DOE/ER-0046/2

Damage Analysis and Fundamental Studies

Quarterly Progress Report
April - June 1980

August 1980

U.S. Department of Energy
Assistant Secretary for Energy Technology
Office of Fusion Energy
Washington, DC 20545

Printed in the United States of America
Available from
National Technical Information Service
U.S. Department of Commerce
5285 Port Royal Road
Springfield, VA 22161

NTJS price codes
Printed copy: A08
Microfiche copy: A01

DOE/ER-0046/2
UC-20,20c

Damage Analysis and Fundamental Studies

Quarterly Progress Report
April -June 1980

August 1980

U.S. Department of Energy
Assistant Secretary for Energy Technology
Office of Fusion Energy
Washington, DC 20545

FOREWORD

This report is the tenth in a series of Quarterly Technical Progress Reports on *"Damage Analysis and Fundamental Studies"* (DAFS) which is one element of the Fusion Reactor Materials Program, conducted in support of the Magnetic Fusion Energy Program of the U. S. Department of Energy. The first eight reports in this series were numbered DOE/ET-0065/1 through 8. Other elements of the Materials Program are:

- Alloy Development for Irradiation Performance (ADIP)
- Plasma-Materials Interaction (PMI)
- Special Purpose Materials (SPM).

The DAFS program element is a national effort composed of contributions from a number of National Laboratories and other government laboratories, universities, and industrial laboratories. It was organized by the Materials and Radiation Effects Branch, Office of Fusion Energy, DOE, and a Task Group on *Damage Analysis and Fundamental Studies* which operates under the auspices of that Branch. The purpose of this series of reports is to provide a working technical record of that effort for the use of the program participants, for the fusion energy program in general, and for the Department of Energy.

This report is organized along topical lines in parallel to a Program Plan of the same title so that activities and accanplishments may be followed readily, relative to that Program Plan. Thus, the work of a given laboratory may appear throughout the report. The Table of Contents is annotated for the convenience of the reader.

This report has been ccmpiled and edited under the guidance of the Chairman of the Task Group on *Damage Analysis and Fundamental Studies*, D. G. Doran, Hanford Engineering Development Laboratory. His efforts and those of the supporting staff of HEDL and the many persons who made technical contributions are gratefully acknowledged. M. M. Cohen, Materials and Radiation Effects Branch, is the Department of Energy counterpart to the Task Group Chairman and has responsibility for the DAFS Program within DOE.

Klaus M. Zwilsky, Chief
Materials and Radiation
Effects Branch
Office of Fusion Energy

CONTENTS

	Page
Foreword	iii
Figures	xi
Tables	xiv
CHAPTER 1. IRRADIATION TEST FACILITIES	1
1. Rotating Target Neutron Source (RTNS)-II Operations (LLNL)	3

A variety of short term irradiations were performed including studies of NbTi, Cu, and Al at 4K.

Facility operation was routine during the quarter.

A dosimetry ezperiment to characterize the neutron field was begun.

2. Fusion Materials Irradiation Test (FMIT) Facility (HEDL)	5

Significant reduction of the saturated level of radioactive ^{7}Be in the FMIT lithium target in order to reduce maintenance problems is difficult to achieve via nuclear means.

The FMIT neutron activation file now has over 1080 reactions on 107 nuclides. The NEUACT code system and the pre-equilibrium code PRECO-D are operational both at HEDL and at NMFECC.

Preliminary analysis was completed of neutron spectra and radiation heating from measurements of the transmission of FMIT-like neutrons through thick iron.

CONTENTS (Cont'd)

Page

Analysis of gamma measurements from the thick target Li (d,xγ) reaction at 35 MeV shows a very small gamma yield of low energy gamma rays.

FMIT-related nuclear data problems are discussed in a workshop report from the recent Symposium on Nuclear Cross Sections from 10 to 50 MeV.

CHAPTER 2. DOSIMETRY AND DAMAGE PARAMETERS 25

1. **Fission Reactor Dosimetry (ANL)** 27

Radiometric and helium accumulation (RIES) dosimeters have been prepared for the HFIR-T1 irradiations. The status of other dosimetry for irradiations in HFIR, ORR, Omega West, and EBR 11 is summarized.

2. **High-Energy Neutron Dosimetry (ANL)** 30

A dosimetry characterization ezperiment has been conducted at RTNS-11 with RIES and LLL. Plans include mapping the neutron field, measuring helium generation rates, testing nuclear cross section, measuring the room return flux, and cross-calibrating active neutron detectors.

3. **Dosimetry Standardization (ANL)** 32

Integral cross-section tests are presented for ENDF/B-V and compared to previous results using ENDF/B-IV. The tests are for Be (d,n) spectra measured at E_d = 14-40 MeV.

CONTENTS (Cont'd)

Page

4. Helium Generation in Fusion Reactor Materials (RIES) 36

Neutron Fluence Map and Total Helium Generation Cross Section for the 14.8-MeV Neutron Irradiation Environment of RTNS-I 37

A detailed neutron fluence map has been constructed for the second Rockwell International irradiation experiment at RTNS-11, and total helium production cross sections have been determined for several pure elements and separated isotopes.

Characterization of the RTNS-II Neutron Field 45

An irradiation experiment has been initiated at RTNS-II to characterize the neutron field, to further develop neutron dosimetry for long-term RTNS-11 experiments, and to measure helium generation cross sections of several separated isotopes and pure elements for 14.8-MeV neutrons.

Helium Production by Be(d,n) Neutrons 45

Initial correlations have been made between the neutron fluence and energy spectrum map and the helium generation results for the Rockwell International-ANL-LLL joint Be (d,n) neutron irradiation experiment at the University of California at Davis.

Helium Accumulation Neutron Dosimetry for Mixed-Spectrum Reactor Irradiations 46

Helium accumulation dosimetry materials were supplied to ANL for inclusion in the Omega West Reactor spectral irradiation and the HFIR irradiations HFIR-MFE-T1 and T2.

CONTENTS (Cont'd)

Page

5. Displacement Functions for Polyatomic Materials (LASL) 49

Displacement production in diatomic materials having a large mass ratio may be quite different in fission and fusion neutron spectra.

6. Damage Parameters for Insulators in FMIT (BNL) 55

An uncollided gamma ray flux estimator has been added to the MORSE Monte Carlo transport code.

The spectrum averaged electronic damage energy cross section has been evaluated for Al_2O_3 and Si_3N_4.

Spectrum average displacement cross sections have been evaluated for $MgAl_2O_4$.

7. Simulation of Short-Term Annealing of Displacement Cascades in FCC Metals (HEDL) 60

Computer modeling experiments using calibrated MARLOWE and SCAS codes indicate that the total number of surviving point defects in an isolated cascade produced at any temperature is proportional to the damage energy for cascade energies from 5 keV up to at Zeast 100 keV.

CHAPTER 3. FUNDAMENTAL MECHANICAL BEHAVIOR 73

1. HVEM Observations of Crack Propagation in Helium Irradiated Type 316 Stainless Steel Containing Precipitates (U. Va.) 76

Chi-phase precipitates on grain boundaries in type 316 stainless steel apparently do not serve as crack initiation

Page

sites when stressed at 900°C or *25°C. They shear crystallographically and neck down under stress at 900°C in the presence of a high density* of *heliwn bubbles at the matrix-precipitate interface.*

CHAPTER 4. CORRELATION METHODOLOGY 91

1. Temperature Dependence of Swelling in Single and Dual-Ion Irradiated 316 Stainless Steel (ANL) 93

In solution annealed and aged MFE 316 stainless steel a broad swelling peak was found for *dual-ion irradiated samples, while a smaller and narrower peak was observed* for *single-ion irradiations of helium preinjected samples.*

2. Dual-Ion Irradiation of Titanium-Modified 316 SS (W-R&D) 103

Microstructural evaluation of *dual-ion bombarded titanium-modified 316 SS at appm He/dpa ratios* of *0.2, 12 and 70 reveals precipitation* of *MC particles in cube-on-cube orientation with the matrix. Small He bubbles are seen in association with the particles in reasonable agreement with observations on the same material after HFIR irradiation.*

A first order attempt at partitioning implanted helium between cavities and dislocations results in reduced critical cavity sizes and lower temperature sensitivity for *the transition from gas-driven to bias-driven cavity growth.*

CONTENTS (Cont'd)

Page

A method is proposed for correcting cavity volume fractions and swelling for statistically combined cavity distributions obtained ut widely different magnifications, foil. thicknesses and cavity sizes.

3. DAFS Specimen Matrix in the AD-2 Irradiation Experiment (HEDL) 121

TEM disks of several ferritic alloys, including two pressure vessel steels and several Fe-Ni-Cr alloys, will be irradiated in EBR-II.

4. HFIR Irradiation of Reoresentative Path B Alloys (HEDL) 126

TEM disks of ADIP Path B alloys B1, B2, B3, and B4 will be irradiated in HFIR.

FIGURES

Page

CHAPTER 1

2. Fusion Materials Irradiation Test (FMIT) Facility (HEDL) 5

FIGURE 1. FMIT neutrons through thick iron. 12

FIGURE 2. Radiation heating rate distribution in direction of incident beam. 13

FIGURE 3. Nickel-58 (n,t) cross section. 14

CHAPTER 2

4. Helium Generation in Fusion Reactor Materials (RIES) 36

FIGURE 1. Contours of constant neutron fluence over the front helium specimen layer for the second RTNS-I irradiation (Units of 10^{17} n/cm^2). 39

FIGURE 2. Neutron fluences obtained from RTNS-I radiometric foils, providing a comparison between dosimetry reaction cross sections. 44

5. Displacement Functions for Polyatomic Materials (LASL) 49

FIGURE 1. Values of the displacement efficiencies k_{ij} as a function of energy for the material MgO (62,00,00,62). 54

FIGURE 2. Values of the displacement efficiencies k_{ij} as a function of energy for the material TaO (60,60,60,60) 54

7. Simulation of Short-Term Annealing of Displacement Cascades in FCC Metals (HEDL) 60

FIGURE 1. The number of frenkel pairs remaining at three stages of simulation annealing as a function of damage energy. 66

FIGURES (Cont'd)

FIGURE 2. Defect production efficiency, expressed as total frenkel pairs per unit damage energy, as a function of damage energy. 67

FIGURE 3. Comparison of defect production functions (smooth curves) of reference 1 with present results. 69

CHAPTER 3

1. HVEM Observations of Crack Propagation in Helium Irradiated Type 316 Stainless Steel Containing Precipitates (U. Va.) 73

FIGURE 1. Micrograph of rod-shaped and irregular precipitates. 88

FIGURE 2. Indices of SAU patterns in figure 1. 89

FIGURE 3. HVEM micrograph of intergranular crack formed at 900°C containing chi phase precipitates. 90

CHAPTER 4

1. Temperature Dependence of Swelling in Single and Dual-Ion Irradiated 316 Stainless Steel (ANL) 93

FIGURE 1. Temperature dependence of swelling in dual-ion and preinjected single-ion irradiated 316 stainless steel. 99

FIGURE 2. Temperature dependence of cavity number density in dual-ion and preinjected single-ion irradiated 316 stainless steel. 100

FIGURE 3. Temperature dependence of mean cavity size in dual-ion and preinjected single-ion irradiated 316 stainless steel. 101

FIGURE 4. Bright-field dark-field pairs showing irregularly shaped cavities in preinjected single-ion and dual-ion irradiated 316 stainless steel. 102

FIGURES (Cont'd)

Page

2. Dual-Ion Irradiation of Titanium-Modified 316 SS (W-R&D) 103

FIGURE 1. BF TEM micrographs showing cavities and precipitates in dually bombarded Ti-modified 316 SS. 115

FIGURE 2. TEM micrographs showing precipitates and dislocation microstructure in dually bombarded Ti-modified 316 SS. 116

FIGURE 3. BF TEM micrographs showing dislocations in dual ion-bombarded Ti-modified 316 SS. 117

FIGURE 4. Fraction of implanted helium atoms partitioned to dislocations as a function of the total dislocation density, for dual-ion bombarded 316 SS in the solution annealed, 20% cold-rolled or aged (800°C) condition. 113

FIGURE 5. Comparison of maximum equilibrium bubble diameter D_C determined from helium inventory method for dual-ion bombarded 316 SS including partitioning of helium to dislocations and excluding partitioning to dislocations. 119

FIGURE 6. Calculated correction factor (F_T) for cavity number density as a function of the ratio of cavity diameter to foil thickness. 120

TABLES

Page

CHAPTER 2

1. Fission Reactor Dosimetry (ANL) 27

TABLE 1. Status of reactor experiments 28

3. Dosimetry Standardization (ANL) 32

TABLE 1. Integral cross section errors deduced from activation and time-of-flight measurements in Be fields. 35

4. *Helium* Generation in Fusion Reactor Materials (RIES) 36

TABLE 1. Total helium generation cross sections for ~ 14.8-MeV neutrons. 42

6. Damage Parameters for Insulators in FMIT (BNL) 55

TABLE 1. Energy deposited through electronic processes. 57

TABLE 2. Spectrum averaged cross sections for $MgAl_2O_4$. 58

CHAPTER 3

1. HVEM Observations of Crack Propagation in Helium Irradiated Type 316 SS Containing Precipitates (U. Va.) 76

TABLE 1. D_{hkl} of precipitate versus D_{hkl} of phases normally found in 316 stainless steel aged at 900°C. 79

TABLE 2. Chemical composition of precipitates and matrix versus nominal type 316 stainless steel. 81

TABLE 3. A comparison of cracks formed in helium irradiated aged type 316 stainless steel with those cracks in unirradiated type 316 stainless steel and neutron irradiated 304 type stainless steel. 84

TABLES (Cont'd)

CHAPTER 4

3. DAFS Specimen Matrix in the AD-2 Irradiation Experiment (HEDL) 121

TABLE 1. OAFS matrix in part 1 of the AD-2 test (390, 500, 550°C) 123

TABLE 2. DAFS matrix in part 2 of the AD-2 test (390, 450, 500°C) 123

4. HFIR Irradiation of Path B Alloys (HEDL) 126

TABLE 1. DAFS specimens for HFIR irradiation. 127

TABLE 2. Irradiations including STA path B alloys. 128

CHAPTER 1

IRRADIATION TEST FACILITIES

I. PROGRAM

Title: RTNS-II Operations (WZJ-16)
Principal Investigator: C. M. Logan
Affiliation: Lawrence Livermore National Laboratory

II OBJECTIVE

The objectives of this work are operation of OFE's RTNS-II (a 14-MeV neutron source facility), machine development, and support of the experimental program that utilizes this facility. Experimenter services include dosimetry, handling, scheduling, coordination, and reporting.

111. RELEVANT OAFS PROGRAM TASK/SUBTASK

TASK II.A.2,3,4.
TASK II.B.3,4.
TASK II.C.1,2,6,11,18.

IV. SUMMARY

A variety of short term irradiations were performed including studies of NbTi, Cu, and Al at 4K.

Facility operation was routine during the quarter.

A dosimetry experiment to characterize the neutron field was begun.

V. ACCOMPLISHMENTS AND STATUS

A. Irradiations - N. E. Ragaini, M. W. Guinan and C. M. Logan(LLNL)

The exposure of glass-bonded mica and MACOR samples for Frank Clinard (LASL) was completed. The exposure of HVEM tensile specimens for Bill Jesser (Univ. of Virginia) was also completed. The irradiation of

NbTi samples at 4°K for R. Van Konynenburg (LLNL) was started and completed. In addition, the irradiation of Cu and Al samples at 4°K for resistivity/damage studies for Mike Guinan (LLNL) was started and completed. Another irradiation of liver enzymes for Vessey (V.A./SFO), Heikkinen, and Logan was done. Quartz and sapphire samples were irradiated for J. McNeese (HEDL). Low fluence irradiations for Russ Jones (PNL) were completed. The neutron field characterization and He production experiment of Kneff et al. (RIES, ANL,LLNL) was begun.

B. RTNS-II Status C. M. Logan and D. W. Heikkinen (LLNL)

There were no major unscheduled outages during this quarter. The on-line computer system for beam and neutron monitoring has been implemented. Target data is now stored on disk and magnetic tape. The terminal horizontal turbo pump has been replaced. This has resulted in improved ion source performance. The unused machine beam transport vacuum system is operational from the accelerator tube section to the target room.

VII. FUTURE WORK

During this quarter irradiations are scheduled for W. Barmore (LLNL), M. Guinan (LLNL), R. Jones (PNL) and N. Panayotou (HEDL). The latter involves installation and check-out of the two temperature furnace.

VIII. PUBLICATIONS

C. M. Logan, J. C. Davis, T. A. Gibson, D. W. Heikkinen, B. J. Schumacher and M. S. Singh "Tritium Experience at RTNS-11", UCRL-83405 (1980)

B. J. Schumacher, "RTNS-II Tritium Scrubber Design and Performance" UCRL-83403 (1980)

I. PROGRAM

Title: Nuclear Data for Damage Studies and FMIT (WH025/EDK)
Principal Investigators: D.L.Johnson/F.M.Mann
Affiliation: Hanford Engineering Development Laboratory (HEDL)

II. OBJECTIVE

The objective of this work is to supply nuclear data needed for damage studies and in the design and operation of the Fusion Material Irradiation Testing (FMIT) facility.

III. RELEVANT DAFS PROGRAM PLAN TASK/SUBTASK

All tasks that are relevant to FMIT use, with emphasis upon:

SUBTASK	II.A.2.3	Flux spectra definition in FMIT
TASK	II.A.4	Gas Generation Rates
SUBTASK	II.A.5.1	Helium Accumulation Monitor Development
SUBTASK	II.B.1.2	Acquisition of Nuclear Data

IV. SUMMARY

Neutron spectra and radiation heating data have been obtained from preliminary analysis of measurements of the transmission of FMIT-like neutrons through thick iron. These data will be used to confirm neutron transport calculations used for predictions of radiation heating in FMIT test cell walls but will also shed light on neutron transport calculations within an experimental test matrix.

Analysis of measurements of the prompt gamma yield and spectra from the thick target Li(d,xγ) reaction at 35 MeV shows a very small gamma yield of low energy gamma rays. Hence this contribution to radiation heating and damage is expected to be much smaller than neutron contributions.

A study of potential methods to reduce the saturated level of radioactive ^{7}Be in the FMIT lithium target and thereby reduce maintenance problems shows that it is difficult to achieve large reductions via nuclear means.

The FMIT neutron activation file now has over 1080 reactions on 107 nuclides. The NEUACT code system and the pre-equilibrium code PRECO-D are operational both at HEDL and at NMFECC.

V. ACCOMPLISHMENTS AND STATUS

A. Neutron Transport and Radiation Heating Measurements --

D.L.Johnson and F.M.Mann (HEDL), G.L.Woodruff (Univ. of Wash.), F.P.Brady, J.L.Romero, J.L.Ullmann, M.L.Johnson and C.M.Castaneda (Univ. of Calif. at Davis)

Measurements of the transmission of FMIT-like neutrons through thick iron and the radiation heating within the iron were briefly outlined in the last DAFS quarterly report. The objective was to provide data to confirm neutron transport calculations which are used for predictions of radiation heating in the FMIT test cell walls. Furthermore, data were obtained for a situation that is nearly identical to that which will be experienced in the test matrices within the FMIT test cell. The comparison of measurements and calculations of the same quantities will shed light primarily on the adequacy of our knowledge of (1) nuclear data for neutrons up to 50 MeV on iron and, (2) characteristics of the bare neutron source. The largest uncertainties might be expected in the nuclear data which have been extended far beyond the 20 MeV limit in ENDF/B evaluations.

The neutrons were produced by a 6mm beam of 35 MeV deutrons stopped in a solid lithium target that was $\sim$ 2.5 cm in diameter by 2 cm thick. This target was placed close to the center of a nearly cubical block of solid iron which was about 60 cm (2 feet) thick on

each side. Neutrons from the source had to penetrate at least about 30 cm (1 foot) of iron in any direction in order to escape the iron block.

Measurements of the neutron spectra were made with detectors placed 10 cm (4 inches) outside the block at 0° and 90° with respect to the beam direction. Proton recoil proportional counters were used to measure the portion of the spectrum from about 10 KeV to about 1.5 MeV where most of the transmitted neutrons are found. An NE213 liquid scintillator was used to measure the spectrum from about 1 MeV up to the maximum that might be observable (about 50 MeV).

Preliminary results of analysis of proton recoil spectral measurements are shown in Figure 1 for the data at 0°. The magnitudes of the data are not yet known, however, the spectral shapes are quite similar to previous observations of neutrons transmitted by thick iron. Note that the spectra drop rapidly above 1 MeV and that there are well known features such as the large peak at about 24 KeV that corresponds to a deep minimum in the iron cross section. The spectrum at 90° has about the same shape as that at 0°.

Preliminary radiation heating data has also been obtained from CaF_2:Mn thermoluminescent dosimeters (TLD's) that were placed within and on the surface of the iron block. Figure 2 shows the distribution of the radiation heating rate (watts/gm-A) through the iron in the direction of the incident beam (0°).

The TLD's are sensitive to radiation heating induced by both gamma rays and by neutrons. The relative contributions have not as yet been determined. The large drop in the heating rate of about 3 orders of magnitude per foot of iron should be a severe test of the calculational model and data. Note that for a beam current of 0.1 amperes, as in FMIT, one projects a heating rate of about 10 watts/gm or more in iron that is adjacent to the target, consistent with earlier transport calculations.

B. Measurements of the Prompt Gamma Yield and Spectra from the Thick Target Li(d,xγ) reaction at 35 MeV. D.L.Johnson and F.M.Mann (HEDL) J.W. Watson, J.L.Ullmann, and W.G. Wyckoff (U.C. Davis)

The gamma yield and spectrum from the FMIT target are needed to evaluate radiation heating and possible gamma induced damage in the vicinity of the FMIT target. Measurements of prompt gamma yield and spectra from 35 MeV deuterons incident on a thick target of natural lithium were done simultaneously with the same NE213 liquid scintillator detector used for measurements of the neutron yields and spectra. This detector can distinguish neutron and gamma ray events via the rise time of their electronic pulses. Preliminary analysis shows the following results. The differential yield as a function of angle is about $2.4(10^9)$(gammas/μc-Sr) and the angular distribution is isotropic. The spectrum has about 80% of the gamma rays with an energy of about 0.5 MeV and about 20% with an energy of about 1 MeV.

When integrated over solid angle the total gamma yield is about $3(10^{10})$ (gammas/μc). This compares with the total neutron yield of about $3(10^{11})$ (neutrons/μc). Hence the ratio of gammas to neutrons is about 1 to 10. This is a very weak gamma production. Even for deuterons of similar energy on beryllium, the ratio is estimated to be nearly unity.

The observed spectrum can be interpreted in terms of only three gamma rays that are expected from deuteron induced reactions in lithium. These gamma rays come from prompt decay of the first excited states of ^{7}Li (.478 MeV), ^{7}Be(0.429 MeV) and ^{8}Li(0.981 MeV) that are populated via these reactions. The angular distributions from decay of these states are known to be essentially isotropic. Note that NO other strong prompt gamma rays were anticipated since all excited states of other product nuclides that may be populated and higher excited states of the nuclides considered above are unbound and decay preferentially via particle emission rather than gamma emission. This contrasts with 33 MeV deuterons on beryllium where reaction products having several bound states

can be formed and the gamma yield is about 6 times larger.

In summary, the small gamma yield compared to beryllium, the energy spectrum, and the isotropic angular distribution all appear to be consistent with expectations. Therefore, the contribution to gamma heating and damage is expected to be quite small compared to the neutron induced contribution even in the immediate vicinity of the target.

C. Reduction of ^{7}Be in the Lithium Target Loop. D.L.Johnson (HEDL)

The radionuclide ^{7}Be is a major consideration in the design of the FMIT lithium system from the standpoint of maintenance. This is because there is a significant production via the reactions $^{7}Li(d,2n)^{7}Be$, and $^{6}Li(d,n)^{7}Be$, the half life is fairly long (53 days), decay gamma rays of about 0.48 MeV are emitted, and it has a tendency to adhere to the walls of piping. It is the only long-lived, gamma-emitting radionuclide that can be produced via deuteron- or neutron-induced reactions with the lithium. Other long-lived, gamma-emitting radionuclides can be produced via deuteron- and neutron-induced reactions with contaminants of other elements in the liquid lithium; however, their contribution to activation levels is much smaller than that of ^{7}Be in proportion to the trace quantities of these contaminants. Therefore, there is substantial interest in searching for potential ways to reduce the quantity of ^{7}Be in the lithium system.

The potential for reduction of ^{7}Be by several means was investigated.

Reduction of the saturated level of ^{7}Be by absorption of thermal neutrons is possible since the energy dependence of the cross section at low energies is l/v and the thermal value is about 50,000 barns. However it would take an external source equivalent to about a 1 megawatt TRIGA reactor in which the coolant and moderator was the FMIT lithium.

Furthermore, the lithium in the loop would have to be enriched to nearly 100% ^{7}Li to reduce parasitic absorption of thermal neutrons by ^{6}Li. Reductions in ^{7}Be of up to about 60% would be possible with such an approach.

Use of ^{6}Li as the target rather than natural lithium would result in a 15% reduction in the saturated ^{7}Be level since the thick target yield from the $^{6}Li(d,n)^{7}Be$ reaction is less than that from natural lithium (92.5% ^{7}Li).

It appears to be difficult to make large reductions in the quantity of ^{7}Be at saturation by nuclear means. It may be necessary to rely on other means such as trapping, or possibly increasing the total lithium volume and thereby decreasing the concentration that can adhere to piping walls.

D. FMIT Neutron Activation Library. F.M.Mann, R.J.Morford, and L.L.Carter (HEDL)

The FMIT Activation Library is a pointwise nuclear cross section library extending from 10^{-5} eV to 40 MeV. Presently over 1080 reactions on 107 nuclides are included. Experimental data, Hauser-Feshbach calculations, the ENDF/B-V evaluated library, and the Lawrence Livermore Laboratory ACTL file were used to update THRESH computer code calculations.

The NEUACT computer code system is designed to combine FMIT flux data with nuclear data to calculate user desired quantities. Three flux libraries are presently available, the empty FMIT test cell, the FMIT test cell filled with half density iron, and the FMIT linac vault. Activation cross sections and decay data for the common materials below zinc are also present. Helium production and displacement cross sections are also present. The code system is in use for calculation of activation of materials in FMIT and has been used to calculate damage rates in the FMIT Test Cell. The code system with abbreviated nuclear

data libraries is also operational at NMFECC.

E. Cross Section Predictions. F.M.Mann (HEDL) and C. Kalbach (Triangle Universities Nuclear Laboratory)

The pre-equilibrium code PRECO-D which predicts the angular distribution of outgoing particles is now operational at HEDL and the NMFECC.

Activation cross sections for the FMIT Activation Library have been calculated for important reactions which are not in the evaluated data libraries of ENDF/B-V and ACTL. Figure 3 shows the results of the HAUSER*5 calculation (multi-step Hauser-Feshbach with pre-equilibrium) along with the experimental data of Qaim[1] and the predictions of THRESH (a code based on systematics).

VI. REFERENCES

1. S. M. Qaim and G. Stocklin, Nuc. Phy., A257 (1976) p. 233; S. M. Qaim and R. Wolfle, Nuc. Phy., A295 (1978) p. 150.

VII. FUTURE WORK

Analysis of measurements of the transmission of FMIT neutrons through thick iron will continue.

Analysis of deuteron activation measurements, described in previous DAFS quarterly reports, will be resumed.

The NEUACT code system will be expanded to include more flux maps and more nuclear data, in particular damage parameters will be installed at NMFECC.

VIII. PUBLICATIONS

None

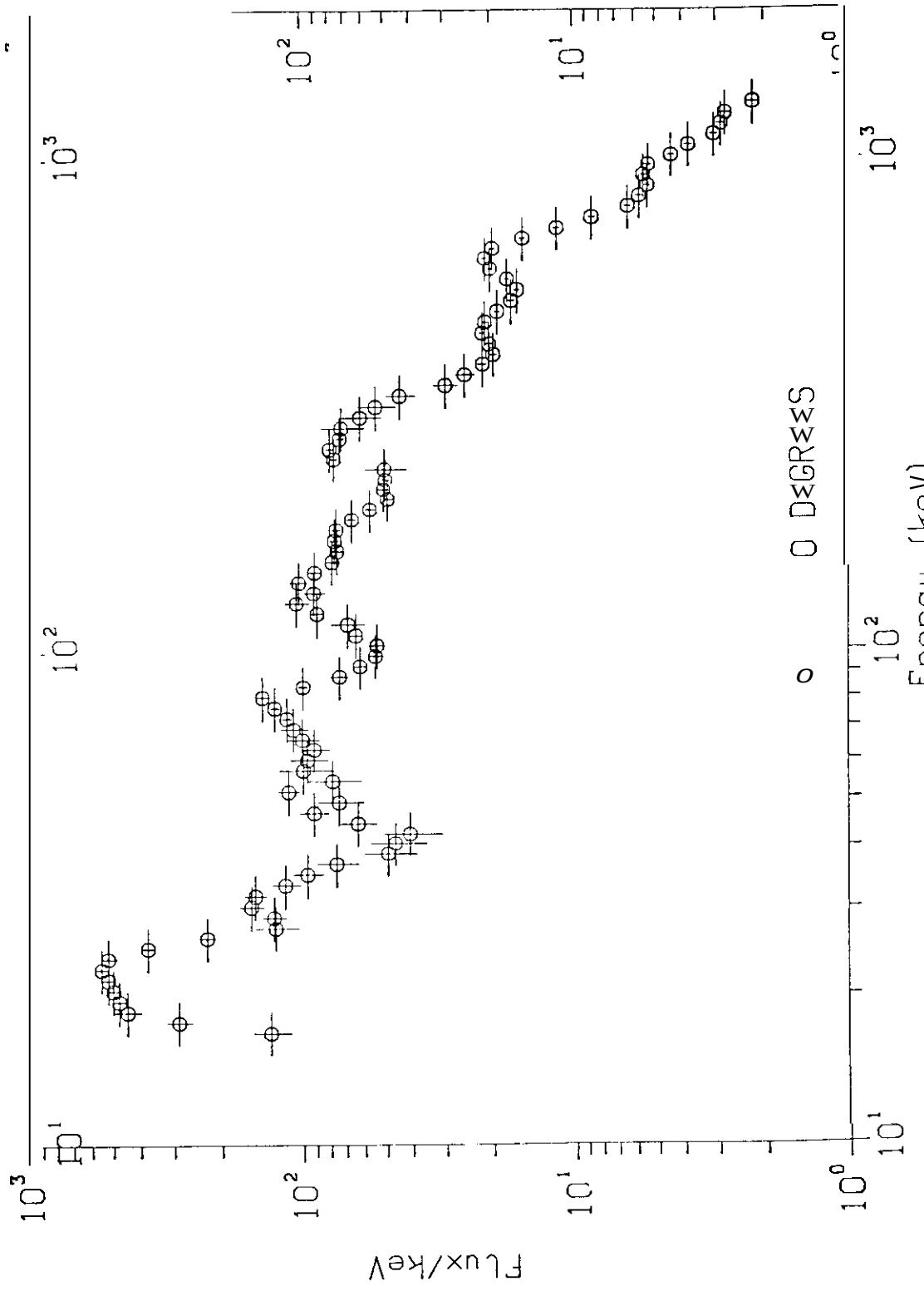

FIGURE 1. FMIT Neutrons Through Thick Iron.

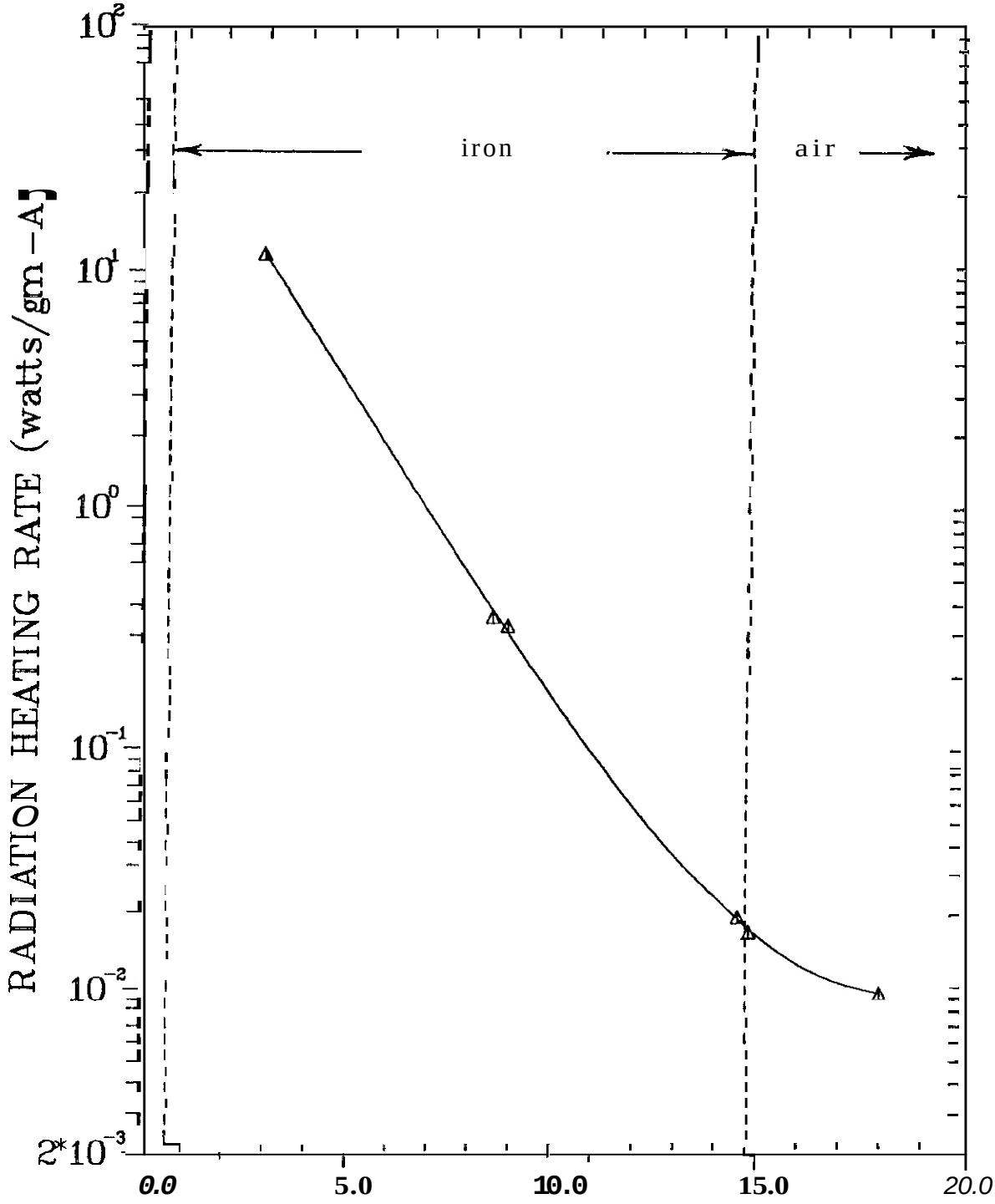
RADIATION HEATING RATE (watts/gm-A)
iron
air
10^{2}
10^{1}
10^{0}
10^{-1}
10^{-2}
$2*10^{-3}$
0.0
5.0
10.0
15.0
20.0

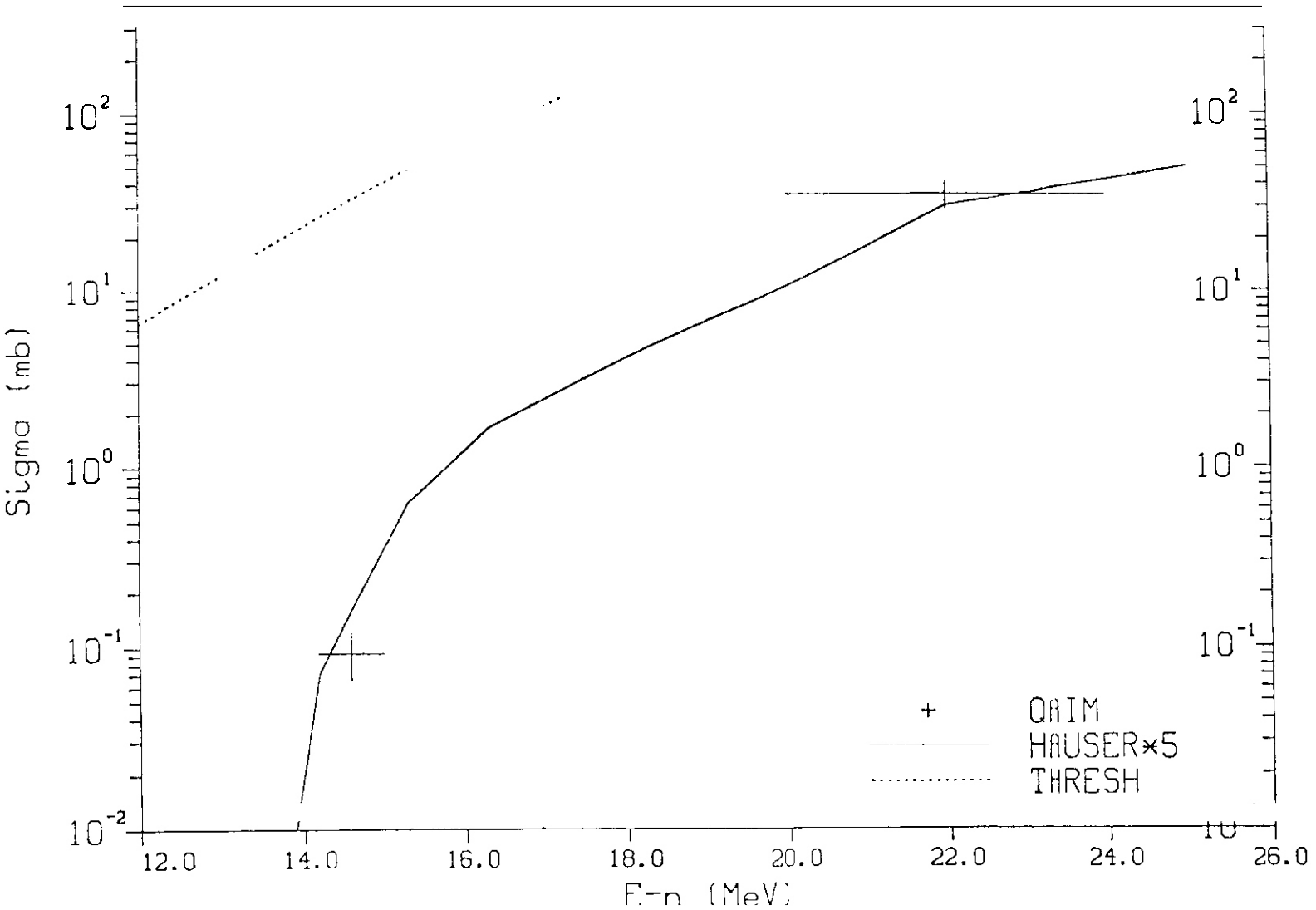

FIGURE 3. Nickel-58 (n,t) Cross Section.

I PROGRAM

Title: Nuclear Data for Damage Studies and FMIT (WH025/EDK)
Principal Investigators: D.L.Johnson/F.M.Mann
Affiliation: Hanford Engineering Development Laboratory (HEDL)

II OBJECTIVE

The objective of this work is to supply nuclear data needed for damage studies and in the design and operation of the Fusion Material Irradiation Testing (FMIT) facility.

III RELEVANT DAFS PROGRAM PLAN TASK/SUBTASK

All tasks that are relevant to FMIT use, with emphasis upon:

SUBTASK	II.A.2.3	Flux spectra definition in FMIT
TASK	II.A.4	Gas Generation Rates
SUBTASK	II.A.5.1	Helium Accumulation Monitor Development
SUBTASK	II.B.1.2	Acquisition of Nuclear Data

IV. SUMMARY

The Symposium on Nuclear Cross Sections from 10 to 50 MeV was held at the Brookhaven National Laboratory from May 12 to 14. The report of the workshop on FMIT related problems is reproduced here by consent of the Symposium chairman.

V. ACCOMPLISHMENTS AND STATUS

The Symposium on Nuclear Cross Sections from 10 to 50 MeV was held at the Brookhaven National Laboratory. The six review papers and the thirty-three contributed papers will be published in a Brookhaven report.

A major part of the symposium were four workshops:

- Intense High Energy Neutron Sources and Their Characteristics
- Differential Data Including Dosimetry Reactions
- Fusion Materials Irradiation Test (FMIT) Facility Related Problems - Shielding and Materials Damage Studies
- Nuclear Model Codes and Data Evaluation.

The reports of these workshops will also appear in the proceedings. The workshop report on FMIT related problems appears on the following pages.

SYMPOSIUM ON NEUTRON CROSS SECTIONS FROM 10-50 MeV

WORKSHOP REPORT

FMIT RELATED PROBLEMS

SHIELDING AND MATERIALS DAMAGE STUDIES

F.M. Mann, HEDL - Chairperson

R.G. Alsmiller, Jr.,	ORNL	D.W. Kneff,	RI
L.L. Carter,	HEDL	R.J. LaBauve,	LASL
D.G. Doran,	HEDL	D.C. Larson,	ORNL
H. Farrar IV,	RI	B. Leonard,	PNL
A.N. Goland	BNL	E.P. Lippincott,	HEDL
R. Gold,	HEDL	B.A. Magurno,	BNL
L.R. Greenwood,	ANL	D.W. Muir	LASL
M.W. Guinan,	LLL	S.M. Qaim	JUL
D. Heikkinen,	LLL	R.E. Schenter	HEDL
D.L. Johnson	HEDL		

I. Introduction

The primary objective of FMIT is to provide a high flux of fusion-energy neutrons for the study of radiation effects in fusion reactor materials. In order to apply materials-property data obtained in FMIT to the prediction of radiation effects in a fusion device, two requirements dependent on nuclear data must be met. One is that the neutron environment to which each specimen is exposed be well defined. To accomplish this, a combination of dosimetry measurements and transport calculations will be needed. A second requirement is that the neutron environment be expressed in terms of energy-dependent damage parameters such as displacement and transmutation rates. Such parameters provide the starting point for damage correlation models needed to relate data

obtained in different environments.

Several other areas impacting both FMIT design and utilization are dependent on adequate nuclear data. These include 1) transport calculations of attenuation in shielding materials and flux-spectra in experimental assemblies, 2) energy deposition in test cell walls and experimental assemblies, 3) activation of facility components and experimental assemblies and specimens.

The FMIT neutron spectra extend to about 50 MeV. In addition, spallation sources such as (LAMPF-WNR, IPNS-I, and SIN) may be used to study radiation effects and their spectra will extend to still higher energies. Hence nuclear data for the above applications are needed well above the 20 MeV limit of the ENDF/B files. In the following section, the status of nuclear data for FMIT applications is briefly described. Recommendations are made for actions that are considered vital for the successful utilization of the FMIT facility.

II. Status and Recommendations

A. Interaction among users and generators of nuclear data

Although there has been informal contact between the users of nuclear data for materials damage studies and for shielding applications and those who generate such data, there must be increased interaction. Generatcrs of nuclear data, whether experimentalists, evaluators, or theorists, must realize that request lists are just indications of user needs. Direct contact must be made so that proper materials, reactions, and energy ranges are investigated.

In order to formalize such interactions the Cross Section Evaluation Working Group (CSEWG) should create a committee designed to ensure that nuclear data needs ior fusion materials studies are recognized and met in a timely and acceptable manner. Coordination with the Damage Analysis and Fundamental Studies Task Group of the DOE-OFE/M&RE branch would be crucial for success. The shielding subcommittee of CSEWG provides an example of such interaction. Such d new committee would help

ensure that user needs are presented to the nuclear data community in a way that the community can understand and respond to. In addition, the committee could oversee the methods, adequacy, and accuracy of files not only in the traditional ENDF/B range of .00001 eV to 20 MeV but also for the higher energy of FMIT (50 MeV for dosimetry cross sections and 40 MeV for damage cross sections). The Special Application Files subcommittee is already responsible for dosimetry, activation, and gas production files to 20 MeV.

The creation of nuclear data is not solely a United States effort. Foreign participation has been significant and is expected to remain so.

B. Dosimetry Reactions

Dosimetry plays an essential role in damage studies as it allows the determination of the neutron exposure of the samples. In order to ensure that an adequate data base is available for FMIT operation, support must be maintained for dosimetry development.

Since the last symposium, much success has been achieved. Passive radiometric foils have been irradiated in d+Be neutron fields produced by 40 MeV deuterons. Measured activities agreed well with calculated activities based on extrapolated cross sections and a time-of-flight measurement of the neutron spectrum (1). In addition, mapping of the d+Be neutron field produced by 30 MeV deuterons using both radiometric foils and helium accumulation neutron dosimetry is being performed (2). Solid state track recorders (SSTR) are being investigated for possible use (3). Also, the ENDF/B-V dosimetry file has been released. Although the file extends to only 20 MeV, it does contain uncertainty data.

However, much work remains to be performed. Table I lists the most important reactions for passive in-situ dosimetry. Note that Arthur, et al (4) have recently provided evaluations of Co-59 and Fe reactions. Additional reactions which may be used for radiometric studies are given in Reference 5 (Table V) and in Reference 6 (Table 6). Because of the limited space in the region of highest flux in FMIT, materials with several useful reactions should have high priority. For the same reason,

consideration should be given to using alloys for dosimetry materials. An important candidate for passive dosimetry is the helium accumulation fluence monitor (HAFM) which requires total helium production cross sections. Because of their possible interference in the interpretation of the active dosimeters, (n,charged particles) cross sections of C, O, and Si will be needed. The measurement of Ra-226 (n,f), (n,2n) and (n,pn) would help extend the usefulness of SSTR's. Further cross section needs may be found in Reference 6.

The supplier of nuclear data must not only supply the needed cross section data, but also the uncertainties in such data. The modern unfolding codes (FERRET, SAND, and STAYSL) use such information to provide the adjustments. In particular, the presence of cross material covariances in the ENDF/B dosimetry file is necessary in certain cases.

C. Damage Cross Sections

Damage cross sections allow material scientists to correlate damage experienced in one type of facility with that in another type. The most important (although not the only) nuclear data needed for the calculation of damage cross sections are the primary recoil spectra and total helium and hydrogen production. The primary recoil spectrum *is* the energy spectrum of the heavy atoms recoiling from elastic scattering and nuclear reactions. Although this spectrum is generated by obtaining the angle-energy emission cross sections of light reactants and then determining the corresponding recoil of the heavy reactant, using reaction kinematics, it should be emphasized that it is the recoil of the heavy atoms that are desired. Thus the creation of primary recoil files (especially if taken directly from adequate model calculations) is highly desirable. Helium production, it must be remembered, includes not only (n,α) reactions but also such reactions as (n,nα) and (n,αn). Similarly, hydrogen production is not simply described by the (n,p) cross section.

A major impediment for damage cross section application for FMIT is the limitation of ENDF/B to a maximum energy of 20 MeV. Greenwood (7)

has extended recoil spectra for several metals up to 44 MeV using approximations to compensate for inadequate data. The LASL evaluation of Fe (4) to 40 MeV and the ORNL evaluation of Cu (8) to 32 MeV are good examples of work needed to lessen the impact of the ENDF/8 limitation.

The acquisition of nuclear data for total helium production by use of helium accumulation (10), charged particle observation (11,12) and activation techniques (13) has been impressive. A recent advance in methodology is the calculation of damage cross sections in multicomponent nonmetals (9,9a).

Although many data have been acquired, the nuclear data base is still meager, particularly in a format useful to the damage studies community. The samples most likely to be irradiated in FMIT will contain Fe, Ni, Cr (highest priority), Ti, Al, Cu (next priority), C, Sn, Nb, and W (lowest priority). Evaluated files containing the recoil spectrum and total helium and hydrogen production are needed for these metals for neutron energies to 40 MeV. In addition, elemental transmutation cross sections are needed but with much lower priority and accuracy. Guidance on specific transmutation products of interest must come from metallurgists. Needless to say, uncertainty estimates and proper documentation are extremely important.

D. Shielding

The need for shielding information is of primary concern during FMIT design. Already data have been obtained for the total cross sections of importance: Fe, O, Si, Ca, and C by ORNL (14), by UCD (15), and by LASL (16). In addition, nonelastic and removal cross sections at 40 and 50 MeV have been determined by UCD for Fe, O, Ca, and C. The new LASL evaluation for Fe which conserves energy will be quite useful in heating calculations.

What is most needed now are evaluations of C, O, and Si. The time scale is short (essentially CY80) and the need is for consistent evaluations. The concept of removal cross sections has been a useful tool and

their measurement is encouraged.

Although activation is not strictly a shielding problem, activation cross sections play an important role not only in bulk shielding design but also in the design of experimental assemblies. The creation of activation files at ANL (17) and at HEDL (18) will be helpful. However, because of their importance, some experimental activation determinations would be helpful. Other needed activation cross sections can be found in Reference 18.

E. Sensitivity Studies

As this area is still in its infancy, sensitivity studies will provide ample rewards. The evaluator of the recoil spectrum should provide strong guidance to the experimenter and model code user as to which cross sections are important in each energy range and for each material. For example, the damage energy response for Fe at 15 MeV arises from inelastic (30%), (n,2n) (~30%), elastic (~20%), and (n. charged particle) (~20%) (19).

Sensitivity studies in calculational dosimetry will provide guidance to evaluators, experimentalists, and model code users as to important reaction types and energy ranges. The use of calculated flux maps will show the response of dosimetry cross sections (6) and damage cross sections (20).

F. Integral Testing

Unlike the situation at fission energies, there does not exist sufficient differential data at higher enerqies for the important materials to provide complete evaluations. Therefore, the use of integral experiments will provide needed checks on the dccuracy of the available experimental data and on the reliability of nuclear model codes. Such checks will not only confirm cross sections but also *the* methods and data used in the calculational dosimetry.

Progress has already been made. Greenwood (1) has shown the con-

sistency of many *of* the passive dosimetry reactions. Qaim, et al (13) have used the d+Be neutron sources to integrally test activation cross sections while Kneff, et al (10) have used similar sources for total helium production. Finally, using time-of-flight measurements, Johnson, et al (21) and Saltmarsh, et al (22) have characterized d+Li and d+Be at deuteron energies of 35 and 40 MeV, respectively.

III. Summary

Much progress has been made in the three years since the last symposium. However, much more progress needs to be made. Increased interaction between the user community and the generators of nuclear data will expedite this progress. Measured and calculated cross section sets must be put into useable form in order to have impact on FMIT utilization.

IV. Refercnces

1. L.R. Greenwood, "Integral Cross Section Testing in a Be-9 (d,n) Field at E(deuterons)=40 MeV," NSE, 72, 175, 1979.
2. D.W. Kneff, et al, paper* II-C3.
3. F.H. Ruddy, et al, paper* IV-C5.
4. E.D. Arthur, et al, paper? V-C4 and C5.
5. L.R. Greenwood, paper* II-R1.
6. R. Gold, et al, paper* IV-C4.
7. L.R. Greenwood, private communication.
8. C.Y. Fu and F.G. Perey, Journal of Nuclear Material 61 (1976) 153.
9. G.F. Dell, et al, paper* IV-C6.

9a. D.M. Parkin and C.A. Coulter, Jour. of Nucl. Mat. 85/86 (1979) 611; ibid, 88 (1980) 249.

10. D.W. Kneff, et al, paper* III-C4.
11. R.C. Haight and S.M. Grimes, paper* III-C1.
12. G. Randers-Pehrson, et al, paper* III-C10.
13. S.M. Qaim, et al, paper* IV-C3.
14. D.C. Larson, papef III-C3.
15. C.I. Zanelli, et al, pape? III-C6.
16. P.W. Lisowski, et al, papef III-C5.
17. L.R. Greenwood, "Extrapolation of Neutron Activation Cross Sections for Dosimetry to 44 MeV," ANL-FPP-TM-115, Nov. 1978.
18. L.L. Carter, et al, papef IV-R1.
19. D.G. Doran, et al, HEDL-TME-76-70, 1976.
20. F.M. Mann, et al, paper* IV-C2.
21. D.L. Johnson, et al, paper* II-C1.
22. M.J. Saltmarsh, et al, Nucl. Instr. and Methods 145 (1977) 81.

* The above mentioned papers are from the symposium.

CHAPTER 2

DOSIMETRY AND DAMAGE PARAMETERS

I. PROGRAM

Title: Dosimetry and Damage Analysis
Principal Investigator: L. R. Greenwood
Affiliation: Argonne National Laboratory

II. OBJECTIVE

To establish the best practicable dosimetry for mixed-spectrum reactors and to provide dosimetry and damage analysis for OFE experiments.

III. RELEVANTS DAFS PROGRAM TASK/SUBTASK

SUBTASK II.A.1.1 Flux-spectral definition in a tailored fission reactor.

SUBTASK II.A.1.3 Applications.

IV. SUMMARY

Dosimeters have been prepared for the T1 and T2 irradiations in HFIR.

The status of all other reactor irradiations is summarized.

V. ACCOMPLISHMENTS AND STATUS

A. Flux-Spectral Measurements in HFIR - L. R. Greenwood (ANL)

Dosimetry capsules have been prepared for the T1 and T2 irradiations in the High Flux Isotopes Reactor (HFIR) at ORNL. Six aluminum capsules were fabricated, each measuring 1/8" OD by 1/2" in length. Twelve dosimetry wires were encapsulated, each measuring 20-40 miles OD by 1/16" - 1/8" length. Radiometric dosimeters included, Ni, Cu, 0.1% Co-Al, 80%

Mn-Cu, Nb, Ti, Fe, and Zr. Helium analysis will be performed on these specimens by Rockwell International as well as for additional samples of Al and alloys of B and Li.

B. Status of Other Experiments

The status of all other reactor dosimetry measurements is summarized in the following table.

TABLE 1
Status of Reactor Experiments

Fatility/ Experiment	Status and Comments
ORR	
-MFE 1	Analysis complete
-MFE 2	Irradiation completed, samples en route to ANL for analysis
-MFE 4A	Irradiation started 5/80
-MFE 4B	Dosimeters sent to ORNL 5/80
-TBC 07	Analysis in progress
HFIR	
CTR 30,31,32	Dosimeters sent to ORNL 4/80
T1, T2	Dosimeters sent to ORNL 6/80
Omega West	
Spectral Run	Dosimeters sent to LASL 5/80
EBR II	
X287	Analysis in progress

VI. REFERENCES

None

VII. FUTURE WORK

The MFE 4A and 4B irradiations in ORR and the HFIR irradiations have several parts which will be irradiated from 3 months to several years. Dosimeters will be analyzed for each segment of the irradiation and compared to neutronics calculations. Helium measurements and calculations will also be obtained for all irradiations.

VIII. PUBLICATIONS

A paper entitled "Review of Source Characterization for Fusion Materials Irradiations" was presented at the Symposium on Neutron Cross Sections from 10-50 MeV at BNL on May 12-14, 1980.

I. PROGRAM

Title: Dosimetry and Damage Analysis
Principal Investigator: L. R. Greenwood
Affiliation: Argonne National Laboratory

11. OBJECTIVE

To establish the best practicable dosimetry for high-energy neutron facilities.

III. RELEVAIITS OAFS PROGRAM TASK/SUBTASK

SUBTASK **II.A.2.2** Flux-spectral definition in RTNS-II.

IV. SUMMARY

A dosimetry experiment has been irradiated at RTNS-II, jointly with RIES and LLL. Radiometric and helium generation data will be used to characterize the facility.

V. ACCOMPLISHYENTS AND STATUS

Flux-Spectral Characterization of RTNS-II - L. R. Greenwood (ANL), O. Kneff (RIES), M. Guinan (LLNL)

A joint irradiation was conducted during June *23* - July *3*, 1980 at the Rotating Target Neutron Source (RTNS)II at Lawrence Livermore Laboratory (LLL). Approximately 400 radiometric foils and *200* helium specimens were irradiated at locations close to the source as well as on 5, 15, and *30* cm arcs. Large foil specimens were also placed at the rear of the target cart and on the back wall to measure room return effects. Other foils were placed near the active neutron detectors (proton recoil and ionization chamber) to provide a cross calibration.

Following irradiation, all of the samples will be analyzed at ANL, LLL, and Rockwell International Energy Systems (RIES). The neutron fiels will be mapped, similar to previous work at RTNS-I[1] and U. C. Davis.[2]

VI. REFERENCES

1. H. Farrar IV, D. W. Kneff, R. A. Britten, and R. R. Heinrich, Symposium on Neutron Cross Sections 10-40 MeV, BNL-NCS-50681, p. 175 (1977).

2. L. R. Greenwood, DOE/ER-0045/1, Damage Analysis and Fundamental Studies Quarterly Progress Report, p. 30 (1980); see also section VIII.

VII. FUTURE WORK

Following the irradiation, the Au, Co, Ag, Ti, Mn, Cu, and Zr foils will be gamma counted at ANL; the Nb, Ni, Fe, Al, Sc, Y, and Tm foils at LLL; and the helium specimens will be analyzed at RIES. In addition, selected helium specimens will also be gamma counted. We then expect to map the neutron field, measure helium generation rates, test radiometric and helium generation cross sections, measure thermal or room return neutrons, and cross calibrate active neutron systems.

VIII. PUBLICATIONS

1. O. W. Kneff, H. Farrar IV, L. Greenwood, and M. W. Guinan, Characterization of the Be (d,n) Neutron Fields by Passive Dosimetry Techniques, Proceedings of Symposium on Neutron Cross Sections 10-50 MeV, BNL, May 1980.

I. PROGRAM

Title: Dosimetry and Damage Analysis
Principal Investigator: L. R. Greenwood
Affiliation: Argonne National Laboratory

11. OBJECTIVE

To enhance flux-spectral unfolding techniques for OFE materials irradiations.

III. RELEVANTS DAFS PROGRAM TASK/SUBTASK

TASK II.A.6 Dosimetery Standardization.

TASK II.A.l Fission Reactor Dosimetry.

TASK II.A.2 High-Energy Neutron Dosimetry.

IV. SUMMARY

All neutron activation files have been revised according to ENDF/B-V. All integral data testing has been repeated and the results are compared to previous tests using ENDF/B-IV.

V. ACCOMPLISHMENTS AND STATUS

A. Integral Tests of ENDF/B-V Neutron Activation Cross Sections

L. R. Greenwood (ANL)

As reported last quarter (DOE/ER-0046/1), all dosimetry cross-section files have been revised according to ENDF/B-V.[1] Since we have previously conducted integral tests of many of the cross sections in Be (d,n) neutron fields,[2,3] we have now repeated these tests using the revised data.

Table I presents a comparison of average integral cross section errors obtained with ENDF/B-IV and V. Be(d,n) neutron fields were measured by time-of-flight spectrometry at deuteron energies of 14, 16, and 40 MeV. As can be seen in Table I, version V generally does better than version IV, although both versions are quite accurate (<10%) for most of the cross sections. At the lower energies, the largest improvements are seen for ^{60}Ni(n,p) and ^{58}Ni(n,2n), especially in the threshold region. Significant errors are still seen with ^{45}Sc(n,2n) and ^{90}Zr(n,2n). At higher energies the differences are much smaller since ENDF stops at 20 MeV.

Although we have not conducted integral tests for fission spectra, we have also tried the new data using dosimetry measurements at the Oak Ridge Research Reactor. Again, the differences between versions IV and V are generally small (<5%), although significant discrepancies persist in both versions for the ^{60}Ni(n,p), ^{54}Fe(n,α), and ^{47}Ti(n,p) reactions. The ^{238}U(n,f), ^{58}Ni(n,p), and ^{48}Ti(n,p) cross sections appear to be more consistent in version V.

A more complete description of these results was presented at a recent conference at Brookhaven National Laboratory.[4]

VI. REFERENCES

1. ENDF/B-V Dosimetry File, National Neutron Cross Section Center, Brookhaven National Laboratory, 1979.

2. L. R. Greenwood, R. R. Heinrich, R. J. Kennerley, and R. Medrzychowski, Nucl. Technol. 41, 109 (1978).

3. L. R. Greenwood, R. R. Heinrich, M. J. Saltmarsh, and C. B. Fulmer, Nucl. Sci. Eng. 72, 115 (1979).

4. L. R. Greenwood, Review of Source Characterization for Fusion Materials Irradiations, Proceedings of Symposium on Neutron Cross Sections from 10-50 MeV, BNL, May 12-14, 1980.

VII. FUTURE WORK

Further integral data testing is now being planned at the University of California at Davis cyclotron. The ENDF/B-V cross-section error and covariance data files are also being compared to our integral results.

VIII. PUBLICATIONS

These results were presented at a recent cross-section conference at BNL.[4].

TABLE 1

Integral Cross Section Errors (ENDF/B) Deduced from Activation and Time-of-Flight Measurements in Be (d,n) Fields. Absolute errors are ±10%; relative ±2%

Keaction	E_D = 14-16 MeV IV	E_D = 14-16 MeV V	E_D = 40 MeV IV	E_D = 40 MeV V
$^{235}U(n,f)$	+7	+8	+1	+1
$^{238}U(n,f)$	+4	+4	-1	-1
$^{115}In(n,n')^{115m}In$	-1	-2	-3	-2
$Ti(n,p)^{46}Sc$	-7	-1	-89(+14)[a]	(+24)[a]
$Ti(n,p)^{47}Sc$	t2	+6	-798(+15)[a]	(-56)[a]
$^{48}Ti(n,p)48Sc$	-7	-1	+2	t4
$Fe(n,p)^{54}Mn$	+6	-3	-89(+1)[a]	(+4)[a]
$^{56}Fe(n,p)56Mn$	-2	-2	-4	-4
$^{59}Co(n,p)59Fe$	-8	-4	+8	+5
$^{58}Ni(n,p)58Co$	0	-3	+9	+3
$^{60}Ni(n,p)60Co$	+14	-2	+3	+3
$^{27}Al(n,\alpha)24Na$	t3	+6	0	-1
$^{54}Fe(n,\alpha)^{51}Cr$	-4	+1	-36	-20
$^{59}Co(n,\alpha)^{56}Mn$	-4	-2	-4	-5
$^{45}Sc(n,2n)^{44m}Sc$	-14	-15	-1	+3
$^{58}Ni(n,2n)57Ni$	-11	+1	-30(+14)[b]	(+14)[b]
$^{59}Co(n,2n)58Co$	+1	+6	-9	-3
$Zr(n,2n)^{89}Zr$	+13	+9	-4	-1
$^{93}Nb(n,2n)^{92m}Nb$	t7	+6	+6	+7
$^{169}Tm(n,2n)^{168}Tm$	--	--	+7	+10
$^{169}Tm(n,3n)^{167}Tm$	--	--	-9	-8
$^{197}Au(n,2n)^{196}Au$	-9	-8	-1	+1
$^{197}Au(n,3n)^{195}Au$	--	--	+8	+12
$^{197}Au(n,4n)^{194}Au$	--	--	+1	+1
$^{238}U(n,2n)^{237}U$	+4	+1	-11	-11

[a] Values in parenthesis include contributions from higher mass isotopes.

[b] Value in parenthesis modified according to B. P. Bayhurst, et al., Phys. Rev. C12,451 (1975).

I. PROGRAM

Title: Helium Generation in Fusion Reactor Materials
Principal Investigators: D. W. Kneff, Harry Farrar IV
Affiliation: Rockwell International, Energy Systems Group

II. OBJECTIVE

The objectives of this program are to measure helium generation rates of materials for Magnetic Fusion Reactor applications in the various neutron environments used for fusion reactor materials testing, to characterize these neutron test environments, and to develop helium accumulation neutron dosimeters for neutron fluence and energy spectrum dosimetry in these test environments.

III. RELEVANT DAFS PROGRAM PLAN TASK/SUBTASK

SUBTASK II.A.4.2	T(d,n) Helium Gas Production Data
SUBTASK II.A.4.3	Be(d,n) Helium Gas Production Data
TASK II.A.1	Fission Reactor Dosimetry
SUBTASK II.A.2.1	Flux-Spectral Definition in the Be(d,n) Field
SUBTASK II.A.2.2	Flux-Spectral Definition in RTNS-II
SUBTASK II.A.5.1	Helium Accumulation Monitor Development

IV. SUMMARY

The neutron fluence map has been completed for the second joint Rockwell International-Argonne National Laboratory (ANL)-Lawrence Livermore Laboratory (LLL) 14.8-MeV neutron irradiation experiment at RTNS-I, and total helium production cross sections have been determined for several pure elements and separated isotopes. Initial correlations have been made between the radiometric neutron spectrum map and helium generation results for the Rockwell-ANL-LLL joint Be(d,n) neutron irradiation

experiment. Another interlaboratory irradiation experiment has been initiated to characterize the neutron environment and measure helium generation cross sections in RTNS-II. Helium accumulation dosimetry materials were supplied to ANL for inclusion in the Omega West Reactor spectral irradiation, and in the High Flux Isotopes Reactor (HFIR) irradiation experiments HFIR-MFE-T1 and T2.

V. ACCOMPLISHMENTS AND STATUS

A. Neutron Fluence Map and Total Helium Generation Cross Sections for the 14.8-MeV Neutron Environment of RTNS-I -- D. W. Kneff, B. M. Oliver, M. M. Nakata, and Harry Farrar IV (Rockwell International, Energy Systems Group)

A detailed neutron fluence map has been constructed for the high-flux region of the Rotating Target Neutron Source-I (RTNS-I) neutron field, for the second joint Rockwell International-ANL-LLL neutron irradiation experiment. This map, based on a combination of foil activation and helium accumulation dosimetry, was then combined with the mass spectrometric helium analyses of several pure elements and separated isotopes to determine total helium generation cross sections for these materials. The analysis of this experiment was also supported in part by the Department of Energy's Office *of* Basic Energy Sciences.

The irradiation experiment has been described in detail elsewhere.[1,2] The irradiation assembly consisted basically of a small stainless steel capsule containing two layers of pure elements, separated isotopes, and pure element helium accumulation dosimetry wire rings, sandwiched between layers of thin radiometric dosimetry foils. The foils were provided by ANL. The assembly was mounted on the fixed outside cover of the RTNS-I rotating tritium target assembly, and irradiated to a total neutron fluence ranging from 0.3 to 2.6 x 10^{17} n/cm^2 over the

volume of the capsule. The average neutron energy was determined to be 14.8 ± 0.1 MeV. Following the irradiation, the radiometric foils were segmented for subsequent counting at ANL and LLL. The helium generation samples were etched, segmented, weighed, and analyzed for helium using high-sensitivity gas mass spectrometry.(3)

A detailed three-dimensional neutron fluence map was then constructed for the capsule irradiation volume using the data from the radiometric and helium accumulation dosimetry materials included in the capsule.(2) This mapping was particularly important because of the steep fluence gradients present within the capsule volume, and because the fluence determination is the largest source of uncertainty in the cross section measurements. An average map was first constructed using the foil activation counting results, assuming a symmetric neutron fluence profile. Figure 1a shows the fluence contours derived from this map for the midplane of the first (upstream) specimen layer of the irradiation capsule.

Detailed adjustments were then made to this map using the helium concentration gradients measured about the Al, Ti, Fe, Ni, and Cu helium accumulation dosimetry rings included in the irradiation capsule. Variations in the normalized helium concentration results with position in the capsule for each element provided a very sensitive measure of the irregularities in the neutron fluence profile. The sensitivity of these latter measurements follows from the fact that the helium generated in each segment was measured with an absolute 1σ uncertainty of 1-2%. Additionally, because the rings were approximately concentric about the neutron source axis, and the average neutron energy was nearly constant over the sample irradiation volume, the helium generation cross sections were also effectively constant over this volume. The neutron fluence map derived by combining this helium accumulation dosimetry with the radiometric map is represented by the following empirical expression:

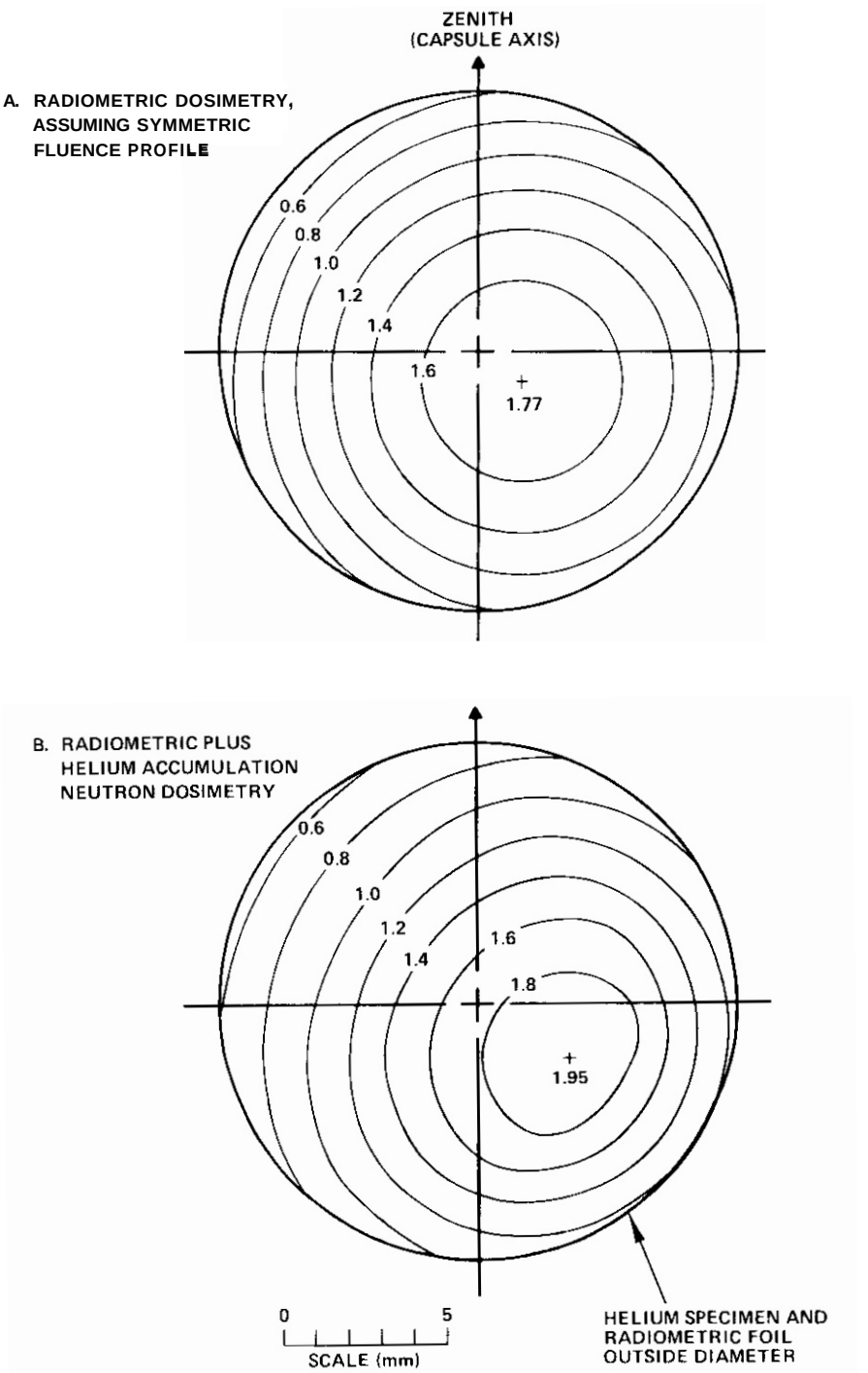

FIGURE 1. Contours of Constant Neutron Fluence Over the Front Helium Specimen Layer for the Second **RTNS-I** Irradiation (Units of 10^{17} n/cm^2).

$$\Phi(R,\theta_c,\Delta Z)=\alpha\left[C_0+C_2(\beta R)^2+C_3(\beta R)^3\right]\left[1+K\left(\frac{R_c-4.5}{15}\right)\sin(\theta_c-60)\right], \qquad (1)$$

where R is the radial distance from the neutron source axis, AZ is the axial distance from the front face of the capsule, θ_c is the polar angle about the irradiation assembly axis, and R_c is the radial distance from this axis. The term $\alpha = \left[C_4/(C_4+\Delta Z)\right]^2$ is the normalization of the radial profile as a function of AZ, and $\beta = C_5/(C_5+\Delta Z)$ is an adjustment factor for the changing radial shape of the fluence curve as a function of AZ. The C_i are constants, and K = 1 ($R_c > 4.5$) or 0 ($R_c \leq 4.5$).

Figure 1b is the fluence contour plot for the midplane of the upstream specimen layer of the irradiation capsule, as represented by Equation (1). The irregular profile shape suggests that one edge of the time-averaged deuteron beam was attenuated by a beam-line collimator. Comparison of Figure 1b with Figure la shows that this irregular deuteron beam profile produced fluences significantly different from those calculated by initially assuming a symmetric fluence profile. This final map was also found to be more consistent with the less-detailed radiometric dosimetry results. The map results, and in particular the factor-of-four variation in fluence over the 2-cm^2 area represented by Figure 1, demonstrate the importance of including comprehensive passive dosimetry in neutron irradiation experiments.

The 1σ absolute fluence uncertainty for this final neutron fluence map is estimated to be 7%. This includes an estimated 57 relative uncertainty from the map itself, due in part to additional but smaller irregularities not incorporated in the map, and 2" and 4' absolute uncertainties from the radiometric counting results and from the $^{93}Nb(n,2n)$ cross section, respectively. A $^{93}Nb(n,2n)^{92m}Nb$ cross section value of 463 ± 19 mb[4] was adopted as the absolute normalization for this fluence map.

The ^{4}He generated in the irradiated samples measured to date from this experiment ranged from 3 x 10^{11} atoms (from ~0.5-mg samples) to 1.2 x 10^9 atoms (from ~5-mg samples). This corresponds to ^{4}He concentrations ranging from 25.7 appb (atomic parts per billion, 10^{-9} atom fraction) in aluminum, down to 0.072 appb in gold. Absolute 1σ uncertainties for most of the ^{4}He measurements were $\leq$2%. The particularly low helium concentrations in the gold samples were measured to average 1σ uncertainties of ~3-10%. Measurements of ^{3}He were also made for several samples, including all of the separated isotopes, but none was detected in each case. The upper limit of the ^{3}He concentration for the nickel and copper isotopes was 0.05 appb.

The total helium production cross sections determined for these materials are presented in Table 1. These results were obtained by combining the measured helium concentrations with the neutron fluences obtained from the map. The cross sections for the specific isotopes were evaluated by first determining the cross sections for the available isotope enrichments, and then solving a matrix of equations for each isotopic material to correct for the small concentrations of each of the other isotopes in the material. The cross section values obtained for different specimens of each material at different locations within the irradiation capsule were generally in very close agreement (within ±4%) This reflects the reproducibility of the helium measurements (to within 2%), and also demonstrates the validity of the final fluence map.

Table 1 also shows that the present cross section determinations for Al, Ti, Fe, and Cu are in excellent agreement with the results for the same materials in a previous RTNS-I irradiation.[5] The exception is gold, for which the high helium concentrations measured previously are attributed almost entirely to α recoils into the thin foils from nearby materials. Also shown in Table 1 are the corresponding charged-particle measurements of Grimes, et al.[6,7] Comparison of these measurements

TABLE 1

TOTAL HELIUM GENERATION CROSS SECTIONS FOR ~14.8-MeV NEUTRONS

Material	Cross Section (mb)		
	Present Work	Previous Experiment[a]	Charged-Particle Measurements[b]
Al	145 ± 10	143 ± 7	121 ± 25
Ti	37 ± 3	38 ± 3	34 ± 7
Cr	34 ± 4	-	38 ± 6
Fe	48 ± 3	48 ± 3	43 ± 7
Ni	100 ± 7	98 ± 6	97 ± 16
^{58}Ni	116 ± 8	-	106 ± 17
^{60}Ni	79 ± 6	-	76 ± 12
^{61}Ni	53 ± 4	-	-
^{62}Ni	18 ± 6	-	-
^{64}Ni	61 ± 4	-	-
cu	51 ± 3	51 ± 3	42 ± 7
^{63}Cu	67 ± 5	-	56 ± 10
^{65}Cu	17 ± 2	-	13 ± 3
Au	0.72 ± 0.09	24 ± 12[c]	-

[a] Farrar and Kneff, Ref. 5.

[b] Grimes, et al., Ref. 6, 7.

[c] High value attributed to helium recoil into the thin Au samples available for analysis.

with the helium generation results shows that the cross section measurements of Grimes, ~~et al.~~ are generally lower, but agree within the quoted uncertainties.

A comparison between the helium production cross sections for the individual isotopes and their associated pure elements provides a good consistency check of the measurements. The sums of the isotopic cross sections for nickel and copper, respectively, weighted by the natural isotopic abundances, are 102 ± 7 mb and 52 ± 4 mb. These values are in excellent agreement with the 100 ± 7 mb and 51 ± 3 mb cross sections measured for the natural pure elements, respectively.

It is also of interest to compare the previously measured helium production cross section of Type 316 stainless steel, a primary candidate structural material for first generation fusion reactors, with the weighted sum of the cross sections of the component elements. The measured stainless steel cross section is 57 ± 4 mb.[5] The weighted sum of the constituent elements Fe, Cr, Ni, Mo, and C [Mo and C from a previous experiment[5]] is 52 ± 3 mb. The small difference is greater than expected from the various uncertainties, and may be due in part to a minor stainless steel component with a relatively high helium production cross section.

This experiment also provided information on the relative cross sections of the radiometric dosimetry reactions used. Figure 2 shows the calculated neutron source axis fluences for most of the segmented radiometric foils, plotted as a function of the foil distance from the front face of the irradiation capsule. The solid curve is the axial fluence profile, as defined by Equation (1). Examination of the data shows that a number of inconsistencies exist between these reaction cross sections. The assumed cross section for the $^{197}Au(n,2n)^{196}Au$ reaction (2110 mb) is in excellent agreement with the $^{93}Nb(n,2n)^{92m}Nb$ cross section (463 mb),

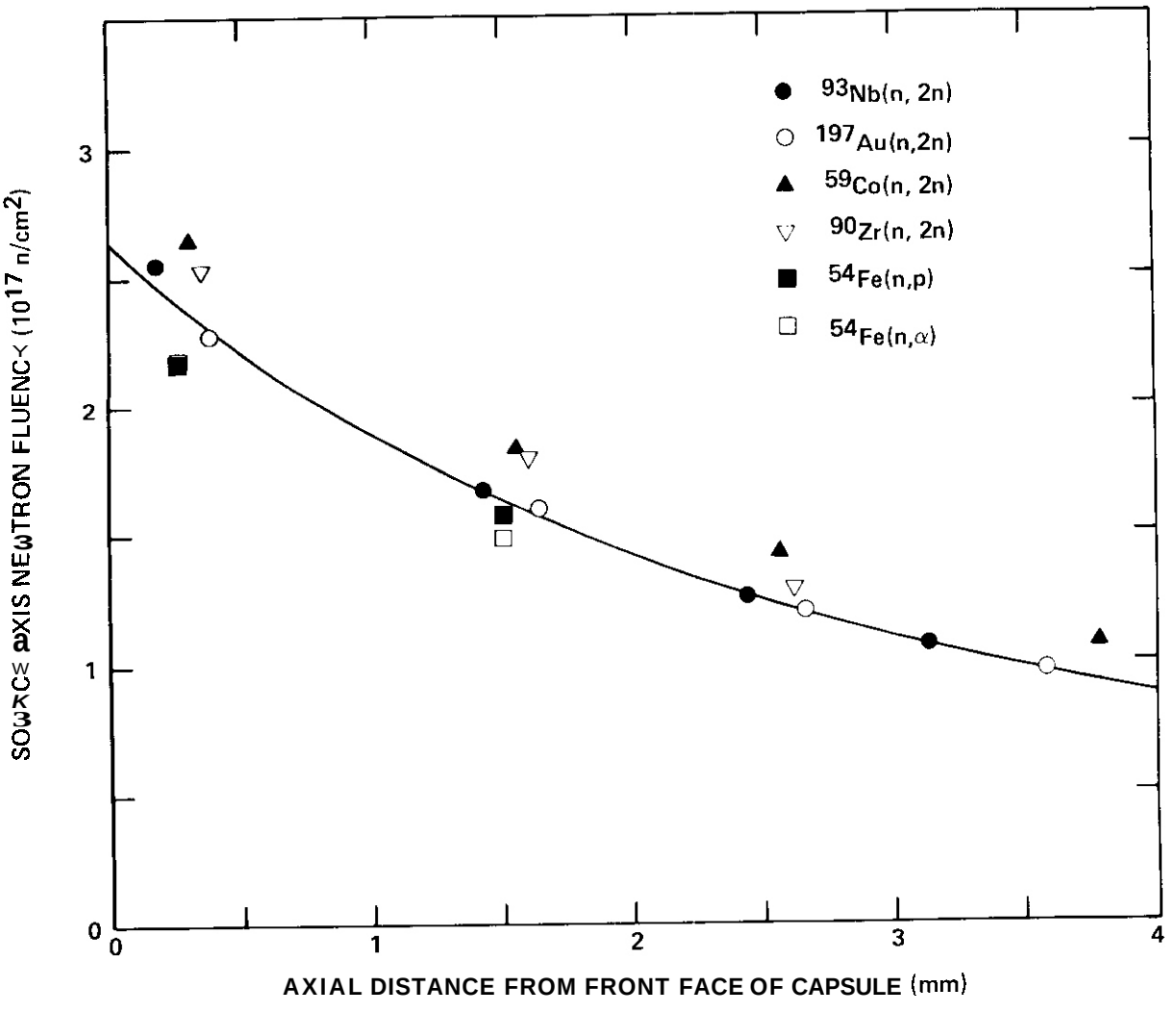

FIGURE 2. Neutron Fluences Obtained from RTNS-I Radiometric Foils, Providing a Comparison Between Dosimetry Reaction Cross Sections.

as demonstrated previously.[8] However, the assumed $^{59}Co(n,2n)^{58}Co$ cross section (692 mb) is about 12% low relative to $^{93}Nb(n,2n)$, and that for $^{90}Zr(n,2n)^{89}Zr$ (760 mb) is about 5% low. The assumed cross sections for $^{54}Fe(n,\alpha)^{51}Cr$ (95 mb) and $^{54}Fe(n,p)^{54}Mn$ (306 mb) both appear to be high relative to niobium. More detailed cross section comparisons require further analysis.

B. Characterization of the RTNS-II Neutron Field -- D. W. Kneff, B. M. Oliver, M. M. Nakata, and Harry Farrar IV (Rockwell International, Energy Systems Group)

A neutron characterization experiment has been initiated at the RTNS-II facility at LLL. The objectives of this experiment, a joint experiment with L. R. Greenwood (ANL) and M. W. Guinan (LLL), are to characterize the RTNS-II neutron environment for small-target experiments, further develop neutron dosimetry for long-term experiments at this facility, and measure helium generation cross sections for 29 pure elements, 45 separated isotopes, and 3 candidate fusion reactor alloys. The irradiation assembly consists of a small stainless steel capsule containing numerous helium accumulation samples, wire dosimetry rings, and activation foils, and a relatively large trailing assembly containing additional activation and helium accumulation materials at well-defined source angles. The irradiation will be completed during the first week of the next report period, and will be described in detail in the following quarterly progress report.

C. Helium Production by Be(d,n) Neutrons -- D. W. Kneff, Harry Farrar IV (Rockwell International, Energy Systems Group), L. R. Greenwood (ANL), and M. W. Guinan (LLL)

Initial correlations have been made between the neutron fluence and energy spectrum map and the helium generation results for the joint

Rockwell International-ANL-LLL Be(d,n) neutron irradiation experiment. The objectives of this experiment,[**]) performed with 30-MeV deuterons, were to characterize the neutron field in detail, further develop radiometric and helium accumulation neutron dosimetry, and measure the helium generation cross sections of several materials in this neutron environment. The neutron spectrum map, derived from the spectral unfolding of the radiometric dosimetry data, using an irradiation assembly beam axis offset determined from helium accumulation dosimetry, was described briefly in the previous quarterly progress report.[9] Initial comparisons have now been made between the spectrum-integrated helium generation data and total helium production cross section evaluations taken from the literature.[10] The literature values were combined with the neutron spectral map to predict helium generation profiles within the irradiation volume. Comparisons with the data demonstrate the potential to integrally test helium generation cross sections for this neutron environment. This work will be continued by making more detailed comparisons with updated cross section evaluations, and will be reported in a subsequent quarterly progress report.

D. Helium Accumulation Neutron Dosimetry for Mixed-Spectrum Reactor Irradiations -- D. W. Kneff and Harry Farrar IV (Rockwell International, Energy Systems Group)

Helium accumulation dosimetry materials were supplied to ANL for inclusion in the Omega West Reactor spectral irradiation, and in the High Flux Isotopes Reactor (HFIR) irradiation experiments HFIR-MFE-T1 and T2.

VI. REFERENCES

1. D. W. Kneff and H. Farrar IV, Helium Generation in Fusion Reactor Materials, Technical Progress Report for Period April - September 1977, AI-DOE-13219, Atomics International, Canoga Park, California, January 1978.

2. D. W. Kneff, B. M. Oliver, M. M. Nakata, and H. Farrar IV, "Helium Generation Cross Sections for Fast Neutrons," Symposium on Neutron Cross Sections from 10 to 50 MeV, Brookhaven National Laboratory, NY, May 1980 (to be published).

3. H. Farrar IV, W. N. McElroy, and E. P. Lippincott, "Helium Production Cross Section of Boron for Fast-Reactor Neutron Spectra," Nucl. Technol. 25, 305 (1975).

4. D. R. Nethaway, "The $^{93}Nb(n,2n)^{92m}Nb$ Cross Section," J. Inorg. Nucl. Chem. 40, 1285 (1978).

5. H. Farrar IV and D. W. Kneff, "Helium Generation in Twelve Pure Elements by 14.8-MeV Neutrons," Trans. Am. Nucl. Soc. 28, 197 (1978).

6. S. M. Grimes, R. C. Haight, K. R. Alvar, H. H. Barschall, and R. R. Borchers, "Charged-Particle Emissions in Reactions of 15-MeV Neutrons with Isotopes of Chromium, Iron, Nickel, and Copper," Phys. Rev. C 19, 2127 (1979).

7. R. C. Haight and S. M. Grimes, "Experimental Studies of (n, charged particle) Cross Sections, Angular Distributions and Spectra with a Magnetic Quadrupole Spectrometer," UCRL-80235, Lawrence Livermore Laboratory (1977).

8. H. Farrar IV, D. W. Kneff, R. A. Britten, and R. R. Heinrich, "Fluence Mapping of RTNS-I by Helium Accumulation and Foil Activation Methods," Proc. Symp. on Neutron Cross-Sections from 10 to 40 MeV, M. R. Bhat and S. Pearlstein, eds., BNL-NCS-50681, pp. 175-184, Brookhaven National Laboratory, NY, July 1977.

9. L. Greenwood, M. Guinan, and D. Kneff, "Characterization of the Be(d,n) Source at U.C. Davis, E_d = 30 MeV," in Damage Analysis and Fundamental Studies, Quarterly Progress Report January - March 1980, DOE/ER-0046/1, U.S. Department of Energy, May 1980.

10. D. W. Kneff, H. Farrar IV, L. R. Greenwood, and M. W. Guinan, "Characterization of the Be(d,n) Neutron Field by Passive Dosimetry Techniques," Symposium on Neutron Cross Sections from 10 to 50 MeV, Brookhaven National Laboratory, NY, flay 1980 (to be published).

VII. FUTURE WORK

Helium analyses will be performed and cross sections determined for additional fusion reactor materials irradiated in the T(d,n) and Be(d,n)

irradiation experiments. More detailed correlations will be made between the Be(d,n) helium generation measurements and cross section evaluations from the literature, in a joint effort with ANL and LLL. The RTNS-II neutron characterization experiment will be disassembled, and the analysis of the irradiated materials will be initiated. Participation in mixed-spectrum reactor dosimetry for fusion materials test irradiations will continue.

VIII. PUBLICATIONS

The following two papers were presented at the Symposium on Neutron Cross Sections from 10 to 50 MeV, Brookhaven National Laboratory, on May 12, 1980, and the final manuscripts were submitted for publication in the proceedings:

"Characterization of the Be(d,n) Neutron Field by Passive Dosimetry Techniques," by O. W. Kneff, Harry Farrar IV (Rockwell International), L. R. Greenwood (ANL), and M. W. Guinan (LLL).

"Helium Generation Cross Sections for Fast Neutrons," by D. W. Kneff, B. M. Oliver, M. M. Nakata, and Harry Farrar IV.

I. PROGRAM

Title: Radiation Damage Analysis and Computer Simulation
Principal Investigator: Don M. Parkin
Affiliation: Los Alamos Scientific Laboratory of the University of California

II OBJECTIVE

The objective of this work is to develop displacement functions for polyatomic materials.

111. RELEVANT DAFS PROGRAM PLAN TASK/SUBTASK

SUBTASK II.B.2.3 Cascade Production Methodology
II.B.4.i Interface with other designs and other tasks
II.B.4.2 Develop theory of spectral and rate effects

IV. SUMMARY

Analysis of the net displacement functions in polyatomic materials generated using the computer code DISPLC, has shown that the displacement cascade in these materials can be described both by PKA energy and material type. Above a certain PKA energy, the nature of the displacement cascade becomes independent of the PKA atom type and below thisenergy it is a strong function of the PKA atom type. For materials whose constituents have a mass ratio near one, this energy is about 10^3 eV. For materials with a mass ratio much greater than one, this energy is about 10^5 eV. As a result of this behavior, displacement cascades in fission and fusion reactors are expected to be similar for the first case (type-1 materials) and to be quite different in the second case (type-2 materials).

V. ACCOMPLISHMENTS AND STATUS

A. Displacement Functions for Polyatomic Materials -- D. M. Parkin (LASL) and C. A. Coulter (The University of Alabama).

The nature of the displacement cascade in polyatomic materials does not lend itself to a description by a universal formula, dependent only on model and materials parameters, as is the case for monatomic materials[1,2]. To bring some order to the discussion and to help illuminate the behavior of the net displacement function $g_{ij}(E)$ we have made the following definition:

$$g_{ij} \equiv \delta_{ij} + k_{ij} f_j \nu_i / E_j^d \qquad (1)$$

where $\delta_{ij} = 1$ if $i = j$ and zero if $i \neq j$ and ν_i is the damage energy for type-i atoms in the material.[3] Equation (1) defines the displacement efficiencies k_{ij}. Using this definition we must assume in general that

$$k_{ij} = k_{ij}\,(A_i, M_i, E_i^d, E_i^b, E_{ij}^{cap}, f_i, E). \qquad (2)$$

Equation (1) is a generalization of the modified Kinchin-Pease formula to the polyatomic case. k_{ij} can be thought of as a correction function that describes the variance between the true behavior of g_{ij} and that predicted by the polyatomic damage energy for type-i atom PKAs. If Eq. (1) is a useful description of the behavior of g_{ij}, then k_{ij} will be a weak function of the parameters and display universal characteristics that describe displacement cascades in polyatomic materials.

Several other properties of Eq. (1) are pertinent. The right-hand side of Eq. (1) contains terms in ν_i and E_j^d that make g_{ij} a function of both the PKA type (type-i atoms) and the displaced atom type (type-j atoms). This occurs even if k_{ij} becomes independent of i and/or j. Thus a signature of the PKA type is maintained.

The delta function in Eq. (1) separates the PKA when $i = j$ from subsequent displacements so that k_{ij} is the efficiency for displacing atoms other than the initial recoil. The initial value of k_{ij} is thus

equal to zero. Further Eq. (1) can be rewritten as

$$K_{ij} = \bar{g}_{ij} E_j^d / f_j \nu_i \qquad (3)$$

where $\bar{g}_{ij} \equiv g_{ij} - \delta_{ij}$. Since E_j^d and f_j are constant, the energy dependence of k_{ij} reflects any failure of the damage energy to describe the nature of polyatomic displacement cascades. If the energy dependence of g_{ij} is accurately described by ν_i, then k_{ij} is a porpotionality constant between the net number of displacements other than the PKA and the damage energy multiplied by a term containing the displacement energy and the stoichiometry.

To indicate the various parameters used in the calculation, we have adopted the following notation. Materials and the corresponding parameters will be given as A_xB_y ... (E_{11}^{cap}, E_{12}^{cap}, ..., E_{21}^{cap}, E_{22}^{cap}, ...) where for a diatomic material we have A_xB_y (E_{11}^{cap}, E_{12}^{cap}, E_{21}^{cap}, E_{22}^{cap}). Because we have used $E_i^d = E_{ii}^{cap}$ and $E_i^b = 0$, this notation contains information on all the parameters used in a specific calculation.

The energy dependence of k_{ij} is characterized by the data for MgO (62,00,00,62) and TaO(60,60,60,60) in Figs. 1 and 2 respectively. The data for MgO, a material for which $M_1/M_2 \sim 1$, display the same characteristics as the equivalent result for monatomic materials (Eq. 7 in Ref. 2). The value of k_{ij} is a strong function of E from threshold to the KeV energy range where it reaches a value dependent on the material parameters. Beyond this energy range, k_{ij} retains this value and becomes roughly constant for all succeeding energies.

The behavior of TaO in Fig. 2 is essentially the same as that for MgO in Fig. 1 except for one significant difference. TaO is a material for which $m_1/m_2 >> 1$ and in this case the strong energy dependence of k_{ij} persists to about 100 keV. It is not until this rather high energy of $\sim$ 0.1 MeV is reached that k_{ij} reaches approximately a constant set of values.

By the definition of k_{ij} (Eq. 3) the necessary and sufficient condition for k_{ij} to be a constant is that $g_{ij} \propto \nu_i$. It can be seen (e.g. Figs. 1 and 2) that although k_{ij} is approximately a set of constant

values above a certain energy, it is not strictly constant. This describes the fact that g_{ij} at best is only approximately proportional to damage energy. It was shown in Ref. 2 that for monatomic materials that n(E) and g(E) are not proportional to damage energy either at low energy or high energy due to the presence of subthreshold collisions. The essential point that causes this behavior is that subthreshold collisions contribute to the damage energy but not to n_{ij} or g_{ij} However, the fact that $g_{ij} \sim \nu_i$ over a wide energy range of interest and that k_{ij} does show some universal characteristics make the use of Eq. (1) meaningful.

It is thus convenient to classify the behavior of k_{ij} into four elements. First, we can identify two energy regions for k_{ij}. In Region-1; k_{ij} is a function of energy E and in Region-2, k_{ij} is roughly independent of energy and can be approximately described by a set of constants. In Region-1, the nature of the displacement cascade is changinq as a function of energy whereas in Region-2 it has stabilized. Second we can group materials into two classes; those whose mass ratio is near one we will call type-1 materials and those whose mass ratio is much greater than one we will call type-2 material.

The consequences of the energy dependence of k_{ij} are significant for radiation effects experiments. For irradiation conditions corresponding to Region-2, PKA energies greater than $\sim$ 1 KeV for type-1 materials and PKA energies greater than $\sim$ 0.1 MeV for type-2 materials, the distribution of displacements is the same. To illustrate the relevance of this result, we note that for type-1 materials, Region-2 conditions exist both in fission reactors and in potential fusion reactors.[4] On the other hand, type-2 materials are in Region-1 in fission reactors and in Region-2 in fusion reactors. Thus the damage effects may be measurably different in the two environments for type-2 materials but the same for type-1 materials.

VI. REFERENCES

1. M. H. Norgett, M. T. Robinson, and I. M. Torrens, Nucl. Eng. Design 33, 50 (1975).
2. C. A. Coulter and O. M. Parkin, to be published in J. Nucl. Mater.
3. C. A. Coulter and D. M. Parkin, J. Nucl. Mater. 83, 249 (1980).
4. D. M. Parkin and A. N. Goland, Radiat. Effects 28, 31 (1976).

VII. FUTURE WORK

Further analysis of the nature of displacement cascades in polyatomic materials will be made.

VIII. PUBLICATIONS

1. C. Alton Coulter and Don M. Parkin, "Damage Energy Functions in Polyatomic Materials," J. Nucl. Mater 88, 249 (1980).

2. C. Alton Coulter and Don M. Parkin. "Total and Net Displacement Functions for Monatomic Materials," to be published in J. Nucl. Mater.

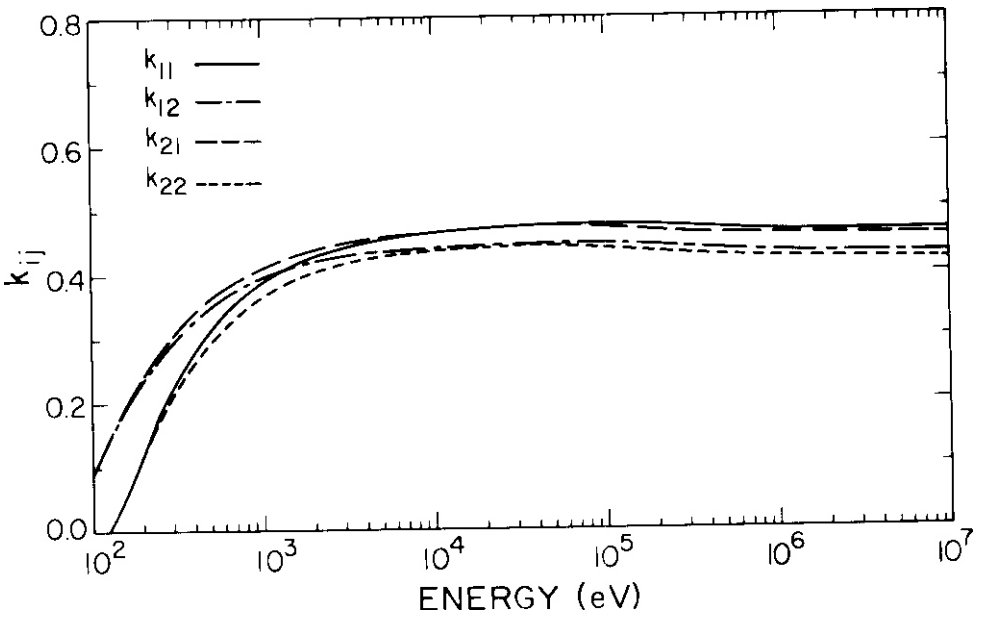

Figure 1. Values of the displacement efficiencies k_{ij} as a function of energy for the material MgO (62,00,00,62).

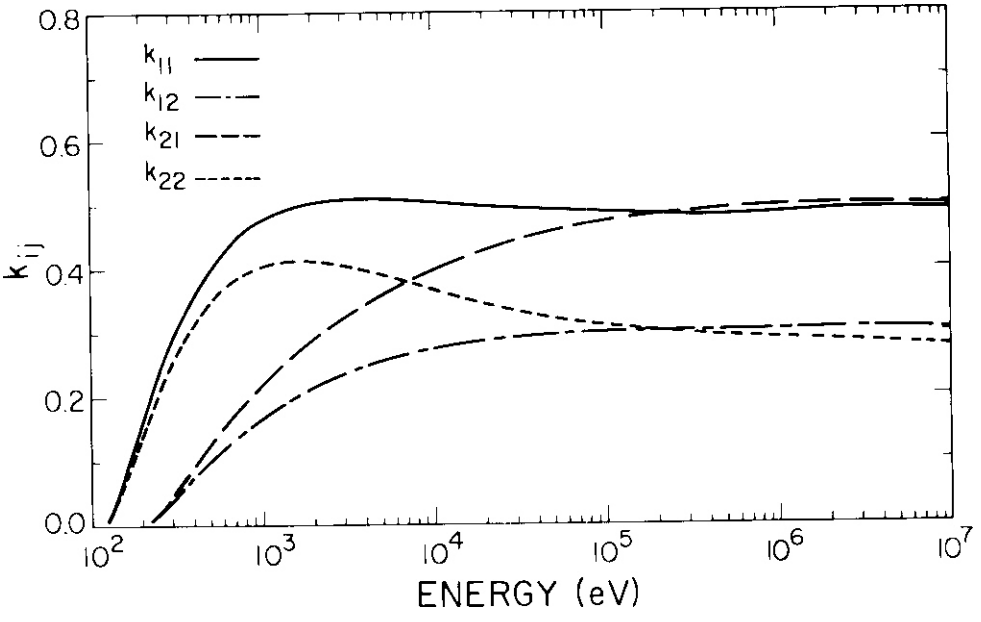

Figure 2. Values of the displacement efficiencies k_{ij} as a function of energy for the material TaO (60,60,60,60).

I. PROGRAM

Title: Damage Analysis and Dosimetry Radiation Damage Analysis
Principal Investigators: A. N. Goland and G. F. Dell
Affiliation: Brookhaven National Laboratory

11. OBJECTIVE

Radiation damage analysis studies associated with the use of electrical insulators in fusion reactors.

III. RELEVANT DAFS PROGRAMS PLAN TASK/SUBTASK

SUBTASK II.A.2.4 Flux Spectral Definition in FMIT

SUBTASK II.B.l Calculation of Displacement Cross Sections

IV. SUMMARY

An uncollided gamma ray flux estimator has been added to the MORSE Monte Carlo transport code.

The spectrum averaged electronic damage energy cross section has been evaluated for Al_2O_3 and Si_3N_4.

Spectrum average displacement cross sections have been evaluated for $MgAl_2O_4$.

V. ACCOMPLISHMENTS AND STATUS

A. Neutron Flux Characterization. Neutron flux spectra have been regenerated using a $30 \times 20 \times 20$ cm^3 test module of half density stainless steel in place of the quarter density iron test module used for previous

flux characterizations. In addition, a 0.3 cm thick target backing plate of full density stainless steel has been inserted between the volume corresponding to the lithium target and the half density stainless steel test module. These changes were made to approximate more closely current FMIT geometry.

B. Gamma-Flux Characterization. Previously reported gamma ray spectra generated with the RSIC version of MORSE using probabilistic flux estimators have been low compared to gamma ray spectra generated with the Livermore version of NORSE and gamma ray spectra generated at HEDL.[1] This discrepancy has been resolved by including in the RSIC version of MORSE an uncollided flux estimator for gamma rays. The flux determination for neutrons and gamma rays is now equivalent in that there is an uncollided and a collided component for each type of particle. The uncollided estimator for gamma rays assumes isotropic emission whereas the uncollided flu estimator for neutrons incorporates the forward peaked angular distribution of neutrons in (d,n) reactions. The gamma ray spectra generated with MORSE-L, the RSIC version of MORSE, and with NPMC at HEDL are now equivalent.

C. Damage from Electronic Processes. The energy deposited through electronic processes in Al_2O_3 and Si_3N_4 has been evaluated by using the DON code[2] to determine the spectrum average of the function $g(T) = 1-T*L(T)$. The Lindhard function is expressed as

$$L(T) = \frac{1}{1 + C_1 T^{0.15} + C_2 T^{0.75} + C_3 T}$$

with the coefficients C_1, C_2, and C_3 being those generated by Parkin and Coulter for multicomponent materials.[3]

The energy $\bar{E}_e$ deposited per gram of material through electronic processes is:

$$\bar{E}_e = n(1)\bar{\sigma}(1) + n(2)\bar{\sigma}(2)$$

where n(i) is the number of atoms of type i per gram of binary material, and $\bar{\sigma}(i)$ denotes the spectrum averaged electronic damage energy cross sections listed in Table 1. Finally, conversion of $\bar{E}_e$ to dose yields $1.66 \cdot 10^{-10}$ RADS/(n/cm^2) and $4.16 \cdot 10^{-10}$ RADS/(n/cm^2), respectively, for the first wall and FMIT spectra.

TABLE 1

ENERGY DEPOSITED THROUGH ELECTRONIC PROCESSES

	Fusion First Wall	FMIT
E_n (MeV)	3.96	10.87
Al_2O_3		
$\bar{\sigma}(Al)\left(\frac{\text{barn-eV}}{\text{atom-(n/cm}^2)}\right)$	$2.38 \cdot 10^5$	$5.78 \cdot 10^5$
$\bar{\sigma}(O)\left(\frac{\text{barn-eV}}{\text{atom-(n/cm}^2)}\right)$	$4.24. 10^5$	$9.49. 10^5$
$\bar{E}_e\left(\frac{\text{eV}}{\text{g-(n/cm}^2)}\right)$	$1.03 \cdot 10^4$	$2.36 \cdot 10^4$
$\text{DOSE}\left(\frac{\text{RAD}}{\text{(n/cm}^2)}\right)$	$1.65 \cdot 10^{-10}$	$3.78 \cdot 10^{-10}$
Si_3N_4		
$\bar{\sigma}(Si)\left(\frac{\text{barn-eV}}{\text{atom-(n/cm}^2)}\right)$	$2.26 \cdot 10^5$	$5.66 \cdot 10^5$
$\bar{\sigma}(N)\left(\frac{\text{barn-eV}}{\text{atom-(n/cm}^2)}\right)$	$4.60 \cdot 10^5$	$1.09 \cdot 10^6$
$\bar{E}_e\left(\frac{\text{eV}}{\text{g-(n/cm}^2)}\right)$	$1.08 \cdot 10^4$	$2.60 \cdot 10^4$
$\text{DOSE}\left(\frac{\text{RAD}}{\text{(n/cm}^2)}\right)$	$1.66 \cdot 10^{-10}$	$4.16 \cdot 10^{-10}$

D. Recoil-atom Damage in $MgAl_2O_4$. The displacement functions of Parkin and Coulter[4] have been used in the damage code DON to evaluate recoil-atom damage in $MgAl_2O_4$. Nine separate evaluations are neccssar) to determine the cross section $\bar{\sigma}(i,j)$ for displacing each species of atom by each species of pka. The total displacement. cross section for each species of atom is obtained from a weighted sum of the contribution from each species of pka:

$$\bar{\sigma}(i) = \sum_{j=1}^{3} p(j)\bar{\sigma}(i,j)$$

where p(j) is the atomic fraction of atoms of type j in the ternary material. Results for $MgAl_2O_4$ are given in Table 2 .

TABLE 2
SPECTRUM AVERAGED CROSS SECTIONS FOR $MgAl_2O_4$
$E_d(Mg)$ = 86 eV, $E_d(Al)$ = 77 eV, and $E_d(O)$ = 130 eV.[4]

	Fusion First Wall	FMIT
$\bar{\sigma}$(Mg) barn/atom	55.14	80.21
$\bar{\sigma}$(Al) barn/atom	123.9	180.8
σ(O) barn/atom	131.0	189.7
σ_H (mb/atom)	21.2	35.8
σ_{He} (mb/atom)	46.4	04.5

VI. REFERENCES

1. A. N. Goland, H. C. Berry, G. E. Dell, and O. W. Lazareth, Damage Analysis and Fundamental Studies Quarterly Technical Progress Report, October-December 1979, p. 42, DOE/ET-0065/8.

2. D. M. Parkin and A. N. Goland, Radiation Effects 28, 31 (1976).

3. C. A. Coulter and D. M. Parkin, Journal of Nuclear Materials 88, 249 (1980).

4. D. M. Parkin and C. A. Coulter, Damage Analysis and Fundamental Studies Quarterly Technical Progress Report, January-March 1978, p. 113, DOE/ET-0065/1.

VII. FUTURE WORK

Future work will include evaluation of damage in multicomponent materials exposed to several neutron spectra of interest to the DAFS effort.

VIII. PUBLICATIONS

A paper entitled "Damage Parameters for Non-Metals in a High Energy Neutron Environment" was presented at the Symposium on Neutron Cross Sections from 10-50 MeV held from May 12-14, 1980, at Brookhaven National Laboratory.

I. PROGRAM

Title: Irradiation Effects Analysis (AKJ)
Principal Investigator: D. G. Doran
Affiliation: Hanford Engineering Development Laboratory

11. OBJECTIVE

The objective of this work is to develop computer models for the simulation of high energy cascades which will be used to generate defect production functions for correlation analyses of radiation effects.

III. RELEVANT OAFS PRAGRAM TASK/SUBTASK

SUBTASK 11.8.2.3 Cascade Production Methodology

IV. SUMMARY

Computer models have been developed for the simulation of high energy displacement cascades. The objective is the generation of defect production functions for use in correlation analysis of radiation effects in fusion reactor materials. In particular, the stochastic cascade annealing simulation code SCAS has been developed and used to model the short-term annealing behavior of simulated cascades in FCC metals. The code is fast enough to make annealing of high energy cascades practical. Sets of cascades from 5 keV to 100 keV in copper were generated by the binary collision code MARLOWE.

In order to simulate the recombination occurring during the localized quenching of the highly excited cascade region, an effective spontaneous recombination radius was applied to reduce the number of defects to be consistent with values measured at 4K. The individual cascades were then annealed with SCAS and examined at stages of short-term annealing corresponding approximately to Stage I and Stage III. The total number of surviving defects in an isolated cascade produced at any temperature is proportional to the damage energy for cascade energies above 5 keV. Comparison is also made with previous cascade annealing simulations.

V. ACCOMPLISHMENTS AND STATUS

Simulation of Short-Term Annealing of Displacement Cascades in FCC Metals - H. L. Heinisch, Jr. (HEOL)

1. Introduction

The characterization of bulk radiation damage in the first wall of a fusion reactor requires an understanding of the high energy recoils, on the order of hundreds of keV, which result from the typical fusion reactor neutron spectrum. Theoretical models are being developed with the objective of generating defect production functions for use in correlation analysis of radiation effects in potential fusion reactor materials. These models treat the problem on an atomistic scale, with various levels of approximation to the physical processes involved depending primarily on the energy range of the recoils under consideration.

Previous atomistic modeling work which culminated in the determination of defect production functions[1-3] was aimed at understanding radiation effects in breeder reactor spectra, which do not have the large component of high energy neutrons of the fusion reactor spectrum. The earliest work at this laboratory used displacement cascades generated by Beeler;[4] more extensive cascades were generated later with an early version of the binary collision code MARLOWE.[5] The simulation of short-term annealing of the cascades was done with the hybrid annealing program HAP. The modeling was used to obtain defect production functions which could be integrated with a primary knock-on atom (PKA) spectrum to find the mean numbers of defects per PKA. Multiplying by the PKA production cross section for a particular incident particle results in defect production cross sections for the particle.

The earlier work is being extended for several reasons. PKAs of energy as large as 100 keV were treated explicitly earlier, but with some difficulty, because of the large amount of computer time necessary to anneal the high energy cascades with HAP. Defect production for PKAs above 100 keV was extrapolated from the lower energy information. The MARLOWE cascades used in the earlier work were generated in copper using a displacement energy, E_d, of 25 eV, that is, only atoms receiving at least 25 eV of energy were allowed to participate in the cascade. (In the context of this report the terminology "displacement energy" refers to this MARLOWE parameter and not necessarily to the energy needed to form a stable Frenkel pair.) This

criterion effectively prevents the occurence of the long replacement collision sequences (LRS) that are observed in dyndmical computer simulations[6] and inferred from experimental evidence.[7] The low energy collisions which occur in replacement events can be included in MARLOWE by lowering the displacement energy parameter to something on the order of 5 eV.[7] Unfortunately, this also allows so many more atoms to participate in the cascade that the capacity of a large computer is saturated for *PKAs* of 40-50 keV in copper.

This report describes briefly recent advancements which now make possible the modeling of the higher energy displacement cascades resulting from the fusion reactor spectrum. The new stochastic cascade annealing simulation code SCAS simulates the short-term annealing of cascades with such economy that statistically significant numbers of high energy cascades (hundreds of keV) can be considered. Continued refinement of MARLOWE parameter settings[7] has produced a model which has a more fundamental physical basis. Also, unlike the previous work, the modeling is fitted to the actual defect yields extracted from resistivity measurements on low temperature ion-irradiated materials.[9]

Results of simulations using SCAS and improved MARLOWE cascades at energies up to 100 keV in copper are presented and discussed, along with a comparison with the previous work.

2. Annealing Simulation and Cascade Generation

The stochastic cascade annealing simulation code SCAS and its calibration against the results of the HAP code are described in more detail elsewhere.[8] Besides using improved computational techniques, SCAS employs some simplifying approximations to the more physically rigorous details of defect movement employed in HAP. In SCAS the defect clusters are assumed to be spherical and centered on lattice sites. Mobile defect clusters (mono-, di-, tri-, tetra-vacancies; mono-, di-, tri-interstitials) move as a whole, one lattice site at a time, while in HAP, the integrity of the individual point defects was maintained even when clustered. In SCAS the mobile defects are followed until they leave the "cascade region," defined here as the rectangular parallelpiped which encloses the initial cascade plus a margin of 25 lattice parameters in each direction. To check the SCAS code, it was used on the same sets of cascades as annealed previously with HAP, using critical reaction distances and jump frequencies which are consistent with the corresponding parameters in HAP.

SCAS gives results remarkably similar to HAP with only about 5% of the expenditure of computer time. With SCAS it is now computationally feasible to anneal sets of cascades with energies of hundreds of keV. With the ability to anneal large cascades realized, the computational limitation rests more with the generation of the high energy cascades using MARLOWE.

With the proper choice of parameter settings, MARLOWE has been made to model PKAs with energies less than 100 eV,[8] even though it employs the binary collision approximation. It gives replacement sequences with lengths comparable to those produced in simulations using the many-body dynamical code COMENT with the same interatomic potential. The parameter settings for this low energy version of MARLOWE, which uses a displacement energy of 5 eV, can be used for PKAs up to about 40 keV. Above that, a higher displacement energy must be used to reduce the number of defects produced.

Defect production "efficiency" experiments[11] have shown that, at cascade energies above a few keV, fewer Frenkel pairs remain than are predicted by partitioning the damage energy into an effective energy necessary to displace an atom from its lattice site [e.g., the modified Kinchin and Pease model[12]]. The experiment temperatures are such that both interstitial and vacancies are immobile with respect to normal thermally activated migration, thus the yields observed must be due to recombination during localized "quenching" of the excited cascade region. That is, excitation resulting from the energy localized in the cascade region after all initial displacements occur is thought to lead to immediate athermal rearrangement of the atoms, resulting in considerable pair recombination. This phenomenon has been observed in computer simulations of cadcades in tungsten.[13] The MARLOWE code cannot model this aspect of the cascade development directly, hence MARLOWE predicts far too many defects. To account for the recombination which takes place during the quenching of the cascade, the simplest procedure is to recombine the closest pairs until the experimentally observed number has been reached. In the earlier work[2] spontaneous recombination volumes, determined from static modeling and some experimental evidence, were applied to the MARLOWE cascades. Even with a displacement energy of 25 eV, these cascades had many more defect pairs remaining after recombina-

tion thanobserved in the more recent experiments. The present procedure is to apply whatever amount of recombination is necessary to make the number of defects consistentwith values extracted") from resistivity measurements on low temperature, ion irradiated samples.[11] A single, energy-independent, effective recombination radius of 3 lattice parameters, applied to the MARLOWE cascades having E_d = 17 eV, gives Frenkel pair yields consistent with the resistivity measurements in the range from 5 to 100 keV. The value 17 eV is about the minimum displacement threshold obtained with the interatomic potential used in this work. A larger, also energy independent radius of 5.5 lattice parameters was applied with equal success for the low displacement energy (E_d = 5 eV) MARLOWE model throughout the 5 keV to 30 keV range. This effective recombination radius may seem quite large. However, in a computer simulation study of Frenkel pairs in *electron*-irradiated copper by Tenenbaum,[14] an "attraction range" was determined for Frenkel pairs which is larger than the spontaneous recombination radius. Within the attraction range newly produced interstitials activated by local heating of the lattice tend to jump toward the vacancies. This activation range was estimated to be 5.4 lattice parameters at 0 K.

Raising the displacement energy E_d to permit the simulation of higher energy cascades necessitates a procedure to account for the truncation of LRS.[10] Sets of cascades in the energy range from 5 to 30 keV were generated using MARLOWE with displacement energies of both 5 and 17 eV. Both sets were annealed with SCAS, and the results were compared at two stages of annealing: 1) after a time τ = 1000 jumps, corresponding to 1000 jumps of a single interstitial, i.e., after near exhaustion of the nobile interstitials from the cascade region, and 2) at τ = *END* after all mobile vacancies and interstitials had escaped the cascade region ($\sim 10^{12}$ jumps). Multiplicative scaling parameters were then determined for converting defect yields from the high E_d model to be the same as those for the low E_d model.

The relative jump frequencies used in the annealing runs were the same as those used in HAP. They correspond to a temperature of about 800 K in gamma-iron. These jump frequencies for single interstitials and vacancies differ by a factor of about 10^7. A few test cases have shown the

outcome to be fairly insensitive to the jump frequencies. Thus, we prefer to discuss our results in terms of mechanisms rather than temperatures. We identify the motion of interstitials with Stage I annealing and the motion of vacancies approximately with Stage III.

3. Results

Using a displacement energy of 17 eV, sets of ten MARLOWE (Version 11) cascades were generated at energies of 5, 20, 30, 60 and 100 keV. The defect yields per cascade were adjusted to be similar to those expected from the low displacement energy model by using the calibration factors. In Figure 1 the number of Frenkel pairs are plotted versus the average damage energy computed directly (Lindhard energy partition model) in the MARLOWE runs. The results are plotted for three stages of annealing: at τ = 0 (recombined but not annealed), τ = 1000 jumps, and τ = END. The curve for τ = 0 is a function derived from resistivity data.[9] It is nearly linear in this energy range. The curves for τ = 1000 and τ = END are simply the τ = 0 curve multiplied by 0.87 and 0.70 respectively. The error bars are one standard deviation, based on ten cascades at each point. Thus, in the energy range from 5 to 100 keV the number of pairs remaining after annealing is simply a fraction, independent of energy, of the initial number of defects

Over a lower range of PKA energies there is a transition in the nature of defect production, as the energy is increased, from the production of a small number of isolated pairs per PKA to the production of cascades in which considerable recombination occurs. In Figure 2 the average number of defects per unit damage energy is plotted versus damage energy for recombined but unannealed MARLOWE cascades. The curve, calculated from τ = 0 in Figure 1, is extended to somewhat smaller energies to illustrate the sharpness of the transition region. From this figure the high end of the transition region can be said to lie somewhere between 5 and 20 keV. Above 20 keV the defect production efficiency is nearly constant with energy.

4. Discussion

Many characteristics of the new cascades, produced by a version of MARLOWE which has been calibrated against many-body dynamical simulations, are independent of energy in the range of PKA energies from 5 to 100 keV.

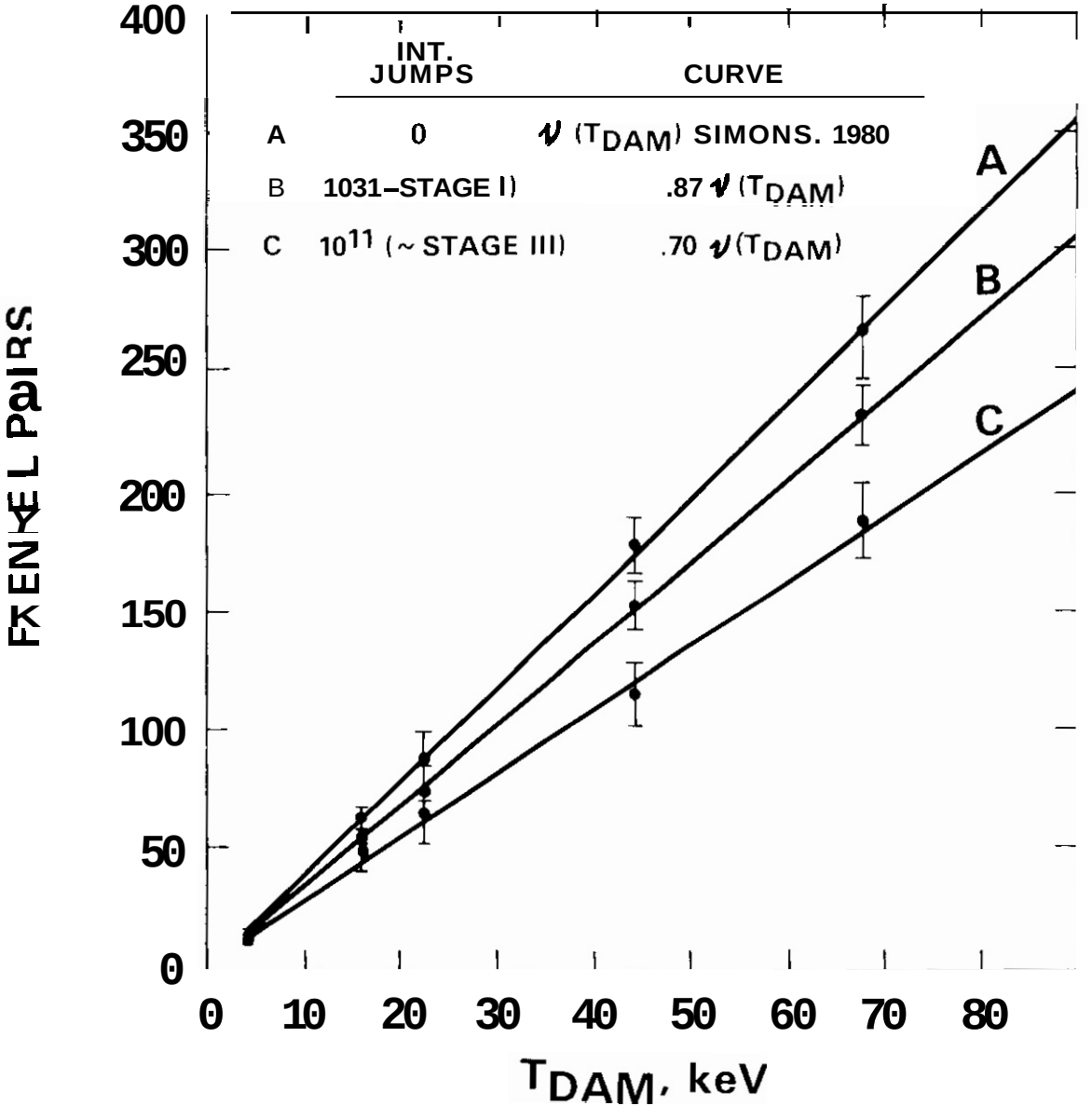

FIGURE 1. The Number of Frenkel Pairs Remaining at Three Stages of Simulation Annealing as a Function of Damage Energy. The top curve was extracted by Simons from resistivity data (Reference 8).

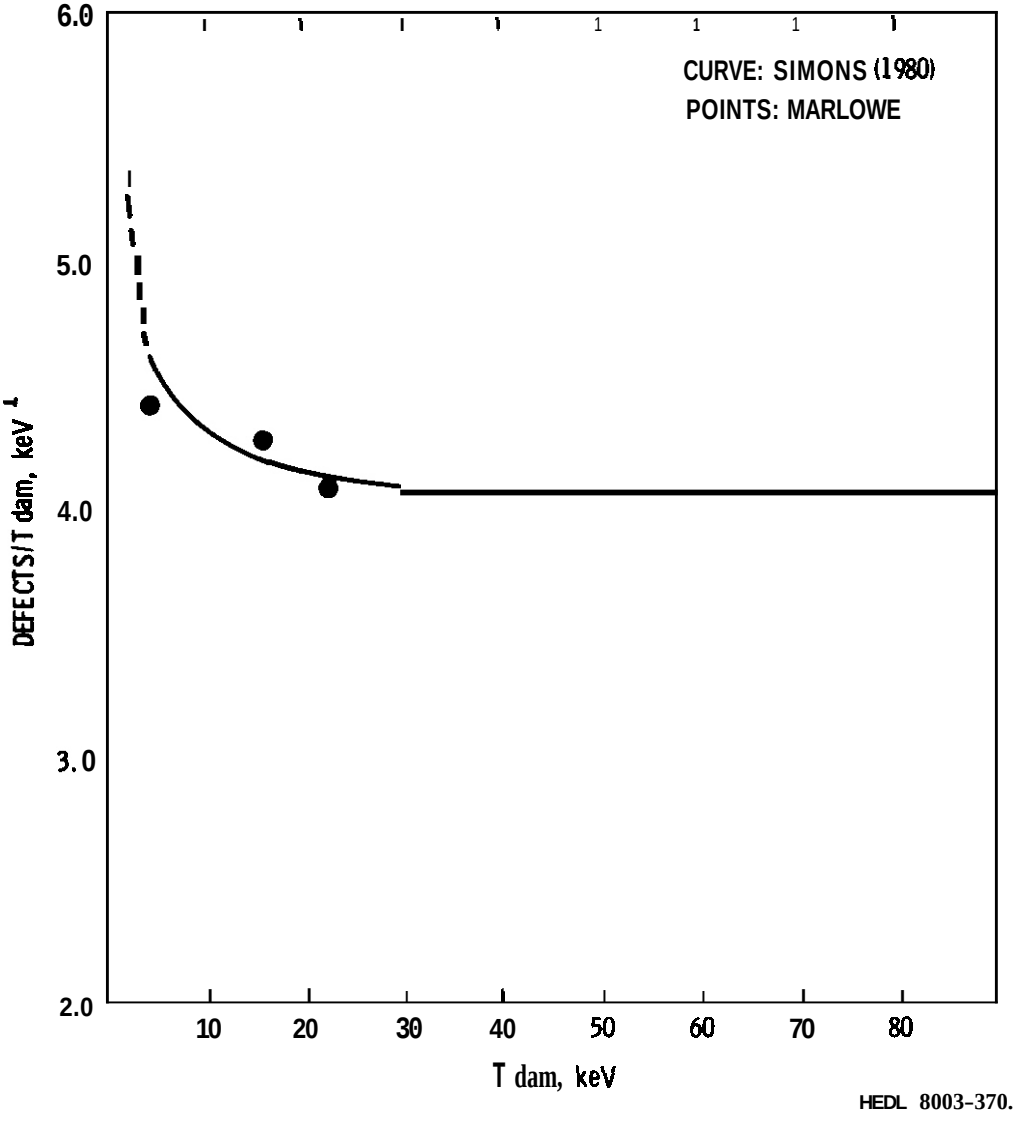

FIGURE 2. Defect Production Efficiency, Expressed as Total Frenkel Pairs Per Unit Damage Energy, as a Function of Damage Energy.

For cascades produced using either a high E_d or low E_d, an effective recombination radius independent of damage energy produced defect pair yields consistent with resistivity measurements. At two stages of simulated short-term annealing the residual fraction of original defect pairs is independent of damage energy. The efficiency of defect production, measured by the number of defect pairs per unit damage energy, is fairly uniform above 5 keV (perhaps more so above 20 keV). An explanation for this behavior is that, above about 5 keV, the density of defects in cascades is independent of PKA energy and remains so after short-term annealing. This behavior should make for easy extrapolation to cascades of much higher energy.

The formation of subcascades, i.e., multiple, spatially separated cascade regions produced by the same PKA, could be expected to result in the observed nearly constant defect production efficinecy at high energies. However, initial analysis of the spatial extent of the fifty cascades produced for this study reveals only two cascades, at 30 and 100 keV, that had widely separated damage areas. In both cases the secondary damage area was quite small and quickly annealed out. Graphical analysis in progress of these and higher energy cascades will produce valuable insights into the reasons for the energy independent characteristics.

It is of interest to compare the present results with the defect production functions developed in the previous annealing study. In that work cascades were generated with an older version of MARLOWE, using E_d = 25 eV. No provisions were made for including effects of LRS in these MARLOWE cascades. With a higher E_d value the average pair separation is smaller; hence, more recombination and smaller yields than those obtained in the present study might be expected as these cascades were annealed. On the other hand, the initial number of pairs was not reduced by recombination sufficiently to give the "measured" values used in the present work. Also, because of different criteria in determining the end of an annealing simulation, the previous cascades were perhaps not annealed completely. These factors would tend to result in somewhat larger yields. These contrasting effects evidently compensate for each other. The result, shown in Figure 3, is that the present simulation values fit the previous defect production functions surprisingly well. If the present results using E_d = 17 are not

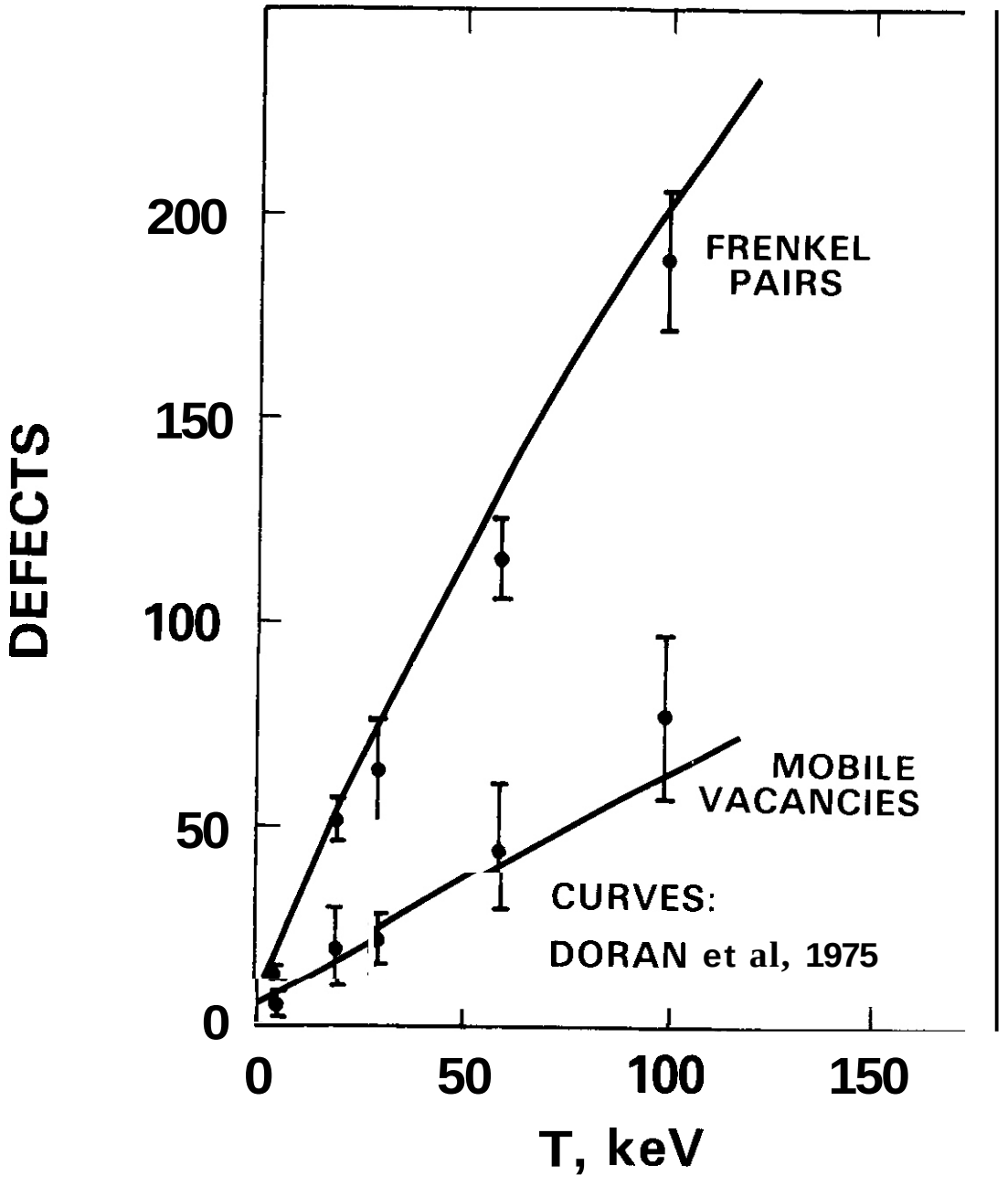

FIGURE 3. Comparison of Defect Production Functions (Smooth Curves) of Reference 1 With Present Results.

adjusted by the calibration factors to account for LRS, then they differ from the old defect production functions by about 30%.

The comparison with the earlier results suggests that an alternate method of calibrating defect yields from anneals of high E_d MARLOWE cascades would be to increase the pre-anneal number of defects by decreasing the recombination radius. Because this procedure would have the advantage of maintaining, at least approximately, the appropriate spatial configuration of all the residual defects, it is being investigated. In the current procedure, the number of defects is adjusted upward but the location of the "added" defects is unknown.

The short-term annealing of isolated cascades should be comparable to the annealing of resistivity in specimens exposed to low dose, cascade-producing radiation, at least through Stage I where the recovery mechanisms are relatively straightforward. Recovery of resistivity at the end of Stage I for low dose, 4 K irradiation of copper by 400 keV Bi^{++} ions, has been measured[14] to be 15%. The PKA spectrum corresponding to this irradiation is such that only negligible displacements are produced below 5 keV. If one assumes the curves in Figure 1 can be extrapolated to several hundred keV, for comparison with this experiment, then at $\tau = 1000$ all cascades above 5 keV will have recovered by 13%. Thus, good agreement with experiment has been obtained for at least the initial stages of the short-term annealing simulation.

5. Conclusions

The simulation of displacement cascades in copper in the 5 to 100 keV range has produced the following conclusions:

1) The total number of surviving defects in an isolated cascade produced at any temperature is proportional to the damage energy for cascade energies above about 5 keV.

2) The fractions of vacancies and interstitials which are free are essentially constant over the same energy region.

3) No firm evidence for subcascadc formation has been found, although comprehensive graphical analysis has not yet been performed.

VI. REFERENCES

1. Doran, D. G., Simons, R. L. and McElroy, W. N., "Spectral Effects in Neutron and Charged Particle Irradiations," Properties of Reactor Structural Alloys After Neutron or Particle Irradiation, ASTM STP 570 (1975) pp. 290 - 310.

2. Doran, D. G. and Burnett, R. A., "Computer Simulation of the Short-Term Annealing of Displacement Cascades," Interatomic Potentials and Simulation of Lattice Defects, P. C. Gehlen, J. R. Beeler, Jr. and R. I. Jaffee, eds., Plenum Press, N. Y. (1972) p. 403.

3. Beeler, J.R., Jr., J. Testing and Evaluation, 3, (1975) p. 230.

4. Beeler, J. R., Jr., Phy. Rev., 150 (1966) p. 150.

5. Robinson, M. T. and Torrens, I. M., Phys. Rev. B, 9 (1974) p. 5008.

6. Schiffgens, J. O., Schwartz, D. M., Ariyasu, R. G. and Cascadden, S. E., Rad Eff., 39 (1978), p. 221.

7. Blewitt, T. H., Kirk, M. A. and Scott, T. L., "Replacement Sequences in Metals," Fundamental Aspects of Radiation Damage in Metals, M. T. Robinson and F. W. Young, eds., CONF-751006, 1, p. 152.

8. Robinson, M. T., DAFS Quarterly Progress Report, January - March 1980, DOE/ET-0065/9, U. S. Department of Energy, in press.

9. Simons, R. L. DAFS Quarterly Progress Report, January - March 1980, DOE/ET-0065/9, U. S. Department of Energy, in press.

10. Heinisch, H. L., Jr., DAFS Quarterly Progress Report, October - December 1979. DOE/ET-0065/8, U. S. Department of Energy (1980) p. 49.

11. Averback, R. S., Benedek, R., and Merkle, R. L., J. Nuc. Mat., 69 and 70 (1978) pp. 786 - 789.

12. Norgett, M. J., Robinson, M. T., and Torrens, I. M., Nuc. Eng. and Design, 33 (1975) pp. 50 - 54.

13. Guinan, M. W., Stuart, R. N., Kinney, J. H. and Violet, C. E., DAFS Quarterly Progress Report, April - June 1979, DOE/ET-0065/6, U. S. Department of Energy (1979) p. 71.

14. Tenenbaum, A., Rad. Eff., 39 (1978) pp. 119 - 122.

15. Averback, R. S., Thompson, L. J. and Merkle, K. L., J. Nuc. Mat, 69 and 70 (1978) pp. 714 - 719.

VII. FUTURE WORK

Higher energy cascades will be generated and short-term annealed. The interaction of cascades during short-term annealing will be investigated with the newly developed annealing code ALSOME.

VIII. PUBLICATIONS

This work is to be published as part of the Proceedings of the ASTM Tenth International Symposium on Effects of Radiation on Materials, Savannah, GA, June 3 - 5, 1980.

CHAPTER 3

FUNDAMENTAL MECHANICAL BEHAVIOR

I. PROGRAM

Title: Simulating the CTR Environment in the HVEM

Principal Investigators: W. A. Jesser and R. A. Johnson

Affiliation: University of Virginia

II. OBJECTIVE

The objective of this work is to investigate the effects of precipitates on crack propagation in aged helium irradiated type 316 stainless steel.

III. RELEVANT DAFS PROGRAM TASK/SUBTASK

Task **II.C.14.2** Fundamental relations between microstructure and fracture mechanisms.

IV. SUMMARY

An HVEM specimen of type 316 stainless steel, irradiated to a dose of $\sim 1 \times 10^{17}$ ions/cm^2 (below the critical dose for the formation of visible helium bubbles), was subsequently aged in vacuum at 900°C for 38 minutes. During this post-irradiation aging process, large rod shaped and irregular shaped precipitates ($\leq \sim 1\mu$) formed in the matrix and on grain boundaries. Helium filled bubbles were also observed to have formed; bubbles on the precipitate/matrix interface had a mean diameter of 9 nm as compared to 3.5 nm for bubbles in the matrix. The precipitates were identified as having a bcc crystal structure with a lattice constant, $a = 8.87 \pm .08\text{Å}$; they belonged to a chi phase, rich in Mo and Cr, and Ni and Fe deficient in comparison to the matrix. During tensile tests, at 900°C and at 25°C, these precipitates apparently did not serve as crack initiation sites.

Precipitates on a grain boundary were observed to have sheared crystallographically and to have necked down under stresses generated during the aging process.

V. ACCOMPLISHMENTS AND STATUS

HVEM observations of Crack Propagation in Helium Irradiated Type 316 Stainless Steel Containing Precipitates, J. I. Bennetch, R. D. Gerke, and W. A. Jesser, Department of Materials Science, University of Virginia, Charlottesville, Virginia 22901.

1. Introduction

It is possible during the lifetime of a reactor component that, due to the presence of a high supersaturation of point defects, normally unstable second phase particles may form on grain boundaries and limit ductility. The nature of intergranular crack propagation in such a case may be changed from that usually found in intergranular failure. The intent of this report is to provide further insight into the mechanisms of crack propagation by HVEM examination of microscopic cracks in a type 316 stainless steel specimen implanted with helium and aged to produce precipitate particles.

2. Experimental Details

A thin HVEM tensile specimen of solution annealed type 316 stainless steel, was irradiated in-situ with a flux of 3.5×10^{14} ions cm^{-2} sec^{-1} of 80 keV He^{+} ions at ambient temperature to a fluence of 1×10^{17} ions cm^{-2}. No irradiation-induced helium filled bubbles were visible in the HVEM at that low dose and temperature. No visible oxide film was seen on the foil surface exposed to the ion beam. The sample was then removed and placed in a high vacuum ion pumped system to be aged at 900°C in a quartz tube furnace for 38 minutes. After the

completion of the aging treatment, second phase particles were observed, as well as numerous cracks, and small helium filled bubbles. The sample was then tension tested to failure at room temperature.

3. Results and Discussion

a. Identification of Precipitates

In order to identify the precipitates, a post failure examination of the sample in a high resolution Philips EM 400 with an x-ray energy dispersive analyser was carried out. Careful attention was given *to* crystal morphology, structure, and chemical composition. The phases normally found at 900°C in 316 stainless steel are carbides such as $M_{23}C_6$, M_6C, and intermetallic phases denoted as σ and χ.

1. Crystal morphology

The appearance of these particles ranged from a rod shape to a more massive irregular shape. They occurred intragranularly as well as on grain boundaries. A definite orientation relationship between $M_{23}C_6$ carbide particles and the austenite matrix [1,2,3] has been reported to be:

$$\{100\}\gamma \,||\, \{100\}_{M_{23}C_6}$$

$$\langle 100\rangle\gamma \,||\, \langle 100\rangle_{M_{23}C_6},$$

Although σ particles also often obey an orientation relationship with the matrix [4,5] of the type

$$\{111\}\gamma \,||\, \{100\}\sigma$$

$$\langle 011\rangle\gamma \,||\, \langle 140\rangle\sigma,$$

no such simple relationship existed between the austenitic matrix plane

of (011) and the broad face of the particles. As an illustration of the particle/matrix orientation relationship in the present work, figure 1 shows a micrograph of three rod shaped and irregular shaped precipitates (labeled A, C and D) with their corresponding SAD patterns. The pattern for the matrix is labelled B. Each pattern was obtained by tilting the specimen until its zero order Laue zone appeared. Because the electron beam direction is different for each one of the four patterns, there was no simple orientational relationship between precipitate D and the matrix, even though they exhibit the same diffraction pattern. These diffraction patterns at-e indexed in figure 2.

2. Crystal Structure

S.A.D. patterns from a number of intragranular precipitates in different orientations were compiled and analyzed in order to compute d_{hkl} spacings for these particles. Only one useable grain boundary precipitate pattern was obtained from the particles in figure 1, since they were, in general, too thick for distinct patterns to be produced. A summary of the results is tabulated in table 1. In this table, experimental d_{hkl} values are contrasted to those values for $M_{23}C_6$, M_6C, σ and χ. All four of these phases are commonly found in unirradiated 316 stainless steel aged at high temperatures, but normally at 900°C $M_{23}C_6$ is the only phase to appear in 40 minutes [10]. However, the d_{hkl} data in table 1 suggest instead that the precipitates possess a bcc structure with a lattice constant, a = 8.87 ± .08Å. The angles between the planes so indexed also agree quite closely (within ~1°).

that of the austenitic matrix here and the nominal type 316 stainless steel composition. To avoid solute segregation effects, the x-ray scan for the matrix was taken in the grain far from the precipitates. From the table, one can see that the results for the matrix are consistent for the most part with the nominal composition for type 316 type stainless steel. The presence of a comparitively large amount of silicon in the matrix (and thus in the precipitates) is possibly due to silica deposited from the quartz annealing furnace.

A number of observations concerning the intragranular and grain boundary precipitates are apparent. Regardless of shape or position, the precipitates are chromiuni and molybdenum enriched at the expense of iron and nickel. Despite some differences in the concentration of molybdenum (a minor constituent), since the concentrations of the rest of the components are fairly consistent, one can conclude that each type of precipitate has closely the same major chemical composition. Thus this is further evidence that these particles are all the same phase. Further, because the composition of the chi phase (which can contain Mo, Cr, Fe and Ni) has been found to vary appreciably, since it has a high tolerence for metal exchange [10,12], one can be reasonably sure that the unknown precipitate is a chi phase.

TABLE 2

CHEMICAL COMPOSITION OF PRECIPITATES AND MATRIX VS. NOMINAL TYPE 316 STAINLESS STEEL (Weight %)

Area Analysed	Si	Cr	Mn	Fe	Ni	Mo
	2.3	20	0.2	62	14	2.2
"Irregular" shaped precipitate (matrix)	1.8	33	0.2	53	6.2	5.1
precipitate (matrix)	2.6	31	0.3	52	6.4	8.2
	2.8	31	0.4	50	6.2	10
Nominal type 316 stainless steel composition	1.00max	16-18.00	2.00max	balance	10-14.00	2.00-3.00

b. Effect of Precipitation on Radiation-Induced Microstructure

Normally when one injects a large amount of helium into a sample of type 316 stainless steel (SS) and then anneals (or ages) it above a certain temperature for a long enough time, helium filled cavities nucleate and grow in the sample interior. Annealing experiments on 17-17 SS were carried out by Braski et al. on stressed and unstressed samples that were implanted with He to a total concentration of 158 appm and subsequently annealed at 750°C for times as long as 480 hours. No mention is made of aged induced precipitation in this reference. Bubbles were produced in unstressed samples that grew as

large as 1.7 nm in diameter ($\rho \simeq 2 \times 10^{15} cm^{-3}$) in the grain matrix and ~6 nm in diameter ($\rho \simeq 4 \times 10^{10} cm^{-2}$) on grain boundaries after 217 hours [13]. The results of Braski's annealing experiment can be compared to the present work where a type 316 SS sample implanted with helium to a higher fluence of $10^{17} cm^{-2}$ ($\leq$ 1300 appm helium for a foil 100 nm thick) was annealed at a higher temperature (900°C) for a shorter time (38 minutes). Despite the higher concentration of helium in the sample, bubbles in the matrix grew only to ~3.5 nm diameter ($\rho \simeq 5 \times 10^{15} cm^{-3}$), smaller than the matrix bubbles in Braski's work. In contrast, larger bubbles grew at the matrix/precipitate interface than either Braski's grain boundary or matrix bubbles, ~9 nm on the average ($\rho \simeq 3 \times 10^{10} cm^{-2}$) with large fluctuations in diameter (some with bubble diameters as big as 30 nm). This result suggests that precipitate particles act to suppress bubble growth in the grain interior.

c. Effect of Precipitation on Ductility

In order to determine the effect of precipitate particles on ductility, an effort was made to characterize microscopic cracks in an HVEM. The crack opening angle and the crack's plastic zone width perpendicular to the crack flanks have been shown to be measures of ductility [14,15]. In addition, an examination of how the precipitate particles themselves behave as a crack advances is an indication how ductile a material is. In order to accomplish this goal of measuring ductility, a comparison was made of cracks that formed in this He irradiated type 316 stainless steel sample during the 900°C

aging treatments with cracks forming and propagating in a highly ductile unirradiated solution annealed type 316 stainless steel sample as well as those from a highly brittle neutron irradiated type 304 stainless steel sample. Both latter cases were tested at 600°C and did not contain visible second phase particles.

A summary of crack angle and zone widths and lengths is found in table 3. There one sees the aged sample contained both transgranular (T) and intergranular (I) cracks (Cases #1 and #2) in contrast to the extremely ductile unirradiated Case #3 (which only contained T cracks). However, T cracks for the aged case (Case #1) had crack angles and zone sizes quite similar for those T cracks in the unirradiated case (Case #3). In addition, the intergranular crack in the aged case (Case #2) had a large crack angle and zone size as compared to the brittle neutron irradiated case (Case #4). A ductile intergranular crack can be seen in figure 3, an HVEM micrograph of an intergranular crack decorated with precipitates (Case #2) from the aged helium irradiated sample. As can be seen, the χ phase intergranular precipitates have physically deformed in what appears to be a crystallographic mode. (The precipitates were too thick to obtain a distinct SAD pattern.) In addition, two particles have necked down. The associated strains for three of these particles range from 1.1-2.6, showing their large ductility at 900°C. In contrast to this behavior, transgranular cracks in this sample apparently bypassed the precipitate particles altogether.

TABLE 3

A COMPARISON OF CRACKS FORMED IN HELIUM IRRADIATED AGED TYPE 316 STAINLESS STEEL WITH THOSE CRACKS IN UNIRRADIATED TYPE 316 STAINLESS STEEL AND NEUTRON IRRADIATED 304 TYPE STAINLESS STEEL

	Treatnient			
	Aged Helium Irradiated		Unirradiated [13]	Neutron Irradiated I131
	Case #1	Case #2	Case #3	Case #4
1. Crack type	T	I	all T	all I
2. Crack angle	∿25°	8"	10-30°	2°
3. Plastic zone length	>4μm	5μm	≥10μm	∿0μm
4. Plastic zone width	0.75μm	≥0.2μm	width indistinct (>1μm)	∿0μm
5. Test temp.	900°C*	900°C*	600°C	600°C

*Cracks formed during aging process.

In the previous section, it has been reported that helium preferentially collects as bubbles at precipitate/matrix interfaces. However, since the grain boundary precipitate particles necked down to failure, rather than separating at the precipitate/matrix interface, one can conclude the presence of helium bubbles on the interface does not contribute in a catastrophic way to the deformation process at high temperature or at low temperature.

Contrary to what is usually expected for mechanisms of fracture, the hole that developed in front of this crack, as illustrated in figure 3, apparently did not initiate at a second phase particle. Instead, one can see lighter areas that have thinned in spaces between

particles on the boundary in front of the crack tip. I. Chan, in studying an aged Al-CU alloy system containing precipitates also noted that void nucleation did not necessarily occur at second phase particles, but rather at dislocation cell walls [It-]. Numerous other experimentalists have made similar observations concerning void nucleation and second phase particles [17-21].

Transgranular cracks parallel to that intergranular crack illustrated in figure 3 became operative when the sample was tensile tested to failure at 25°C after aging. This indicates that at lower temperatures the intergranular precipitate particles were much stronger than the helium filled matrix.

4. Conclusions

a. The presence of large amounts of helium in type 316 stainless steel can lead upon aging at 900°C to the formation of a chi phase.

b. Helium bubbles formed at 900°C at the precipitate/matrix interface have a much larger mean diameter than for those found in the grain interior.

c. Cracks along grain boundaries containing chi phase particles propagate in a ductile manner at 900°C with holes opening in front of the crack between particles. The particles themselves deform by shearing crystallographically.

d. A high density of helium bubbles along the grain boundary precipitate/matrix interface does not necessarily lead to brittle intergranular fracture at 900°C.

e. Room temperature tension tests showed transgranular cracks propagated while a parallel, previously existing intergranular crack containing necked down precipitates did not propagate.

VI. REFERENCES

1. P. Duhaj and J. Ivan, J. Iron Steel Inst., 206, (1968), p. 1014.
2. F. R. Beckitt & B. R. Clark, Acta Mct., 15, (1967), p. 113.
3. M. H. Lewis and B. Hattersley, Acta Mct., 13, (1965), p. 159.
4. M. ti. Lewis, Acta Mct., 14, (1966), p. 142.
5. S. Nenno, et al., Trans. Jap. Inst. Metals, 3, (1962), p. 82.
6. ASTM card no. 14-1407 ($M_{23}C_6$).
7. ASTM card no. 14-330 (M_6C).
8. ASTM card no. 15-539 (σ phase).
9. ASTM card no. 6-674 (χ phase).
10. B. Weiss and R. Stickler, Met. Trans., 3, (1972), p. 851.
11. G. Cliff and G. W. Lorimer, J. of Microscopy 103, pt. 2 (1975), P. 203.
12. D. V. Edmonds and R. W. K. tioneycombe, "Precipitation in Iron-Base Alloys" in Precipitation Processes in Solids, edited by K. C. Russell & ti. I. Aaronson (The Metallurgical Society *of* AIME, Warrenton, PA) 1978, p. 121.
13. D. N. Braski, H. Shroeder, S ti. Ullmaier, J of N. Materials, 83, (1979), p. 265.
14. J. A. Horton, Doctoral Dissertation, U.Va., Jan. 1980.
15. D. S. Gelles, 109th Annual Meeting of AIME, Las Vegas, 1980.
16. I. Chan, Doctoral Dissertation, U.Va., Jan. 1980.
17. J. C. Williams, R. R. Boyer, M. J. Blackburn, ASTM STP 453, (1969), P. 215.
18. R. W. Bauer, R. L. Lyles, ti. G. F. Wilsdorf, Z. Metallkde, 63, (1972), P. 525.

19. H. C. Burghard, Met. Trans., 5, (1974), p. 2083.

20. A. Gysler, G. Lütjering, V. Gerdd, Acta Met, 22, (1974), p. 901.

21. R. N. Gardner, T. C. Pollock, H. G. F. Wilsdorf, Mat. Science Eng., 29, (1977), p. 169.

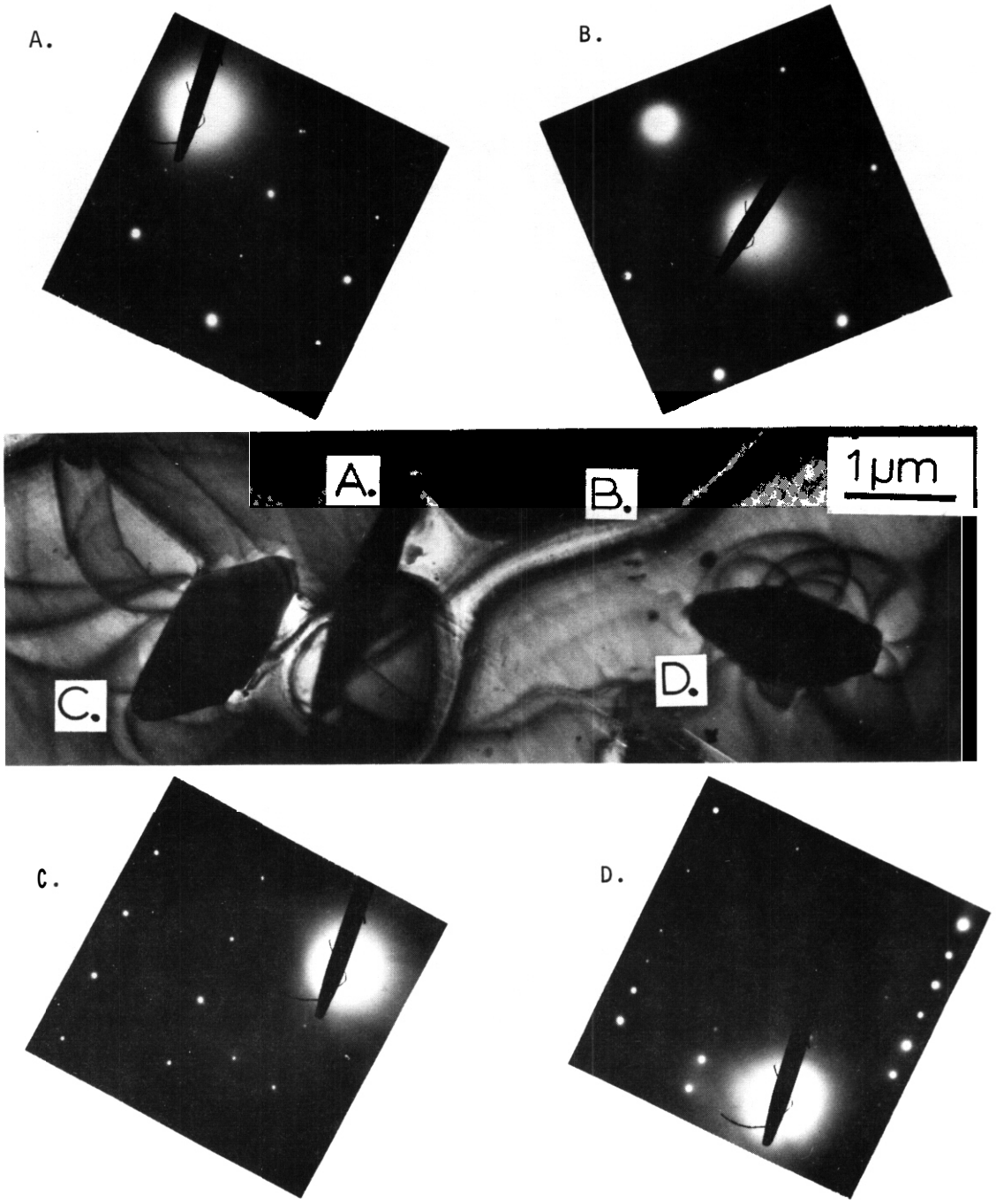

FIGURE 1: Micrograph of rod-shaped and irregular precipitates. SAD patterns A, C, and D correspond to precipitates labeled A, C, and D while Pattern B corresponds to the matrix.

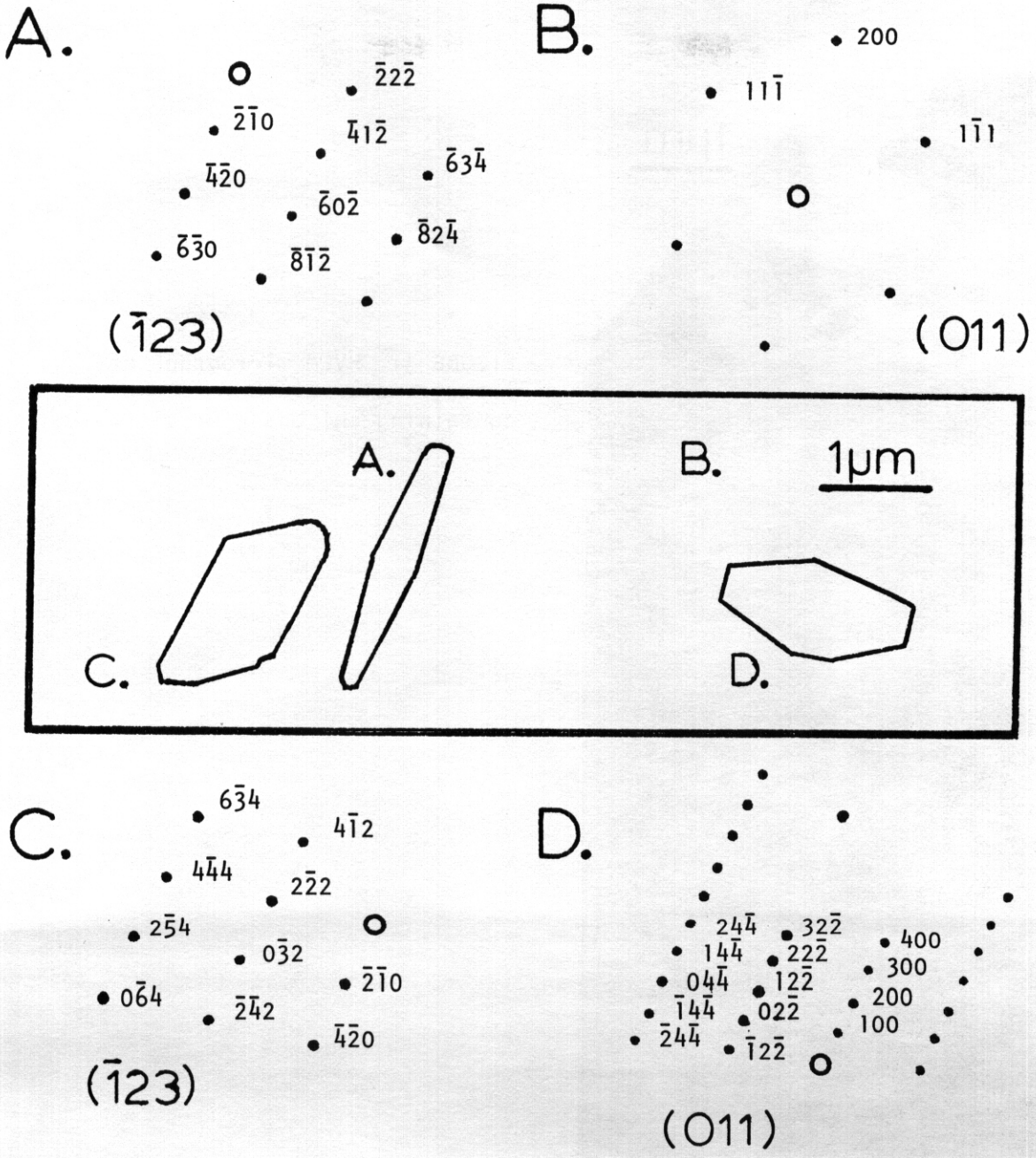

FIGURE 2: Indices of SAD patterns in figure 1. (Note: the electron beam direction is different for each pattern.)

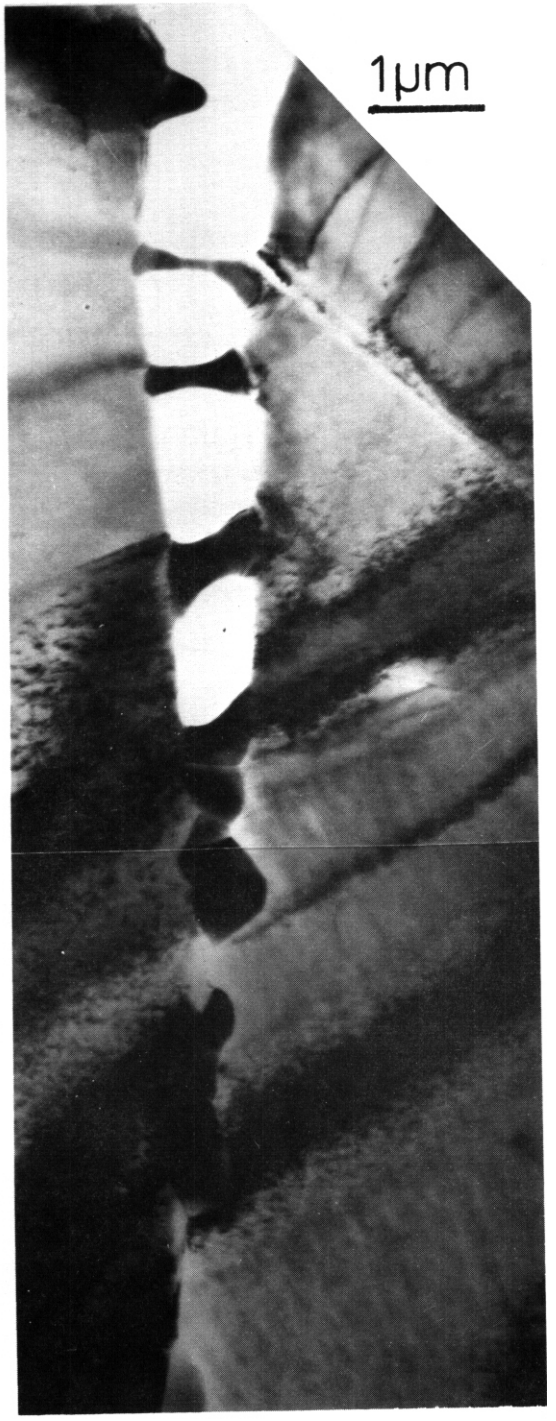

FIGURE 3: HVEM micrograph of intergranular crack formed at 900°C containing chi phase precipitates.

CHAPTER 4

CORRELATION METHODOLOGY

I. PROGRAM

Title: Effects of Irradiation on Fusion Reactor Materials
Principal Investigators: F. V. Nolfi, Jr. and A. P. L. Turner
Affiliation: Argonne National Laboratory

II. OBJECTIVE

The objective of this work is to determine the microstructural evolution, during irradiation, of first-wall materials with special emphasis on the effects of helium production, displacement damage and rates, and temperature.

III. RELEVANT OAFS PROGRAM PLAN TASK/SUBTASK

SUBTASK II.C.2.1 Mobility, Distribution, and Bubble Nucleation

IV. SUMMARY

Work on the temperature dependence of void swelling in preinjected single-ion and dual-ion irradiated 316 stainless steel has been updated by re-analysis of some samples and addition of new samples. The purpose was to rationalize the somewhat anomolous data which was reported previously.[1] Re-analysis of samples which caused large anomolous peaks in the single and dual-ion swelling curves showed that an artifact was present; its removal reduced the calculated peak swelling. Swelling data for the newly added samples was in good agreement with previous results. The final swelling curve shows a broad peak for dual-ion irradiated samples, and a smaller narrower peak for preinjected samples.

V. ACCOMPLISHMENTS AND STATUS

A. Temperature Dependence of Swelling in Single and Dual-Ion Irradiated 316 Stainless Steel -- G. Ayrault, H. A. Hoff and R. A. Conner, Jr.

1. Introduction

A major question in the irradiation response of candidate fusion reactor structural materials is the influence of concurrent displacement damage and helium production. Dual-ion irradiation, using heavy-ions for damage production and helium ions to simulate gas production by transmutation events, provides a means of investigating such effects in the absence of a high energy neutron source.

This report is an update of the preliminary results presented in an earlier progress report[1] on the temperature dependence of swelling in single and dual-ion irradiated 316 stainless steel. Since the previous report, five samples (two dual-ion and three single-ion) have been added, and two samples (one dual-ion and one single-ion) were completely re-analyzed to eliminate artifact effects. It will be seen that the new samples largely confirmed the previous results, while the re-analyses produced rather dramatic changes in the swelling curves.

2. Irradiation Conditions

Type 316 stainless steel samples from the MFE heat were 50% cold worked, then solution annealed at 1050°C for 0.5 h and aged at 800°C for 10 h. One set of samples was simultaneously irradiated with 3.0 MeV Ni^+ and 0.87 MeV degraded $^3He^+$ in the ANL Dual-Ion Irradiation Facility; the nominal helium injection rate was 15:1 appm He:dpa. A second set of samples was preinjected at room temperature with either 5 or 15 appm ^3He and single-ion irradiated with 3.0 MeV Ni^+. For both sets the nominal dose was 12 dpa. For dual-ion and 5 appm preinjected single-ion samples the nominal irradiation temperatures were 550, 600, 625, 650 and 700°C. For the 15 appm preinjected samples the nominal temperatures were 575 and 675°C. Surface temperatures of all samples were measured with an infrared pyrometer during irradiation.

After irradiation the samples were electrochemically sectioned to 4500 Å (peak damage is at 5500 Å), and backthinned for TEM inspection.

3. Swelling in Dual-Ion Irradiated Samples

The lack of a smooth variation in void swelling as a function of temperature in the previously reported preliminary results,[1] prompted us to take a second look at the samples which had already been analyzed, and to add some nominal duplicate samples to see if the previous results were reproducible.

Calculated swelling values for the new samples at 638 and 652°C were in excellent agreement with the previous values at 633 and 649°C respectively, Fig. 1. As with previous samples the scatter between different regions of the same sample, represented by the error bars, was fairly large. Despite the good agreement in swelling between old and new samples, we have doubts about the authenticity of the swelling difference between ∿ 635 and ∿ 650°C. This is because the agreement in swelling arose through compensating changes in cavity size and number density, as seen in Figs. 2 and 3. We have therefore drawn a smooth swelling curve between these points in Fig. 1.

For the small cavities in the bimodal cavity-size distribution, the measured number densities were larger and mean cavity diameters smaller in the new samples. The cause of this was traced to greater care in recording the new micrographs, making small cavities more easily visible. This is a graphic illustration of the danger in using overall mean values for cavity size and number density when very small cavities are present. The changes in overall mean values produced here by small changes in image quality would be large, and devoid of any physical significance. Information about the large cavities, which actually produce the swelling, would have been lost if the small and large components had not been separated.

A rather dramatic change in the swelling curve resulted from re-analysis of the sample irradiated at 603°C. Our initial analysis indicated a large swelling (~ 3.5%) for this sample due to the large cavities of irregular shape shown in Figs. 4a and b. On first inspection of single micrographs these appeared to be surface artifacts, but stereo inspection showed that most were within the foil. In addition one could image a surface coating in dark-field, Fig. 4b, which appeared to be similar to that on the smaller, nearly spherical cavities. This led us to conclude that the large cavities actually formed with these irregular shapes, and had the same coating as the smaller cavities. However, more recent observations indicated that this was not the case. In thick regions of the foil it was found that the large cavities were all nearer to the backthinned surface than the sectioned surface (different solutions were used for sectioning and backthinning). In addition, careful inspection of some of the cavities in some stereo pairs showed hollow tracks leading to the backthinned surface; there tracks appeared to be in the same directions as the axes of the acicular precipitates(2).

Thus it appears that the large, irregularly shaped cavities are artifacts, probably caused by preferential etching of the acicular precipitates; on encountering genuine cavities which had nucleated at the ends of the precipitates, it is thought that these etched out to form the bulbous shapes deep in the sample which were observed. This model is somewhat speculative, but the fact that the cavities (or at least their large sizes) are artifacts is clear from their appearance near only one surface. For this reason the micrographs were re-analyzed, eliminating the large, irregular cavities. The re-analyzed swelling value for this sample (plotted at 603°C) is lower than that of its nominal duplicate at 595°C, and may now be under-estimated since the large cavities eliminated in the analysis probably started as normal size cavities before being etched out. The computer program used for swelling analysis includes a correction for cavities which intersect the surface and are etched out (they are deliberately

not counted with the Zeiss particle sizer, and the program compensates by increasing the number density), but these cavities are far too deep within the sample for this correction to be adequate. For this reason we have given little weight to this point when drawing the swelling curve of Fig. 1.

4. Swelling in Single-Ion Irradiated Samples

Three helium preinjected and single-ion irradiated samples have been added since the last progress report, two preinjected with 15 appm ^{3}He and irradiated at ∿ 575 and 675°C, and one preinjected with 5 appm ^{3}He (like the other samples in this study) and irradiated at 642°C. In addition the 645°C nominal duplicate of the last-mentioned sample was re-analyzed in the same way as the 603°C dual-ion sample described above.

In the past report'') an anomolous swelling peak at ∿ 650°C was reported for the sample shown in Fig. 4c and d. Re-analysis showed that although the cavities were within the sample, they were all closer to the backthinned surface than the sectioned surface, and are thought to be etching artifacts like those described above in the 603°C dual-ion sample. Since no cavities were found close to the sectioned surface, we have taken the swelling to be zero for this sample. This conclusion was supported by the nominal duplicate sample at 642°C, in which no cavities and no etching artifacts were observed. The reason for finding artifacts in some samples but not in others is not clear at present.

The swelling curves of Fig. 1 show that room temperature preinjection of 5 appm ^{3}He has suppressed void swelling relative to dual-ion irradiations, at this dose level. The new point with 15 appm 3He and 575°C suggests even greater supression for higher helium content. Figures 2 and 3 show that this further suppression is the result of a similar number density of smaller cavities. The second 15 appm ^{3}He preinjection at ∿ 675°C supports the trend of complete suppression of swelling at 12 dpa for T > 625°C. It should be noted that this suppression

is at least partially due to a delay in the onset of the rapid swelling regime for preinjected samples, as shown by dose dependence studies (up to 25 dpa) in both 316 stainless steel[**] and Fe-20Ni-15Cr.[3] Further experiments are needed to determine whether or not swelling suppression in preinjected samples persists at high (> 25 dpa) doses.

VI. References

1. F. V. Nolfi, Jr., G. Ayrault and H. A. Hoff, DAFS Quarterly Report No. 7, July-September (1979).

2. F. V. Nolfi, Jr., A. P. L. Turner, G. Ayrault and H. A. Hoff, DAFS Quarterly Report No. 9, January-March (1979).

3. S. C. Agarwal, G. Ayrault, D. I. Potter, A. Taylor and F. V. Nolfi, Jr., J. Nucl. Mater. 85 & 86, p. 653 (1979).

VII. Future Work

Quantitative TEM analysis of dose dependence studies on samples dual-ion irradiated at 5:1 and 50:1 appm He:dpa and 625°C is essentially complete, and final data reduction *is in* progress. Further dual-ion irradiations of 316 stainless steel involving different dose rates, higher doses, and variations in the helium injection schedule will be carried out in the near future.

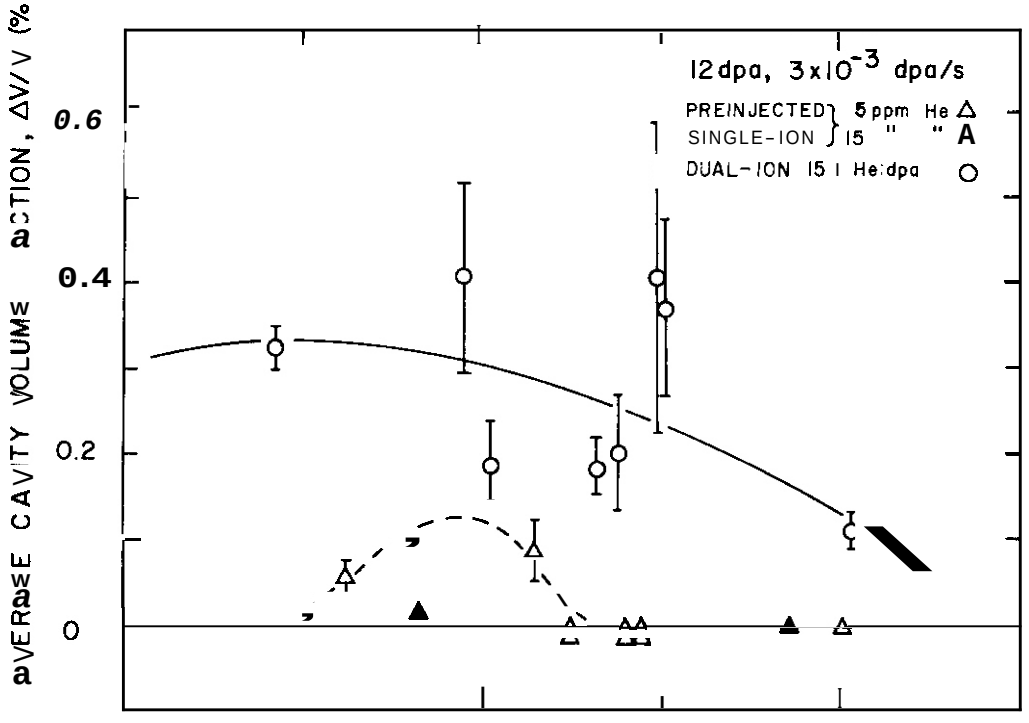

Figure 1. Temperature dependence of swelling in dual-ion and preinjected single-ion irradiated 316 stainless steel.

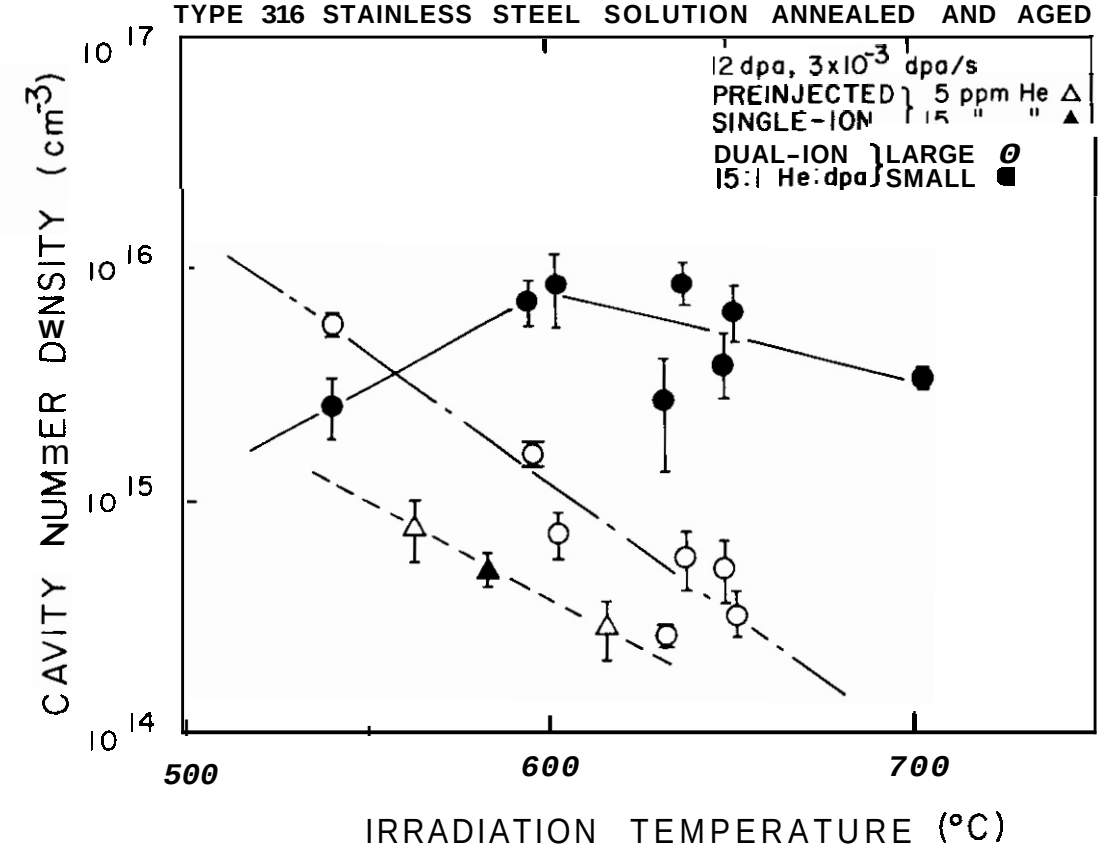

Figure 2. Temperature dependence of cavity number density in dual-ion and preinjected single-ion irradiated 316 stainless steel.

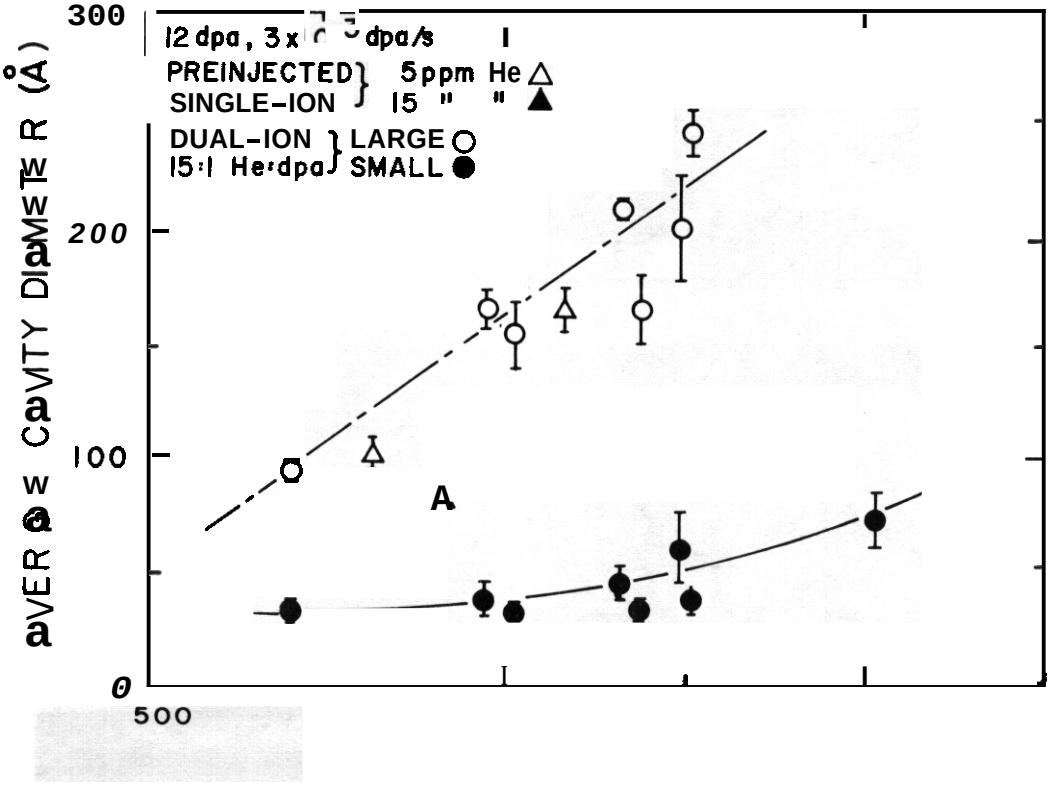

Figure 3. **Temperature dependence of mean cavity size in dual-ion and preinjected single-ion irradiated 316 stainless steel. Small and large cavity sizes are plotted separately for the bimodal size distribution found in dual-ion irradiated samples.**

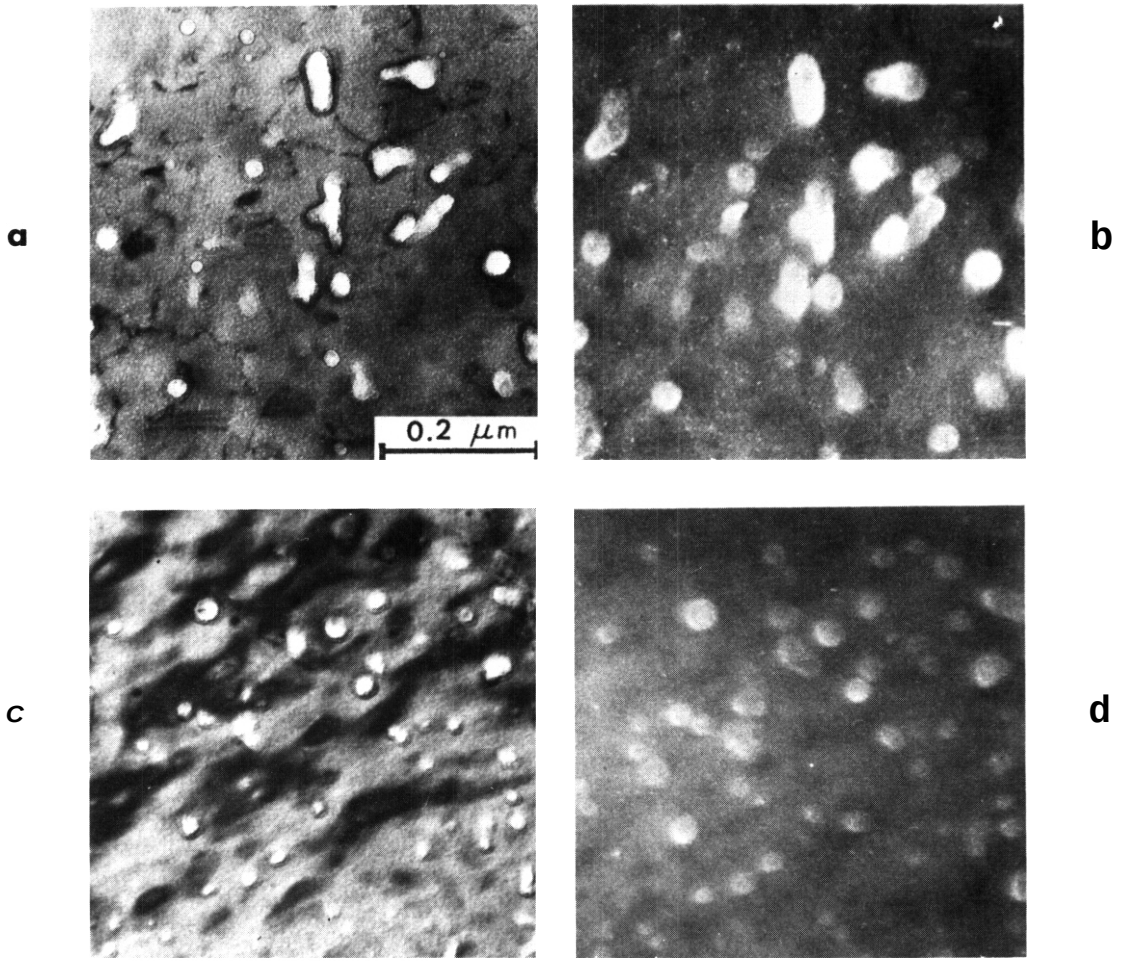

Figure 4. Bright-field dark-field pairs showing irregularly shaped cavities in preinjected single-ion and dual-ion irradiated 316 stainless steel (dose = 12 dpa, dose rate = 3×10^{-3} dpa $\cdot$ s^{-1}) (a) 603°C dual-ion, (b) dark-field of same region as (a), (c) 645°C preinjected single-ion, and (d) dark-field of same region as (c).

I. PROGRAM

Title: Irradiation Response of Materials

Principal Investigators: J. A. Spitznagel, S. Wood, and W. J. Choyke
Affiliation: Westinghouse Research and Development Center

II. OBJECTIVE

The objective of this work is to assess the phenomenology and mechanisms of microstructural evolution in materials exposed to simultaneous helium injection and creation of atomic displacement damage by a second ion beam.

III. RELEVANT DAFS PROGRAM TASK/SUBTASK

SUBTASK II.C.1, II.C.2, II.C.3, II.C.5, II.C.9, II.C.18

IV. SUMMARY

Microstructural evaluation of dual-ion bombarded titanium-modified 316 SS at appm He/dpa ratios of 0.2, 12 and 70 reveals precipitation of MC particles in cube-on-cube orientation with the matrix. Small He bubbles are seen in association with the particles in reasonable agreement with observations on the same material after HFIR irradiation. A first order attempt at partitioning implanted helium between cavities and dislocations results in reduced critical cavity sizes and lower temperature sensitivity for the transition from gas-driven to bias-driven cavity growth. A method is proposed for correcting cavity volume fractions and swelling for statistically combined cavity distributions obtained at widely different magnifications, foil thicknesses and cavity sizes.

V. ACCOMPLISHMENTS AND STATUS

A. Microstructural Evaluation of Dually-Bombarded Ti-Modified 316 SS

Helium produced by (n,α) reactions from 14 MeV neutrons in the plasma will inevitably induce swelling or other deleterious effects in all candidate first-wall materials for CTR applications. Thus, swelling reduction and mechanisms of helium trapping are important and interesting factors to be pursued. Maziasz and Bloom have recently shown[1] that titanium additions to a standard type 316 SS resulted in a dramatic reduction in swelling (at $T \lesssim 700°C$ for specimens irradiated in HFIR to fluences producing 3000 to 4200 appm He and 40 to 60 dpa) when compared with the unmodified 316 SS. We have recently obtained data from dual ion-bombarded samples of the same Ti-modified steel and have observed a similar microstructural trend.

Bulk quantitative chemistry of the Ti-modified 316 SS has been reported previously.[1] Final fabrication steps prior to the dual bombardment with 28 MeV Si^{+6} and $\lesssim$ 2 MeV He ions at the High Energy Ion Bombardment Facility at the University of Pittsburgh were a solution anneal for 1h at 1050°C (in vacuum followed by an argon quench) following a 50% reduction in area of rod by cold swaging. The anneal was sufficient to induce some rather inhomogeneous precipitation of the Ti-rich carbide phase reported by Maziasz,[1] with an average size $\sim$ 40 nm and a number density $\sim 3 \times 10^{13}/cm^3$. Targets of this material were subsequently bombarded at 600°C to a peak of 40 dpa, and with appm He/dpa ratios of 70:1, 12:1 and 0.2:1, for comparison with HFIR, CTR and EBR-II conditions, respectively. Preliminary data obtained at a fluence of $\sim$ 3 dpa and a displacement rate of $\sim 1 \times 10^{-4}$ dpa/s are reported.

Typical BF TEM micrographs obtained with void-contrast conditions are shown in Fig. 1 for the 70:1 specimen ($\sim$ 2.8 dpa, 180 appm He). Figure 1a clearly shows a bimodal cavity distribution with a low number density

of ∼ 35 nm diameter cavities and a higher number density of bubbles which are ∼ 5 nm in diameter. Both are associated with Ti-rich carbides induced during bombardment, although only a fraction of these precipitates appear to have cavities adjacent to them. Further, higher magnification, high resolution TEM work is currently in progress to ascertain if the number density of the small bubbles is higher than indicated here. The precipitate stringers visible in Fig. 1a suggest that carbides have nucleated on dislocations [similar features have been observed by Maziasz[1]]. In general, bubbles associated with the stringers are larger and therefore more easily resolvable than those associated with most of the randomly nucleated precipitates. Comparison of Figs. 1a and 1b reflects the overall inhomogeneity observed in the cavity microstructure. It is suggested that the apparent absence of cavities in 1b is linked to a non-homogeneous precipitate distribution throughout the specimen. This second area shown in Fig. 1b has a higher carbide number density which may have resulted in a higher number density of smaller, and therefore unresolvable bubbles. A further, very important point to make is that the swelling in this material is drastically reduced compared to that obtained in conventional SA 316 SS under similar experimental conditions. Our earlier work has shown that at these helium injection and damage rates (6.9 x 10^{-3} appm/s and 1.1 x 10^{-4} dpa/s, respectively) SA 316 SS exhibits rapid cavity growth and thus a very high swelling.[2]

The precipitates are better imaged in the DF TEM micrograph shown in Fig. 2a, and clearly have a cube-on-cube crystallographic habit. This is in agreement with small MC particles produced thermally in titanium-modified austenitic stainless steels[3] but does not totally agree with observations made after HFIR irradiation to high fluences of 30-60 dpa.[4] In the latter material, an additional rod-shaped variant was observed. Further work is currently in progress on our dually bombarded specimen to ascertain if rod-shaped carbides are present at some low number density. It is possible that they may only be observed at the higher fluences.

Figure 2b shows a typical dislocation structure imaged under a two beam dynamical condition with g = [111]. It is generally similar to other low fluence structures obtained in 316 SS, exhibiting some faulted loops, but mostly line dislocations. The cube-on-cube carbides are also imaged under these diffraction conditions, and close inspection of the micrograph shows their characteristic Ashby-Brown strain contrast.[5]

Dislocation and cavity microstructures from the specimen irradiated to ∿ 3 dpa at 600°C with an appm He/dpa ratio of ∿ 12:1 are presented in Fig. 3. Stereo microscopy has shown that the cavity-like features in Fig. 3a are all close to one of the foil surfaces and thus are polishing artifacts. If these are ignored, it is apparent no large cavities have developed and, furthermore, no equilibrium gas bubbles are visible. Similarly, bubbles were not observed in the specimen bombarded to an appm He/dpa ratio of 0.2:1 (not shown). Further, higher magnification TEM is in progress to clarify this point and ascertain if very small ($\lesssim$ 30Å) bubbles are present. There is also no evidence of irradiation-induced carbide precipitation in either the 12:1 or 0.2:1 samples — comparison of Figs. 3b and 2b clearly indicates this. However, Fig. 3a does show a few carbides similar to those observed in unirradiated specimens. Dislocation structures are again characteristic of an unmodified 316 SS bombarded under similar experimental conditions. None of the specimens exhibited grain boundary precipitation or the development of Laves phase [such as that seen after HFIR irradiation to high fluences[4]].

These results suggest that the Ti-rich carbide nucleation and/or growth is linked to either the helium injection rate or total [He], since these were the only experimental variables (damage rate, fluence and temperature were maintained constant). It is possible that very small carbide clusters have formed but have not grown sufficiently to be imaged with the TEM. Despite their size, such clusters could still act as effective trapping sites for helium, resulting in a high number density of non-visible helium clusters.

B. Modification of the Helium Inventory Method to Account for Helium Trapping at Dislocations

The use of several inferential methods for determining the spatial distribution of implanted helium was described previously.[6] In particular the "helium inventory" method was found to be particularly useful for estimating the maximum equilibrium bubble size, the spatial distribution of bubbles, and the critical cavity size for the transition from gas-driven to bias-driven cavity growth. We presently have a first order correction to the method which attempts to account for the amount of helium partitioned to dislocations.

Dislocations are known to be very effective traps for helium. There are numerous examples in the literature suggesting that helium bubble nucleation and growth are very intimately tied to the dislocation structure. It has been postulated[7] that under continuous helium injection populations of growing bubbles, cavities and mobile and sessile dislocations compete for the injected helium. To a first approximation, the partitioning of helium to these sinks should be related to the sink strengths for point defects.[7,8]

If we define Q^{-1} as the fraction of helium partitioned to cavities such that

$$Q^{-1} = \frac{\sum_i 2\pi D_i N_i}{\sum_i 2\pi D_i N_i + \rho_D}$$

where D_i = diameter of cavity in size class i
N_i = number of cavities in size class i
ρ_D = dislocation density

Then the amount of helium to be distributed to the cavities is

$$[He]_c = K_g \cdot t \cdot Q^{-1}$$

K_g = gas injection rate (assumed constant)
t = time for implantation

neglecting helium still in solution in the matrix or lost to grain boundaries. The amount of helium partitioned to dislocations is then

$$[He]_d = K_g \cdot t[1 - Q^{-1}].$$

Figure 4 shows the variation of the fractional partitioning of He to dislocations with dislocation density, ρ_D, in dual ion bombarded 316 SS. The data points shown are for a variety of initial microstructural conditions including solution annealed, 20% cold rolled and aged (800°C) at bombardment temperatures $\geq$ 600°C. The values have been obtained by incorporating partitioning coefficients into our computerized data files. Data was selected from targets bombarded at similar damage rates (within a factor of 4) and fluences but with atomic displacement damage produced by different high energy ions (28 MeV Si^{+6} or 20 MeV O^{+4}) at appm He/dpa ratios from 13 to 85. Data from cavity-dominated microstructures such as those exhibiting the rapid cavity growth phenomenon[2] have been excluded. In this temperature region the helium partitioning is a monotonically increasing function of the dislocation density. Analysis of data at lower temperatures, still in progress, suggests a much more complicated dependence with higher sensitivity to the appm He/dpa ratio.

Approximately 40-100% of the helium is partitioned to the dislocations based on the relative sink strength approximation. This reduces the amount of helium available to stabilize equilibrium bubbles and should reduce the maximum equilibrium bubble size calculated from the helium inventory method. Figure 5 demonstrates the effect. The maximum

equilibrium bubble diameter, D_c, is smaller when $Q^{-1} \neq 1$. The effect is most pronounced at higher temperatures and suggests that the temperature dependence of the critical cavity size (related to the maximum equilibrium bubble size) may be less than that predicted by theory.[9]

Several assumptions in this partitioning scheme make it likely that too little helium is allocated to the cavities. First, it is assumed that absorption by a dislocation removes the possibility of the helium atom ever being absorbed by a cavity. This is intuitively unrealistic. Bubble nucleation is often seen to occur in association with dislocations so that one event can follow the other. In addition, no account is taken of thermal desorption, resolution from atomic displacements, "pipe" diffusion or dislocation "drag" effects — all of which would tend to enhance the probability of multiple trapping of He atoms by vacancies and small bubbles. The inventory is also conducted with a static picture, i.e. relative sink strengths at some damage level. In reality, Q^{-1} is a function of time or dpa level and tends to increase continuously so that $(1 - Q^{-1})$ tends to decrease as a saturation value of ρ_D is approached.

While it will be extremely difficult to derive more rigorously correct partitioning values, a number of experimental approaches can be taken Temperature change experiments, post-bombardment annealing and spatially inhomogeneous helium implants look particularly promising to us. In this regard we note that increasing the temperature during dual ion bombardment gives estimated critical cavity sizes more in accord with a value of $Q^{-1} = 1$.[6]

C. Corrections to Cavity Volume Fraction and Swelling for Statistically Combined Cavity Distributions with a Wide Range of Sizes

Procedures have been recommended by the ASTM[10] for obtaining bulk representative "void" densities from TEM micrographs. In general, it is assumed that void size distributions are randomly distributed and homogeneous in each size class. If voids whose centers lie within 0.5 D_i of

each foil surface are not counted, to avoid possible errors from erosion of cavity walls intersecting the surface during electropolishing, bulk representative cavity densities (ρ_v) may be obtained from

$$\rho_v = \frac{1}{A} \sum^{i} \frac{n_i}{\left(t_f - D_i\right)} = \frac{1}{A\, t_f} \sum^{i} N_i$$

where n_i = observed number of voids in size class i

N_i = number of voids corrected for surface intersections

$= n_i t_f/(t_f - D_i)$

A = area in which measurements are made

t_f = foil thickness

D_i = mean diameter of size class i

Problems arise when a large number of measurements are required from many areas of the foil at widely differing magnifications. This situation exists when helium levels and injection rates are high enough to produce large numbers of barely resolvable bubbles and fewer but much larger inhomogeneously distributed cavities. To obtain a reasonable statistical representation of such populations it is necessary to photograph many areas. Counting and sizing all cavities using stereo images to apply the $\geq 0.5\ D_i$ exclusion principle then becomes impractical. In addition, it is necessary to work in very thin areas of the foil to properly size and count the small bubbles. This can result in loss of information about the larger cavities usually responsible for most of the swelling. Combining data at low and high magnifications in thin areas of the foil greatly improves the counting statistics, but results in erroneous cavity area and volume fractions. Other statistical problems arise in attempting to characterize inhomogeneous cavity populations using only thick sections of foil and in combining data obtained at very different magnifications and thicknesses using different visibility criteria.[11] These will not be discussed further here.

To the best of our knowledge no quantitative stereological method or statistical procedure has been worked out to "correctly" handle such data sets. Failure to apply some corrections for truncation and erosion of cavity surfaces, however, has resulted in overestimates of void volume fractions in some of our data. While we believe that comparisons of ion and neutron results will be most fruitful if centered on relative nucleation and growth kinetics using model calculations, it is undoubtedly true that "swelling" values will be compared. Thus, we have attempted a first order correction of void volume fraction for projected images of convex particles. The approach used by Cahn and Nutting[12] as extended by Underwood[13] forms the basis for the correction needed for truncation of non-overlapping images by the foil surfaces. An exclusion size, based on observations of many stereo plates, is also invoked to minimize electropolishing effects on cavity size and shape.

If a correction factor F_T is defined such that:

$$F_T \times n_i = U_c \cdot A_A = \left[\frac{2 D_i}{2D_i + 3t_f}\right] A_A$$

where n_i = number of cavities in size class i
U_c = Underwood[13] correction factor to the specific projected area of the particles per unit test area, A_A
D_i = diameter of cavities in size class i
t_f = foil thickness

it can be shown[14] that

$$F_T = \frac{3t_f}{2D_i}\left[\frac{2D_i}{2D_i + 3t_f}\right]$$

Thus multiplying the number of cavities in each size class by F_T should give a void volume fraction corrected for truncation of cavities with centers either inside or outside of the foil volume imaged. Every feature thought to be an image of a cavity, regardless of proximity of the feature to the foil surface, can thus be counted and sized on the projected image. It is thus relatively simple to apply the correction to each data set in a comouterized data file.

Figure 6 shows the variation of F_T with the ratio of D_i/t_f. For small cavities, $D_i << t_f$ and very little correction is required. However, as $D_i/t_f \rightarrow 1$, it is necessary to reduce the number of cavities contributing to the swelling by as much as 40%.

Observations of stereo plates suggest that cavities with diameters $D_i \geq 3/4\ t_f$ are most likely to suffer enlargement, loss of shape and loss of void contrast due to electropolishing. Even for a cavity with $D_i = 3/4\ t_f$, however, the probability that it will not intersect the surface is $\sim$ 30%. Thus, to avoid an unrealistically large reduction in cavity volume fraction we have found it necessary to set the numerical exclusion at cavity sizes of $D_i \geq t_f$ and to apply the correction factor, F_T, to smaller size classes. This procedure is not rigorously correct. Small cavities are usually etched out instead of truncated. Large cavities which intersect the surface are truncated, but then enlarge at an unknown rate. Nevertheless, the procedure should give reasonable "lower bound" swelling values and will be used until an improved method is developed. By way of example, swelling values of 3.81% and 0.28%, reported for dual-ion bombarded aged 316 SS in the previous report,[6] reduce to 2.54% and 0.25%, respectively, with the correction procedure.

VI. REFERENCES

1. P. J. Maziasz and E. E. Bloom, ADIP Quarterly Report, DoE/ET/0058/1, August 1978.

2. Susan Wood, J. A. Spitznagel and W. J. Choyke, DAFS Quarterly Report #8, February 1980.

3. J. M. Leitnaker and J. Bentley, Met. Trans. 8A (1977) 1605.

4. P. J. Maziasz, unpublished work.

5. J. W. Edington, Practical Electron Microscopy in Materials Science (Van Nostrand Reinhold, 1976) p. 214.

6. Susan Wood, J. A. Spitznagel and W. J. Choyke, DAFS Quarterly Report #9, January-March 1980.

7. M. R. Hayns, AERE Report TP.758, Harwell U.K., October (1978).

8. M. R. Hayns and L. K. Mansur, Proceedings of the 10th ASTM International Symposium on Effects of Radiation on Materials, June 1980, Savannah, Georgia, to be published.

9. M. R. Hayns and M. H. Wood, J. Nucl. Mater. 87 No. 1, p. 97 (1979)

10. ASTM Proposed New Standard Recommended Practice for Neutron Radiation Damage Simulation by Charged Particle Irradiation Part II Postirradiation Examination (1975).

11. Susan Wood, G. Jouris and J. A. Spitznagel, Westinghouse Research and Development Center, unpublished work (1980).

12. J. W. Cahn and J. Nutting, Trans. AIME 215, p. 526 (1959).

13. E. E. Underwood, "Quantitative Stereology," Addison-Wesley Publishing Co., Reading, Massachusetts, p. 172 (1970).

14. J. A. Spitznagel, Westinghouse Research and Development Center, unpublished work (1980).

VII. FUTURE WORK

Further dual bombardment experiments on the Ti-modified 316 SS will be performed at 700°C and 550°C at appm He/dpa ratios of 70:1 and 12:1. Helium partitioning calculations will be extended to lower temperatures

and damage rates. It will be demonstrated that a scaling procedure exists for predicting instantaneous versus average helium injection rate effects on microstructure.

VIII. PUBLICATIONS

Susan Wood, et al., Scripta Metallurgica, 14 (1980), "Cavity Alignment and Precipitation in SA 316 SS During Dual Ion Bombardment."

TABLE 1

D_{hkl} OF PRECIPITATE VERSUS D_{hkl} OF PHASES NORMALLY FOUND IN 316 STAINLESS STEEL AGED AT 900°C

	D_{HKL} (Å)			
Experimental Data	[6] $Cr_{23}C_6$ ($M_{23}C_6$)	[7] Cr_3Ni_2SiC (M_6C)	[8] FeMo (σ phase)	[9] $Cr_{12}Fe_{36}Mo_{10}$ (χ phase)
8.84± .08	---	---	9.23 (100)	8.88 (100)
6.35±.25	6.16 (111)	6.13 (111)	6.52 (110)	6.28 (110)
---	5.32 (200)	5.31 (200)	---	5.13 (111)
4.42± .04	---	---	4.61 (200) 4.25 (101)	4.44 (200)
4.04±.09	---	---	4.12 (210)	3.97 (210)
3.67±.01	3.76 (220)	3.77 (220)	3.87 (111)	3.62 (211)
3.13±.11	3.08 (222)	3.07 (222)	3.13 (211)	3.14 (220)
2.96± .04	---	---	2.91 (310)	2.96 (300, 221)
a_o=8.87±.08Å	a_o=10.638Å	a_o=10.62Å	a_o=9.218Å	a_o=8.89Å
bcc	fcc	fcc	c_o=4.813Å tetragonal	bcc

3. Crystal Chemical Composition

By use of an x-ray energy dispersive analyser, microchemical compositions of each type of precipitate were computed from relative x-ray intensities, by means of the method first developed by Cliff and Lorimer [11]. The results of the microanalyses are summarized in table 2, where thecanpositions of different shaped precipitates in the matrix and on grain boundaries are compared to both

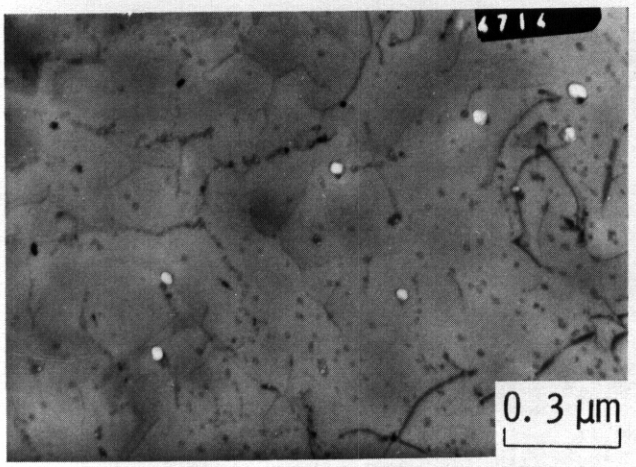

(a) Cavities Associated With Precipitates

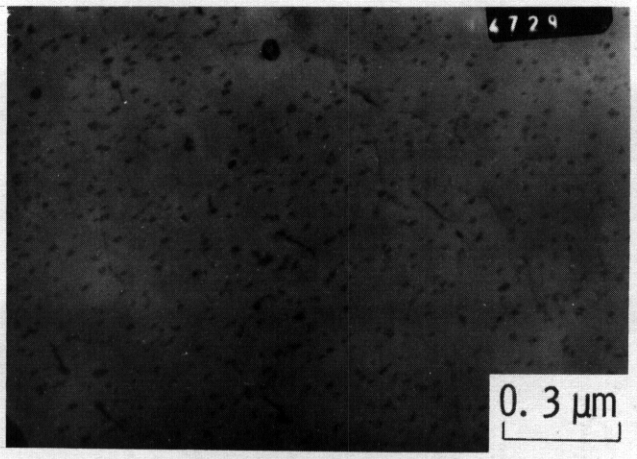

(b) Precipitates with no visible cavities

FIGURE 1. BF TEM Micrographs Showing Cavities and Precipitates in Dually Bombarded Ti-Modified 316 SS. (appm He/dpa ratio is 70:1).

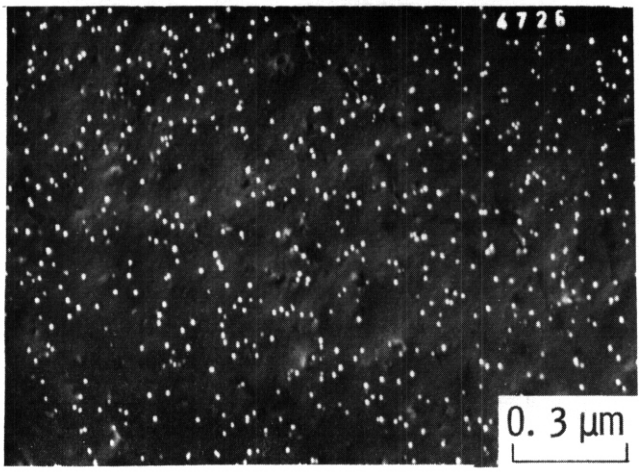

(a) DF of Cuboidal Carbides

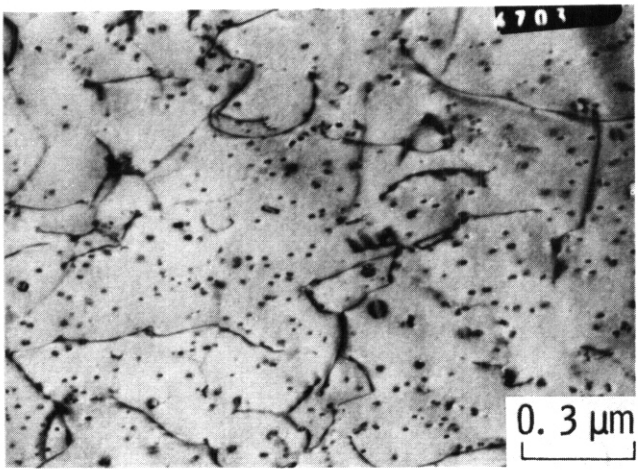

(b) Dislocation Structure.

$\vec{g} = [111]$ $\vec{z} \sim [112]$

FIGURE 2. TEM Microaraphs Showing (a) Precipitates and (b) Dislocation Microstructure in Dually Bombarded Ti-Modified 316 **SS** (appm He/dpa ratio is 70:1).

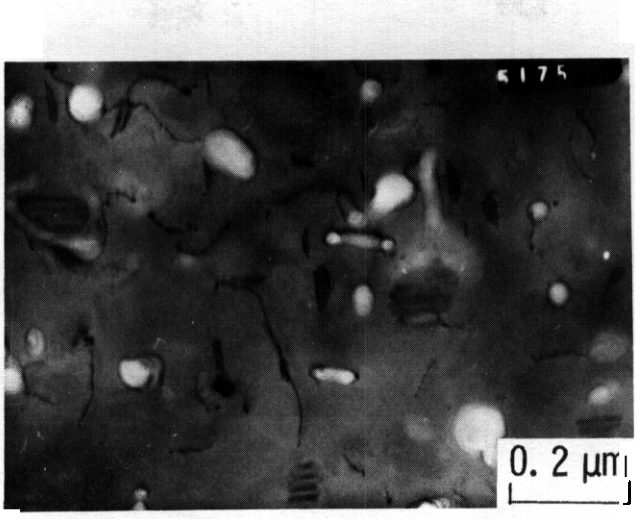

(a) Cavity Contrast

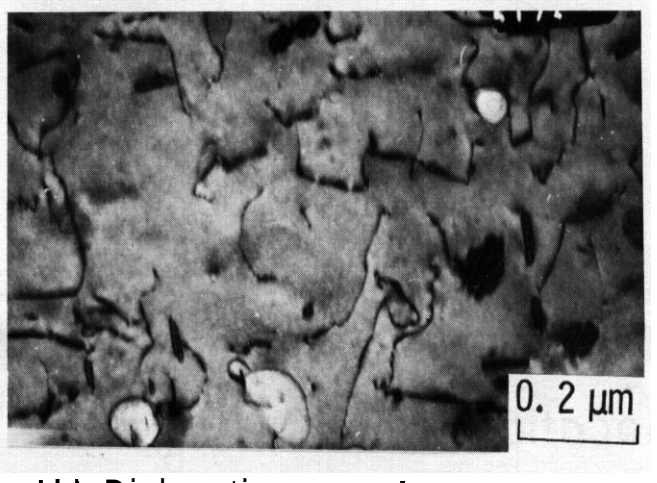

(b) Dislocation Structure

$\vec{g} = [111]$, $\vec{z} \sim [123]$

FIGURE 3. BF TEM Micrographs Showing Dislocations in Dual Ion-Bombarded Ti-Modified 316 SS (appm He/dpa ratio is 12:1). No cavities, bubbles or radiation-induced MC precipitation is observed. (Cavity-like features are polishing artifacts)

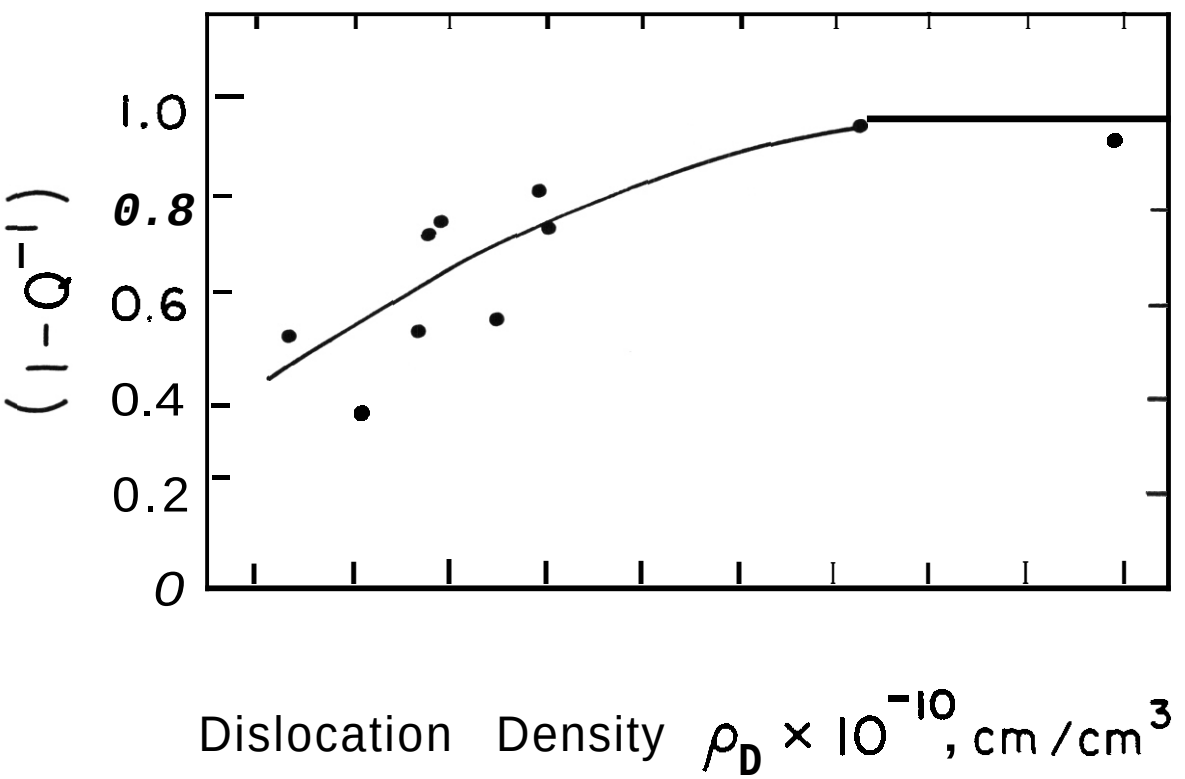

FIGURE 4. Fraction of Implanted Helium Atoms Partitioned to Dislocations ($1 - Q^{-1}$) as a Function of the Total Dislocation Density, ρ_D, for Dual-Ion Bombarded 316 SS in the Solution Annealed, 20% Cold-Rolled or Aged (800°C) Condition. 600°C $\leq T_{IRR} <$ 750°C; $\phi \sim$ 1.5-6.0 $\times 10^{-4}$ dpa/s; $\phi t \sim$ 3-12 dpa; appm He/dpa $\sim$ 12-85.

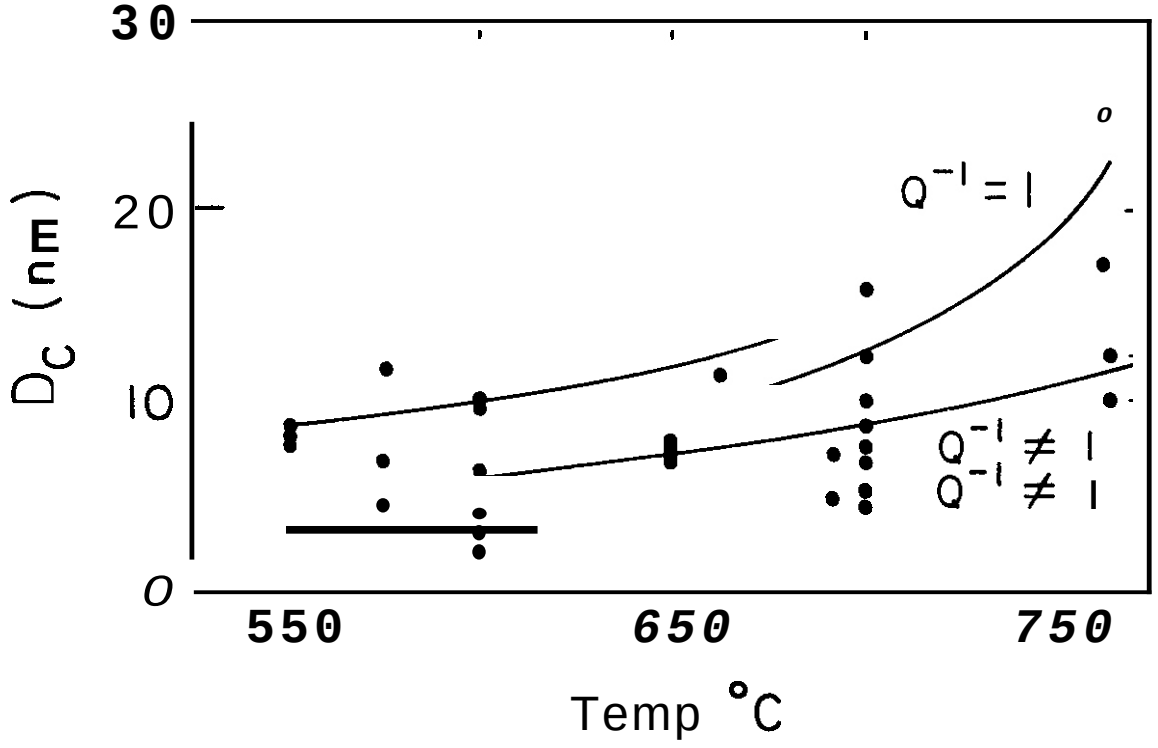

FIGURE 5. Comparison of Maximum Equilibrium Bubble Diameter D_C Determined from Helium Inventory Method for Dual-Ion Bombarded 316 SS Including Partitioning of Helium to Dislocations ($Q^{-1} \neq 1$) and Excluding Partitioning to Dislocations ($Q^{-1} = 1$). Material Conditions, Flux, Fluence and appm He:dpa Same as for Figure 4.

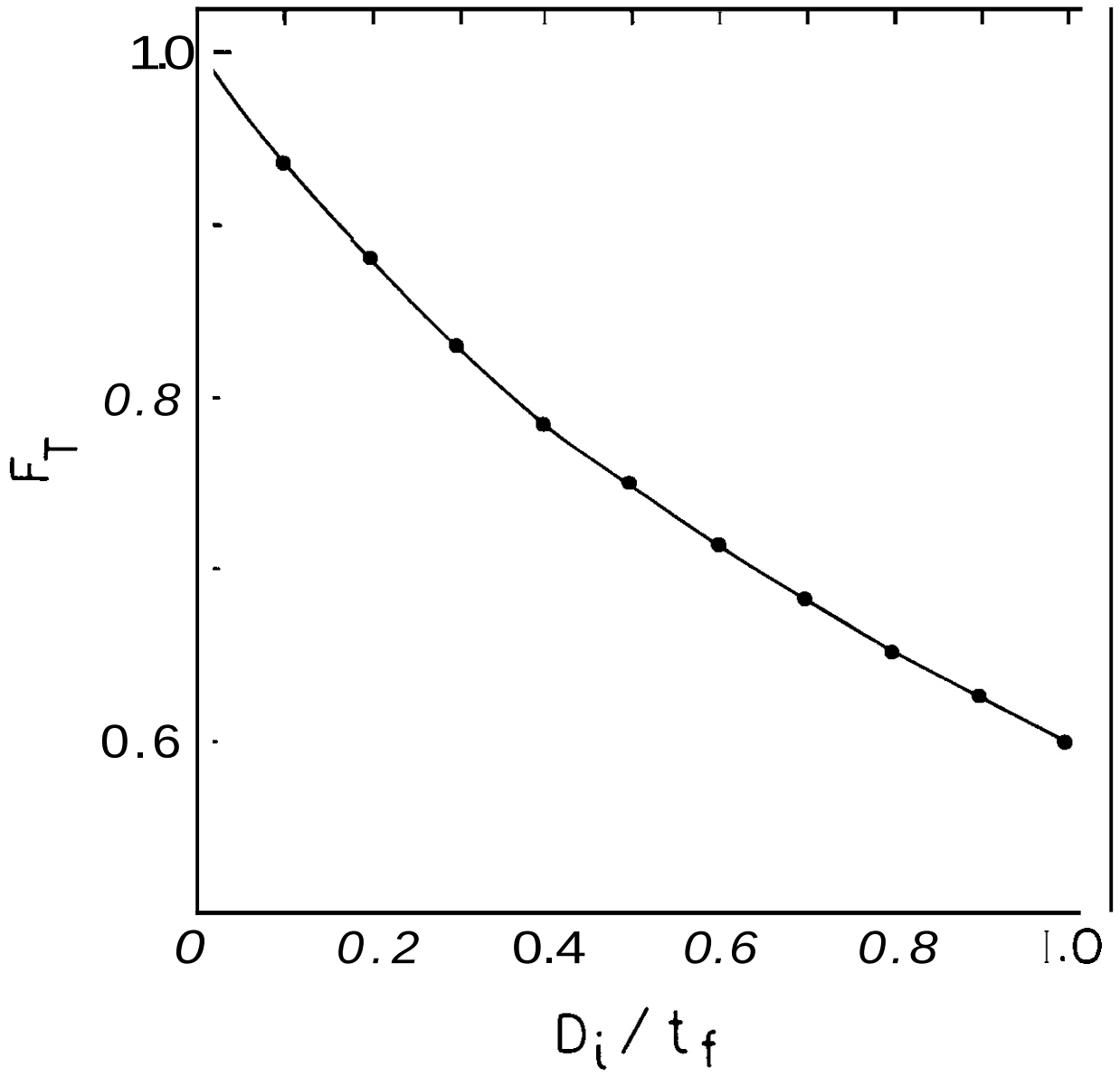

FIGURE 6. Calculated Correction Factor (F_T) for Cavity Number Density as a Function of the Ratio of Cavity Diameter to Foil Thickness.

I. PROGRAM

Title: Irradiation Effects Analysis
Principal Investigator: D. G. Doran
Affiliation: Hanford Engineering Development Laboratory

II. OBJECTIVE

The objective of this work is to study the irradiation response in a fast neutron environment of several ferritic and austenitic alloys

III. RELEVANT DAFS PROGRAM PLAN TASK/SUBTASK

Task II.C.l Effects of Material Parameters on Microstructure
Task II.C.17 Microstructural Characterization

IV. SUMMARY

The AD-2 experiment will begin irradiation in the EBR-II reactor in August 1980. Specimens provided by the DAFS program were included in the experiment. The specimens are transmission electron microscopy (TEM) disks of several ferritic alloys including two pressure vessel steels and several iron-nickel-chromium alloys. These specimens are being irradiated in EBR-II to study their response to neutron irradiation in a fast neutron environment.

V. ACCOMPLISHMENTS AND STATUS

A. DAFS Specimen Matrix io the AD-2 Irradiation Experiment - D. T. Peterson (HEDL) and G. R. Odette (UC-Santa Barbara)

1. Introduction

The second fusion program irradiation in the EBR-II reactor, designated AD-2, will begin irradiation in August 1980. The experiment is

divided into two parts, each consisting of three B-7c capsules. Part 1 consists of capsules B-317, B-318 and B-319 which are designed for isothermal irradiation at 390, 500 and 550°C, respectively. Part 2 consists of capsules B-320, B-321 and B-322, which are designed for isothermal irradiation at 390, 450 and 500°C, respectively. The experiment will be discharged for interim examination at a nominal fluence of 3.5 x 10^{22} n/cm^2 (E >0.1 MeV). The final discharge of the experiment will occur at a fluence of 7.0 x 10^{22} n/cm^2 (E >0.1 MeV).

2. Specimen Matrix

The specimens included in the test are listed in Tables 1 and 2. The specimens are TEM disks and for the most part are present in a multiplicity of seven to eight. A complete set of specimens was included for each discharge of the test. Extensive microhardness testing is planned for comparison with available mechanical properties data and the results of microstructural examinations. Limited hot hardness and instrumented microhardness testing is also planned.

The first two alloys in Table 1 are boron doped AISI 316 specimens prepared by MIT [1] and included at the request of O. Harling. These specimens are intended to test the feasibility of simulating fusion reactor helium effects during fission reactor irradiations by using a technique of boron doping followed by rapid solidification to produce a uniform distribution of boride precipitates. During irradiation these precipitates generate a uniform production of helium by the $^{10}B(n,\alpha)$ reaction.

Two heats of AISI 316 were included in both parts of the test. The N-lot heat (87210) was included as a control because of the extensive data base already available on this material. The MFE heat (X-15893) was included since it is the reference heat of 316 for the fusion program.

Steels A508 (Class 3) and A533-B (Class 1) are low alloy steels commonly used as LWR pressure vessel materials. A508 is a Belgian forging steel and A533-B is a plate steel. The LWR program has generated extensive data on the irradiation of these materials at temperatures up to about 400°C and to fluenceson the order of 10^{20} n/cm^2 (E >1.0 MeV).

TABLE 1

OAFS MATRIX IN PART 1 OF THE AD-2 TEST (390, 500, 550°C)

Alloy	Thermomechanical Treatment
AISI 316 + 1000 appm ^{10}B + Zr	850°C/1 hr/WQ
AISI 316 + 5000 appm B + Zr	980°C/0.5 hr/AC
AISI 316 (N-lot)	1050°C/2 min/AC + 20% CW
AISI 316 (MFE heat)	1050°C/2 min/AC + 20% CW
A508	As received
A533-B	As received*
B2	1025°C/5 min/AC + 800°C/8 hr/AC
63	1025°C/5 min/AC + 750°C/8 hr/AC
B4	1025°C/5 min/AC + 850°C/3 hr/AC + 720°C/8 hr/FC to 620°C/18 hr total/AC

* See Reference 7.

TABLE 2

OAFS MATRIX IN PART 2 OF THE AD-2 TEST (390, 450, 500°C)

Alloy	Thermomechanical Treatment
HT-9	1038°C/5 min/AC + 760°C/0.5 hr/AC
HT-9	1038°C/0.5 hr/AC + 760°C/2.5 hr/AC
9Cr-1Mo	1038°C/1 hr/AC + 760°C/1 hr/AC
2 1/4Cr-1Mo	900°C/0.5 hr/AC + 700°C/1 hr/AC
D57-B	1025°C/5 min/AC + 25% CW
10Cr-2Mo-V-Nb	1050°C/0.5 hr/AC + 800°C/1 hr/AC
AISI 316 (N-lot)	1050°C/2 min/AC + 20% CW
AISI 316 (MFE heat)	1050°C/2 min/AC + 20% CW

Alloys B2, B3 and B4 are developmental precipitation strengthened iron-nickel-chromium alloys. They were included to study phase stability during irradiation in a low helium environment. The results of this irradiation will be compared with the irradiation of similar specimens in the HFIR and ORR reactors.[2,3]

The first four alloy conditions in Table 2 are the same as those being tested in the Alloy Development for Irradiation Performance (ADIP) portion of this experiment, which includes tensile, crack growth, charpy, fatigue, fracture toughness and TEM specimens.[4,5] The mechanical properties data generated by the ADIP program will provide a baseline for the evaluation of the microhardness measurements on the TEM specimens.

These alloys together with D57-B and 10Cr-2Mo-V-Nb represent four generic classes of ferritic alloys. Alloys HT-9 and 9Cr-1Mo are martensitic alloys. HT-9 is a commercial 12% Cr-Mo-V-W alloy. The 9Cr-1Mo alloy is a developmental modification of the commercial 9Cr-1Mo alloy. Both alloys are being tested in the quenched and tempered condition which produces a microstructure consisting of tempered martensite. Alloy 2 1/4Cr-1Mo is a commercial bainitic alloy. It is being tested in the normalized and tempered condition. In this condition its microstructure consists of a combination of tempered bainite and ferrite. Alloy D57-B is a developmental delta-ferritic alloy. The 10Cr-2Mo-V-Nb alloy is a commercial duplex martensitiddelta-ferritic alloy, containing on the order of 30% delta-ferrite.[6]

VI. REFERENCES

1. L. Arnberg and O. Harling, "Characterization of Rapidly Solidified Boron Doped Stainless Steel for Synergistic Helium Production," DAFS Quarterly Report, DOE/ER-0046/1, January-March 1980.

2. D. T. Peterson and R. W. Powell, "HFIR Irradiation of Representative Path B Alloys," this report.

3. D. T. Peterson and R. W. Powell, "DAFS Specimen Matrix for the ORR MFE-IV Test," DAFS Quarterly Report, DOE/ER-0046/1, January-March 1980.

4. R. J. Puigh and B. A. Chin, "Test Plan for the Investigation of Irradiation Effects Upon Mechanical Properties of Ferritic Alloy," ADIP Quarterly Report, DOE/ET-0045/1, October-December 1979.

5. R. J. Puigh, N. F. Panayotou and B. A. Chin, "Specimen Preparation and Loading for the AD-2 Ferritics Experiment," AOIP Quarterly Report, DOE/ET-0045/3, April-June 1980.

6. T. Fujita, K. Asakura and T. Sato, "Development and Properties of New 10Cr-2Mo-V-Nb Heat Resisting Steel," Trans. I.S.I.J., 19, (1975) 605.

7. J. M. Steichen and J. A. Williams, "Effect of Strain Rate and Temperature on the Tensile Properties of Irradiated ASTM A533-B Steel," J. Nucl. Mat., 57, (1975) 303.

VII. FUTURE WORK

The AO-2 experiment will begin irradiation in August 1980. The test is scheduled to be discharged for interim examination at 3.5 x 10^{22} n/cm^2 (E >0.1 MeV) in June 1981.

I. PROGRAM

Title: Irradiation Effects Analysis

Prinicpal Investigator: D. G. Ooran

Affiliation: Hanford Engineering Development Laboratory

II. OBJECTIVE

The objective of this work is to study the stability and helium trapping characteristics of different precipitate phases in precipitation strengthened iron-nickel-chromium alloys.

III. RELEVANT DAFS PROGRAM TASK/SUBTASK

TASK II.C.1.1 Effects of Material Parameters on Microstructures

TASK II.C.2.2 Effects of Helium on Microstructures

IV. SUMMARY

Specimens provided by the OAFS program have been included in the High Flux isotope Reactor (HFIR) irradiations designated HFIR-CTR-30, 31, and 32. The specimens are transmission electron microscopy (TEM) disks of the Alloy Development for Irradiation Performance (AOIP) path B alloys B1, B2, B3, and E4.

V. ACCOMPLISHMENTS AND STATUS

A. HFIR Irradiation of Representative Path B Alloys - D. T. Peterson and R. W. Powell (HEOL)

1. Introduction

Three irradiation assemblies, designated HFIR-CTR-30, 31, and 32 are scheduled to begin irradiation in HFIR in July 1980. These assemblies will be irradiated to goal fluences of 10, 20 and 40 dpa, respectively. Each assembly includes specimens at irradiation temperatures of 300, 400, 500 and 600°C.

2. Specimen Matrix

The DAFS specimens included in these tests are summarized in Table 1. The specimens are TEM disks loaded with a multiplicity of four. The path B

TABLE 1

DAFS Specimens for HFIR Irradiation

Alloy	Heat Treatment
B1	1025°C/5 min/AC + 750°C/8 hr/AC
B2	1025°C/5 min/AC + 800°C/8 hr/AC
83	1025°C/5 min/AC + 750°C/8 hr/AC
84	1025°C/5 min/AC + 850°C/3 hr/AC + 720°C/8 hr/FC to 620°C/10 additional hrs/AC

alloys are developmental precipitation strengthened iron-nickel-chromium alloys. Alloys B2, B3 and B4 are representative of three classes of precipitation strengthened alloys: alloy B2 is a molybdenum-modified, y'-strengthened alloy similar to Nimonic PE-16; alloy 83 is a niobium-modified, γ'-strengthened alloy; and B4 is a γ'/γ''-strengthened alloy similar to Inconel 706. Alloy B1 is also a molybdenum-modified, γ'-strengthened alloy. The effect of the γ'/γ misfit on γ' redistribution and helium trapping can be studied by comparing alloys B1 and B2 since they have different molybdenum contents and therefore different γ'/γ misfits.

Included in the ADIP portion of these tests are TEM disks of all five path B alloys in various cold-worked and cold-worked-Flus-aged-conditions. The DAFS program included specimens in the solution-treated-and-aged (STA) condition in order to bring out phases not present in the cold-worked-and-aged condition and to eliminate the effects of the pre-irradiation dislocation structure. These specimens will be used to study the irradiation stability of the precipitate phases and their helium trapping characteristics.

Similar specimens are also being irradiated in the ORR and EBR-II reactors.[1,2] The irradiation conditions are summarized in Table 2. All three experiments overlap at 400 and 500°C and a fluence of 20 dpa, while the HFIR and ORR irradiations overlap at all four irradiation temperatures and two fluence levels. Comparisons between these irradiations will indicate the influence of He/dpa ratio on microstructural evolution.

TABLE 2

Irradiations Including STA Path B Alloys

Reactor	Experiment Designation	Irradiation Temperatures (°C)	Fluences (dpa)
HFIR	HFIR-CTR-30, 31, 32	300, 400, 500, 600	10, 20, 40
ORR	MFE-IV	300, 400, 500, 600	9, 20, 30.50
EBR-II	AD-2	390, 500, 550	18, 35

VI. REFERENCES

1. D. T. Peterson and R. W. Powell, "OAFS Specimen Matrix for the ORR MFE-IV Test," DAFS Quarterly Report, DOE/ER-0046/1, January - March, 1980.
2. D. T. Peterson and G. R. Odette, "OAFS Specimen Matrix in the AD-2 Irradiation Experiment," this report.

VII. FUTURE WORK

The discharge of HFIR-CTR-30, at a fluence of 10 dpa, should occur early in 1981.

DISTRIBUTION

UC-20 (120)

UC-20c (76)

DOE/RRT-HQ (7)
Mail Stop B-107
Washington, DC 20545

Asst Director, Materials Tech
NA Davies
JF Decker
PB Hemmig
KG Moses
RE Price
FT Scott

DOE/RL (3)
Richland, WA 99352

WA Burns
GM Chenevert
LA Pasquini

Argonne National Laboratory (4)
9700 South Cass Avenue
Argonne, IL 60439

L. R. Greenwood
A. Taylor
APL Turner
H. Wiedersich

Brookhaven National Laboratory
Associated Universities
Upton, NY 11973

Chairman, Nuclear Energy Dept

Columbia University
Plasma Physics Laboratory
New York, NY 10027

R. A. Gross

General Atomics Company (2)
P.O. Box 81608
San Diego, CA 92138

GR Hopkins
D. Stevenson

Lawrence Livermore Laboratory (2)
University of California
P.O. Box 808
Livermore, CA 94550

MW Guinan
CM Logan

Los Alamos Scientific Laboratory (3)
University of California
P.O. Box 1663
Los Alamos. NM 87544

DJ Dudziak
CR Emigh
W. Green

Massachusetts Institute of Technology
Cambridge, MA 02139

L. Lidsky, Nuclear Engineering Dept

McDonnell-Douglas Astronautics
P.O. Box 516
St. Louis, MO 63166

D. Kummer

Mound Laboratory
P.O. Box 32
Miamisburg, OH 45342

Manager, Tech Appl and Development

National Bureau of Standards
Gaithersburg, MO 20760

CD Bowman

Naval Research Laboratory (2)
Metallurgy Division, Code 6390
Washington, DC 20375

J. Manning
JA Sprague

DISTRIBUTION (Cont'd)

North Carolina State University
Department of Nuclear Engineering
Raleigh, NC 26707

JR Beeler, Jr.

Oak Ridge National Laboratory (7)
P.O. Box X
Oak Ridge, TN 37630

Director, Thermonuclear Div,
(Bldg 9201-2)
RJ Colchin, Bldg 9201-2
FG Perey
M. Roberts, Bldg 9204-1
JO Stiegler
C. Weisbin
FW Wiffen

Pacific Northwest Laboratory (4)
P.O. Box 999
Richland, WA 99352

JL Brimhall
T. Chikalla
AB Johnson
LC Schmid

Princeton University (2)
Plasma Physics Laboratory
Forrestal Campus
P.O. Box 451
Princeton, NJ 06540

C. Osgood
K. Wakefield

HEDL (38)

HR Brager	W/A-57	DL Johnson	W/A-4	RE Schenter	W/A-5
WL Bunch	W/C-47	FM Mann	W/A-5	FA Schmittroth	W/A-5
LL Carter	W/C-47	WN McElroy	W/C-39	WF Sheely	W/C-44
BA Chin	W/A-58	GH Moulthrop	W/C-115	RL Simons	W/A-57
DG Dot-an (5)	W/A-57	RE Nygren	W/A-58	AL Trego	W/E-15
EA Evans	W/JAO-6	EK Opperman	W/A-58	GL Wire	W/A-58
FA Garner	W/A-57	NF Panayotou	W/A-53	HH Yoshikawa	W/A-62
DS Gelles	W/A-58	EF Parker	W/E-18	Central Files (5)	W/C-110
R. Gold	W/C-39	RW Powell	W/A-57	Publ Services (2)	W/C-115
HL Heinisch	W/A-57	RJ Puigh	W/A-58		

Rockwell International Energy Systems
8900 DeSoto Avenue
Canoga Park, CA 91304

D. Kramer

Sandia Laboratories (2)
Albuquerque, NM 87115

FL Vook (2)

Sandia Laboratories
Livermore, CA 94550

WD Wilson

University of Michigan
Nuclear Engineering Department
Ann Arbor, MI 48105

T. Kammash

University of Virginia
Charlottesville, VA 22901

WA Jesser

University of Wisconsin
1500 W. Johnson Drive
Madison, WI 53706

WG Wolfer

Westinghouse R&D Center (2)
Beulah Road
Pittsburgh, PA 15234

HR Holland
JA Spitznagel